

The Physics of Von Willebrand Factor (VWF)

Dissertation

von

DANIEL MICHAEL STEPPICH

1. Gutachter: Prof. Dr. Achim Wixforth
2. Gutachter: Prof. Dr. Wolfgang Brütting

Tag der mündlichen Prüfung: 10.02.2009

"I know a man who grabbed a cat by the tail and learned 40 per cent more about cats than the man who didn't."

Mark Twain

Contents

1	Introduction	1
2	Abstract	3
3	Theory and Background	5
3.1	The Blood Clotting Protein Von Willebrand Factor	5
3.1.1	Protein Structure	5
3.1.2	Biosynthesis of Von Willebrand Factor	10
3.1.3	The Role of VWF in Blood Clotting	11
3.1.4	Mechanical Activation of VWF	14
3.2	Interaction Forces on a Molecular Scale	18
3.2.1	Van der Waals Interaction	18
3.2.2	Hydrogen Bonding	21
3.2.3	Water Structure and the Hydrophobic Force	21
3.2.4	Biophysical Sensing	27
4	Materials and Methods	30
4.1	Atomic Force Microscopy	30
4.1.1	Setup and Basic Principle	30
4.1.2	Atomic Force Spectroscopy	31
4.1.3	Imaging Modes	34
4.2	The Lab on a Chip - AFM -Hybrid	36
4.2.1	Surface Acoustic Wave (SAW) driven Microfluidics	37
4.2.2	The Hybrid System	37
5	Results and Discussion	40
5.1	VWF-VWF-Interaction	40
5.1.1	Formation of Ultralarge VWF Aggregates	40
5.1.2	Relaxation of Ultralarge VWF Bundles	46
5.1.3	Impact of the Hydrophobic Effect on VWF Network Formation	50
5.1.4	Regulation of VWF Activation by Physiologic pH Changes	53
5.1.5	Protein - Phase - Diagram	59
5.2	VWF - Membrane - Interaction	68
5.2.1	Binding Model of Von Willebrand Factor to Cell Membranes	68
5.2.2	Investigation of the Binding Forces of von Willebrand Factor (VWF) to Phospholipid Membranes by Atomic Force Microscopy	78

6 Summary and Outlook	90
7 Danksagung	93
A Chemicals, Materials and Procedures	96
B Phospholipid Membranes	100
C Interaction Forces	102
Curriculum Vitae	115

1 Introduction

Rivers and streams have always been preferred places of human settlements building natural borders and protection lines against rivalling neighbours on the one side and providing means of transportation and therefore the exchange of goods and knowledge over far distances on the other side. The rise of most of the classic ancient civilizations such as the Sumerians in Mesopotamia between Euphrates and Tigris, the Egyptians on the river Nile or the Shang Dynasty in today's China on the Yellow River (Huang He), to name only a few, is directly or indirectly related to the wealth and protection provided by a river. With a growing population also the demand for agricultural products increased. By constructing channels and artificial water conducting systems these people were able to cultivate more agricultural land to feed a developing society. In modern times, man dikes whole rivers not only for means of irrigation but also for agricultural or residential land reclamation itself. But rivers imprisoned by barrages, dams and dykes also make a population vulnerable to flood and inundation catastrophes as experienced badly in recent years. In a fictional spirit one may ask at least two questions: Is there a possibility to prevent such catastrophes in the very beginning without the need for external repair of dyke damages and anybody ever taking notice that there was actually damage? Is there further a possibility that a river or a raging torrent in particular would carry all means with its waters that enables automatic dam sealing? The answer to these questions is either "No" or at least assumed to be not yet reality.

But actually it has been and is still reality for rivers and channels on a different length scale in a divers system. The channels of veins and arteries in the vesicular system of vertebrates comprise a multitude of similarities to rivers as the Mississippi or Rhein in different sections of their stream course. Equivalent to rivers for ancient and also modern societies, the blood stream within our vesicular system supplies a healthy and prosperous organism with all means of vitally important substances and materials. Even information transport to and from each individual cell, the smallest unit of life, is often performed on the "waterway". Whereas dyke breaks of rivers are experienced on the timescale of years, injuries to vessel walls occur approximately 1000 times per second in human bodies especially under high pressure and high blood flowing velocities. Severe bleeding events can be noticed as haematomas but we never become aware of the overwhelming percentage of vessel injuries due to an almost instantaneous repair mechanism carried within the blood stream itself. The initial step for this repair mechanism under high velocity and shear rate conditions is performed by a protein called "von-Willebrand-Factor" (VWF). The mechanical unrolling of the initially globular protein associated with its activation to form huge networks over a site of vesicular injury makes vWF an essential and vitally important resource to stop constant bleeding into the tissue. Without the help of these "protein-sandbags", provided and put into the right position

only by the streaming pattern and fluidic forces itself, innumerable little leaks would kill every organism exhibiting a closed vesicular system as an inescapable effect of the mechanical forces acting both from the inside and the outside onto blood vessels.

An investigation of the functional behaviour of this self provided wound healing system may help to understand the mechanisms of the most common inherited bleeding disorder of mankind known as von-Willebrand-Disease (VWD). To contribute to the knowledge of how to cure VWD - e.g. understanding both the natural process of blood clotting observed on the wildtype vWF and the disorders either by lacking vWF molecules or facing a dysfunctional form of it - would be a tremendous step into keeping this ultimate transportation system within the human body healthy and functional. Such a healthy blood system is as essential for every single person as an elaborated irrigation system is for a flourishing human society.

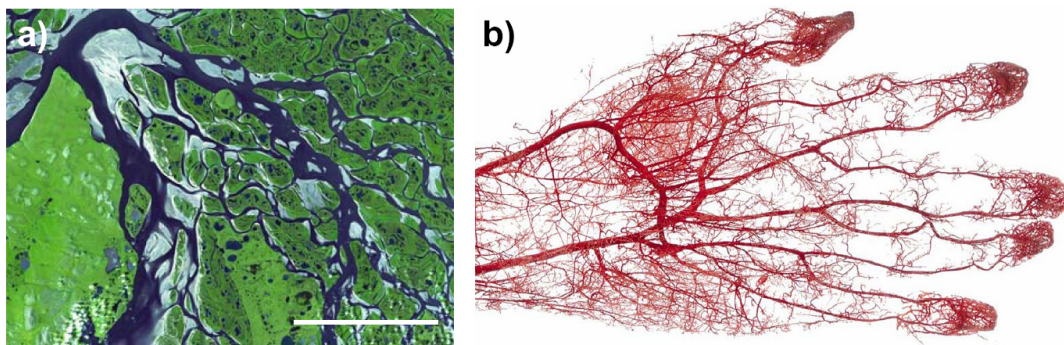


Figure 1.1: The Lena river in Siberia is one of the longest rivers on earth with a total length of approximately 4400km. It flows into the Arctic Ocean forming an extended delta (Scale bar $\approx 20km$). b) On a different length scale, the branched structure of arteries, arteriols and venes of a human hand resembles that of a river in its basic appearance.

2 Abstract

Haemostasis is a complex cascade of physiological processes, which induce the stop of blood loss at a site of vascular damage. In addition to various kinds of cells and proteins, this process involves numerous chemical and / or mechanical stimuli. In this thesis, the focus will be set on the action of the blood clotting factor Von Willebrand Factor (VWF), which plays a pivotal role during both primary and secondary haemostasis under elevated shear flow conditions. The observation of the necessity for a critical shear stress to mechanically unroll the multimeric protein VWF from a globular into an activated unrolled conformation [1, 2] led to a variety of biologically and medically motivated questions: Which forces retain VWF in its globular conformation? What influence does a surface have on VWF activation? How does a change of the streaming properties at a site of vascular damage affect VWF binding? How do VWF networks react to external stress? What parameters can modify the critical shear rate within wound healing? Do VWF molecules physically bind to endothelial cells and platelets besides the biological concept of specific lock- and-key interactions? If so, which membrane and protein factors mediate this interaction? Is such a physical attachment strong enough to span extended and haemostatically active networks?

Following the course of wound healing from VWF-VWF- to VWF-membrane-interactions, these open questions are approached from a physical perspective and are evaluated with regard to their medical impact within this thesis. In particular, the cumulative effect of stream line perturbations in close vicinity to an injured vessel wall and the influence of the surface itself on the critical shear rate were found to significantly affect network formation. Compared to bulk conditions, the combined slowing down of both rotational and translational VWF movement near a planar surface decreases the critical shear rate by up to 60% and hence facilitates VWF activation. Furthermore, modified streaming properties and vortex formation around protruding parts of damaged endothelium or extracellular matrix may directly result in an accumulation of the protein and contribute to an enhanced network formation potential. The elucidation of the interior dynamics of these extended networks represented an exquisite experimental challenge. The development of a Surface Acoustic Wave (SAW) driven microfluidic reactor integrated into an optical accessible Atomic Force Microscope (AFM) was a prerequisite for studying both the dynamics of the network formation process and its response on minute mechanical manipulation with an AFM tip. Application of pulling forces to VWF conglomerates in this effective hybrid system and monitoring their relaxation behaviour enabled the development of a "bundle jamming" model for crosslinked protein fibres emphasizing the role of both memory effects and strong coupling between single molecules inside protein networks. This coupling is described by an interaction potential ΔU . It exactly determines the order of magnitude of the critical shear rates to fit the conditions in our

blood vessels. In a series of experiments with varying solvent polarity, strong evidence was given that ΔU is governed by hydrophobic interactions. From a physiological perspective, a prominent parameter for fine-tuning ΔU and hence VWF's critical shear rate is a change in the pH of the solution. In this respect, it is a spectacular finding that the critical shear rate for unrolling the VWF molecule exhibits a clear maximum at blood $pH \approx 7.4$ and can be sensitively manipulated by minute pH variations in the range of $\pm 0,2$. Any deviation to both acidic and basic pH values results in a distinct decrease of the critical shear rate. Its consequences on the dynamic course of blood clotting are discussed as local changes from $pH \approx 7.4$ may occur at vessel lesions or stenosis. The origin of VWF's maximal stability against external forces under normal blood conditions is related to its minimal solubility at its effective isoelectric point which seems to be evolutionary adjusted exactly to blood pH . Our hybrid system allowed to establish a phase diagram, which displays VWF's activity as a function of both shear rate and pH . This phase diagram represents the condensed information for the response of VWF under different haemostatic conditions.

This precise knowledge of the reaction of the VWF molecule to external forces as well as the factors that control the dynamics inside single molecules and extended networks is further expanded to VWF's binding potential to endothelial cell walls. The investigation of the adhesion process of VWF to artificial phospholipid membranes identified the membrane phase state, membrane defects and domain boundaries as the main contributions for tight bonding and network formation. Atomic Force Microscopy (AFM) imaging under physiological buffer conditions revealed diverse arrangements of both single and activated VWF networks on varying membrane substrates. Advanced tip chemistry further enabled the binding of large multimers onto the AFM cantilever and the determination of extremely high interaction forces in the range of hundreds of pN of VWF with membranes in series of AFM Force Spectroscopy measurements. Both AFM imaging and Force Spectroscopy distinguished a striking influence of the hydrophobic core of the membrane to the interaction potential. The molecular binding mechanism itself seems to be relatively insensitive to VWF conformation while only the total amount of binding sites increases considerably in the activated state. Shear stress on the other hand does not exclusively affect the VWF multimer but also its dimeric building block. Structural analysis elucidated a pronounced susceptibility of single dimers to hydrodynamic forces. This will be the first report on structural changes inside the molecular basis of VWF upon mechanical forces. Previous results concerning VWF activation will have to be reconsidered on this molecular level as structural changes in its subunit will affect the stability of the whole protein under flow conditions and hence the stretching process itself.

The results presented in this thesis start to bridge the gap between physics and medicine by emphasising the role of fluid dynamics, macroscopic force fields, interfaces and protein mechanics in blood clotting. The elaboration of the molecular origin of VWF activation provided a powerful tool for medicine to estimate possible side effects under pathologic blood conditions.

3 Theory and Background

Wound healing is a vitally important adjustment of nature preventing continuous bleeding into the tissue after damage to the blood vessels. A normal human being is bleeding permanently in small arterioles and veins without even getting aware of it. An instantaneous repair mechanism involving numerous blood clotting factors seals vessel lesions and stops excessive blood loss. An essential player in this cascade is the multimeric protein Von Willebrand Factor (VWF). In this chapter, the basics of protein architecture and VWF's role in blood clotting as well as the essential interaction concepts on a molecular scale will be elaborated in order to establish the theoretical groundwork for the results part.

3.1 The Blood Clotting Protein Von Willebrand Factor

In this section, VWF's role in blood clotting will be thoroughly reflected starting with basic considerations to protein structure in general and VWF's complex biosynthesis in particular. After highlighting its role in both primary and secondary haemostasis the state of the art of VWF's unique mechanical activation process will be summarised in order to provide the basis for the investigation of its adhesion and network formation ability.

3.1.1 Protein Structure

Proteins are one of the basic building blocks of living organisms. Besides a multitude of other properties, they regulate body functions as hormones, catalyse vital reaction as enzymes, induce immunologic responses as antibodies, myosins and actins provide muscle contraction and collagens maintain the body structure of organs and interconnect cells. And even though their structure and size is as diverse as their multiple tasks, the basic underlying construction pattern follows a standard working plan. This section is devoted to develop an understanding of this common construction plan, the essential properties of its constituents and how these properties depend on and change with three dimensional protein structure.

The smallest repeating units of proteins are amino acids. In proteinogenic (protein forming) amino acids, a carboxyl and an amine group are interconnected by a α -carbon atom. The structure of the side chain R discriminates the difference between the 20 amino acids used to build up a protein (see Appendix A). Depending on the pH of the surrounding medium, amino acids exhibit both acidic and basic properties and can carry negative (deprotonation of the carboxyl group), positive (protonation of the amine group) or no

charge (zwitterionic state) (figure 3.1).

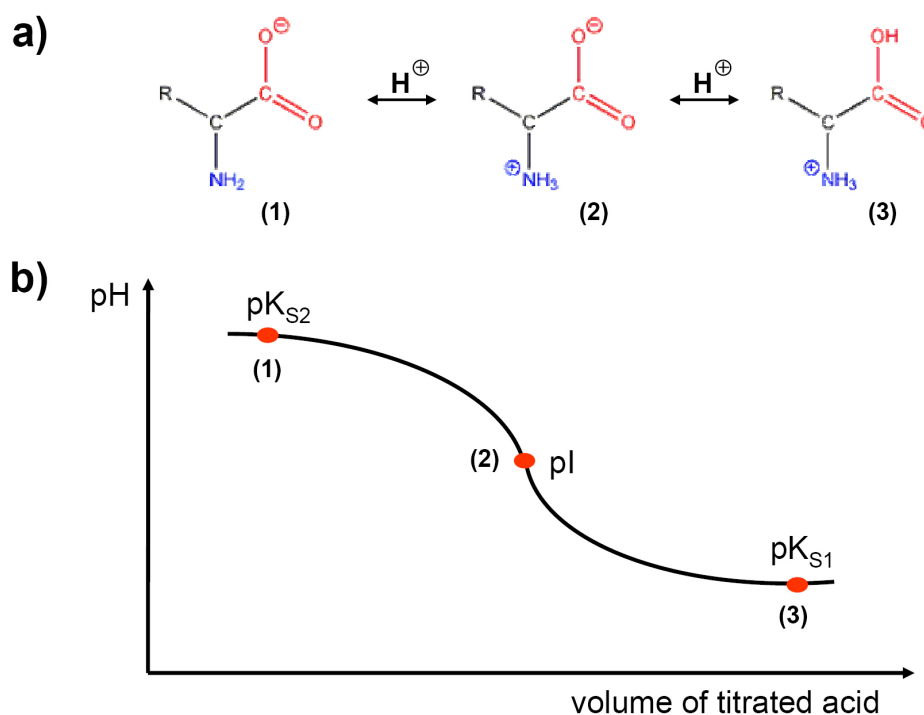


Figure 3.1: a) Under basic conditions the amino acid is fully deprotonated comprising a negative net charge (1). Decreasing the pH to a certain value leads to the protonation of the amine group (2). A further decrease of the pH results in the protonation of the carboxyl group and a net positive charge of the molecule (3). b) A typical titration curve of a solution of identical amino acids is illustrated. Starting at high pH values, where most amino acids comprise negative net charge (1), acid is titrated into the solution. At the isoelectric point pI all amino acids carry a net neutral charge. Additional protonation at regimes of lower pH transforms the molecules into their positively charged state (3). The absolute values of pK_{S1} , pI and pK_{S2} strongly depend on the nature of the residue R.

Characteristic parameters for the charge state of a molecule or a reactive group, respectively, are its pK and pI values. When the pH of the solution equals the pK value of a reactive compound, the probability for being in the protonated positive charged state equals the probability for its deprotonated state. Within an amino acid, different pK values can be assigned to both the carboxyl- and the amine group. The underlying acidic (or basic) process may be realized by considering the following equilibrium reaction between:



The acidic dissociation constant K is given by:

$$K = \frac{[H^+] \cdot [A^-]}{[HA]} \quad (3.2)$$

The negative common logarithm of the acidic dissociation constant defines pK :

$$-\log(K) = -\log \left[([H^+]) \cdot \left(\frac{[A^-]}{[HA]} \right) \right] = -\log ([H^+]) + \log \left(\frac{[HA]}{[A^-]} \right) \quad (3.3)$$

$$\Leftrightarrow pH = pK - \log \left(\frac{[HA]}{A^-} \right) \quad (3.4)$$

Equation 3.4 is known as the Henderson-Haselbalch equation [3]. Typical pK values for carboxyl groups (pK_{S1}) in amino acids are around 2.2 and 9.4 for amine groups (pK_{S2}). Hence, under neutral conditions free amino acids exist mainly in a zwitterionic state. The pH value with vanishing net charge of the molecule is called isoelectric point pI and can be calculated as the mean value of pK_{S1} and pK_{S2} [4].

Peptide bonds between the carboxyl and the amine group of consecutive amino acids form the backbone of proteins [5]. The primary structure of a protein is defined as the linear sequence of amino acids. Due to participation of both carboxyl and amine groups in peptide bonds, both the pK values and the isoelectric point pI arise solely from the side groups R. For energetic, entropic and functional reasons an elongated chain is not very favourable. In addition to the primary structure, a secondary, tertiary and quaternary structure of proteins are discriminated. The secondary structure describes the spatial orientation of the side chains R and is divided into the unordered random coil and the ordered α -helix and β -sheet fractions (figure 3.2). Within the α -helical structure, the backbone of connected C and N atoms forms the centre of the helix while the residues are directed towards the outside. The hydrogen bonded NH and CO groups that stabilize the helical structure are four side chains apart from each other. Whereas all amine and carboxyl groups are involved in the stabilization, the residues R do not participate in the H -bridges. Adjacent side chains comprise a distance of about $0.15nm$ and an angle of 100° along the helical axis. Therefore, a full revolution of the α -helix corresponds to 3.6 amino acid side chains. In nature, the right-handed (clockwise) conformation with four to over forty residues is predominant although there is no theoretical proscription for counter-clockwise structures. This special hydrogen bonding pattern results in an additional electric feature. Within the complete α -helical structure the hydrogen bonding oxygen atoms point towards the C -terminal end of the helix, whereas the hydrogens from the amine group are directed to its N -terminus. This directed distribution of electrons within the hydrogen bonds sums up to an overall electric dipole that may lead to pronounced long range attraction of charged surfaces and contributes to accelerated interactions with other proteins [6]. In contrast to compact α -helices, β -sheets feature a rather flat and open structure. The distance between two adjacent amino acids along the β -sheet axis is approximately $0.35nm$ compared to $0.15nm$ in the α -helix. β -sheets are stabilized by hydrogen bonds between CO and NH groups of different peptide strands.

Depending on the direction of the backbones of the aligned amino acid chains, parallel and antiparallel β -sheets are distinguished (figure 3.2). The size of β -sheets differs significantly from two to twelve parallel lines of up to 15 amino acids [4]. A common feature of many antiparallel β -sheets is a so called β -turn ending, in which the direction of the amino acid chain is reversed completely within the range of two amino acids [7]. The redirected peptide backbone forms the adjacent second chain within the β -sheet. By definition a turn in general is an approach of α -carbon atoms of different amino acids to distances closer than $0.7nm$ while their side chains are not involved in a α -helix or β -sheet. In addition, turns may also connect α -helical and / or β -sheet structures, which do not interact directly with each other. Possible conformations include γ -, β -, α - and π -turns comprising two, three, four and five residues between hydrogen bonding amino acids [8]. The unordered random coil secondary structure includes these various turn patterns but is not limited to them. It further contains all conformations without any α -helical or β -sheet structure independent of the distance between the residues or α -carbons.

Combining the various random coil structures, α -helices and β -sheets into a typical three dimensional structure yields the protein's tertiary structure. It specifies the spatial orientation of residues which are farther away from each other within the linear amino acid sequence. In addition to H -bridges, the stabilization of the tertiary structure is often realized by disulfide bonding between S carrying cysteine residues. In most proteins, a specific spatial organization is a direct prerequisite for the proper execution of its equally specific functions [9, 10, 11]. A variety of proteins builds additional functional units between two or more non-covalently linked, individual protein segments. The quarternary structure description accounts for an arrangement at this superior level. However, the tertiary structure is sufficient to characterize the three dimensional compositions of most proteins. In literature, the terminus "native" or "folded" is frequently used to denote the unique three dimensional structure within a functional protein.

Still, the underlying construction plan of this complex system is found in the specific sequence of amino acids. Within globular proteins, the spatial amino acid distribution generally follows the characteristic properties of the side chains. Non-polar residues are predominantly buried within the protein core while hydrophilic residues are found at the interface between protein and aqueous medium [12]. Although the densely packed protein interior normally excludes water, single H_2O molecules can be incorporated within certain protein structures and mediate attractive interaction by the formation of hydrogen bridges. The characterization of a multitude of protein features, such as activity, charge state, pK or pI , requires more than the numbers of the constituting amino acid [4]. A certain spatial arrangement can change pK and pI values, thermodynamic stability, charge state or solubility of the protein compared to the unfolded elongated chain of amino acids. The dependence on the three dimensional structure can lead to interesting results. Acid titration to a folded protein may resemble the titration curve from figure 3.1 as long as the native structure is maintained. A structural change caused by partial or complete unfolding and denaturation can lead to non-Henderson-Hasselbalch curves and even back-titration effects with increasing pH values on the addition of more acid [13].

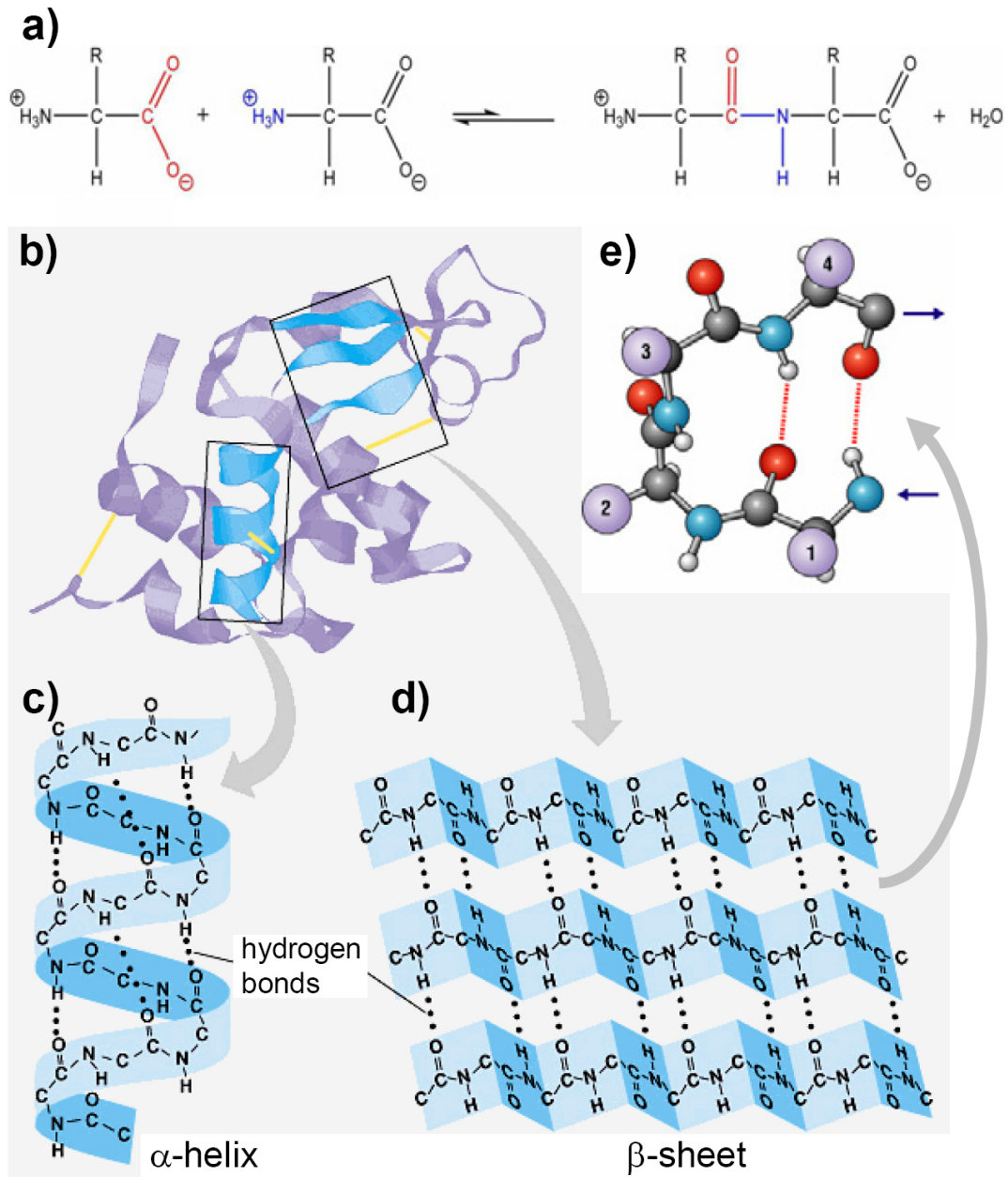


Figure 3.2: a) A peptide bond forms between two amino acids accompanied by the secession of a water molecule. The amino acid chain may arrange into b) a complex three dimensional structure (tertiary structure) consisting of c) α -helices or d) β -sheets. These secondary structures are both stabilized by hydrogen bonds. Antiparallel β -sheets often consist of a single amino acid chain, which exhibits a so called d) β -turn, in which the CO group of the side chain of the n -th amino acid forms a hydrogen bridge to the NH side chain of the $(n+3)$ th amino acid. This spatial arrangement can turn the direction of the amino acid chain.

3.1.2 Biosynthesis of Von Willebrand Factor

The first stages of Von Willebrand Factor (VWF) biosynthesis in megakaryocytes and endothelial cells follow the common protein assembly line. The 178,000 base pairs of the extraordinary large VWF gene are located on the short arm of chromosome 12 and transcribed into an m-RNA copy containing 52 exons [14]. According to the m-RNA plan the first translation product of 2813 amino acids is assembled in the ribosomes. This monomeric VWF precursor molecule (prepro VWF) with a mass of $\approx 360kDa$ exhibits already all functional domains including a propeptide containing 741 residues (figure 3.3).

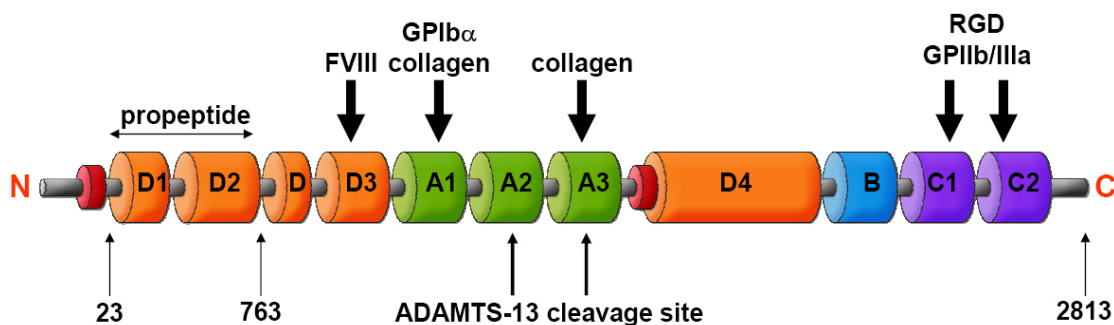


Figure 3.3: The amino acids are numbered in ascending order beginning at the amino end of the protein. Capital letters represent associations of amino acids into functional domains. The prepro VWF molecule contains a signalling peptide (residues 1 to 22), a large propeptide (23-763) and the mature subunit (764-2813) residues [15].

After this first translation product is conveyed to the endoplasmic reticulum (ER) two prepro VWF molecules are covalently linked at their C domains. This "Tail-to-tail" dimerization by disulfide bonding involves only amino acids within the last and cysteine rich 150 residues [15]. A prerequisite for the dimerization process and consequently for VWF's haemostatic function is the glycosylation of certain residues of the monomer in the ER. In addition, the transport of the pro-VWF-dimers to the Golgi apparatus for further processing seems to be inhibited by the absence of sugar groups on the molecule [16]. In the acidic environment of the Golgi, dimers form the mature VWF multimer by covalent linkage at their cysteine rich amino ends accompanied by proteolytic cleavage of their $95kDa$ propeptide. The role of the propeptide in this "head-to-head" multimerization process is not completely understood yet. Although it may directly catalyze the formation of disulfide bonds between VWF dimers [17], multimers consisting of up to 100 dimeric subunits can also form between pro-VWF dimers while they do not form in mutants lacking the propeptide [18]. Subsequently the resulting multimers are either directly released to the blood stream or stored in special compartments called Weibel-Palade bodies [19]. About 5% of all VWF multimers are directed to these cylindrically shaped granules with roughly $0.2\mu m$ in width and $4\mu m$ length. The transport to the

Weibel-Palade bodies being specifically found in endothelial cells also requires the presence of the propeptide. A variety of chemical stimuli induced by injuries of the vessel wall or an increased level of adrenalin in the surrounding blood triggers the release of VWF into the blood stream. Stored and directly secreted VWF molecules seem to differ in the distribution of their size. Whereas in Weibel-Palade bodies exclusively large multimers are found, in the pathway of continuous release VWF sizes range from dimers to large multimers [20]. It is not clear yet, if this is a consequence of improper analysis of plasma-derived and therefore enzymatically cleaved VWF. Nevertheless, both circulating and secreted VWF from Weibel-Palade bodies contribute to wound healing and blood clotting.

3.1.3 The Role of VWF in Blood Clotting

Wound healing is an extremely important adjustment of nature preventing continuous bleeding into the tissue after contusions, transections, burns and lesions of all sizes. Under normal conditions, a stable blood clot is sealing an injured blood vessel in a complex process involving more than a dozen blood coagulation factors. A fast and localized reaction is a prerequisite for a proper functioning of this process. Especially for the use at high shear flow conditions in small arterioles and veins evolution designed a very effective sealing mechanism with VWF as the key player. In the following chapter, the course of wound healing in small arterioles will be sketched as elaborate as necessary for a proper understanding of the underlying processes while keeping it as simple as possible to motivate the basic questions under investigation in this thesis. The focus will be set on VWF network formation on exposed collagen of the connective tissue and on platelet binding to the damaged vessel walls. A brief discussion of VWF's role in the subsequent blood clot stabilization followed by its degradation will introduce a self consistent blood vessel repair mechanism.

The initial process of stopping blood loss by the formation of VWF-platelet plugs is known as primary haemostasis. It is accompanied by the contraction of the injured blood vessel that limits bleeding at first place and strongly affects the streaming properties of the flowing blood. Furthermore, the smooth continuous layer of intact endothelium is replaced by a rough surface of exposed extracellular matrix and damaged cells. Both the altered local streaming conditions, previously hidden cell walls and the exposure of various kinds of connective tissue induce the binding of VWF molecules. This process involves a conformational change within the protein from an inactive globular into an elongated activated state. Activated VWF comprises specific receptors in its A1 and A3 domain to the counterpart in the collagen matrix. Bound to the surface, VWF molecules interconnect and form macroscopic networks on exposed layers of collagen at sites of vascular damage (see figure 3.5). While the VWF network represents the basis for wound healing, platelet aggregation to this network is the starting point for the growing plug, which finally seals the vessel damage. In this regard it is worth mentioning that platelets are enriched near the vessel wall which drastically increases the binding probability (Fahraeus-Lindquist-effect) [21].

The adhesion of platelets to a VWF network at a site of injury involves a two step

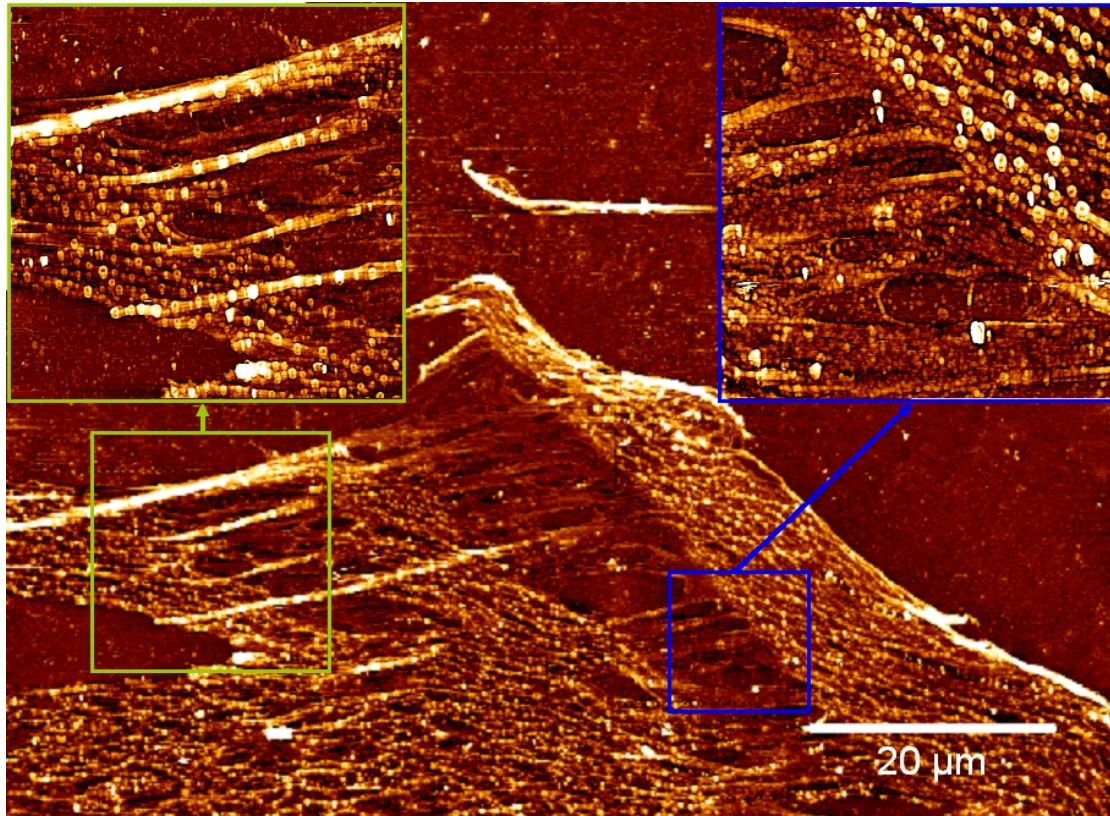


Figure 3.4: An extended VWF network on a thin collagen layer formed under shear flow conditions as they are also found in small arteriols and veins. After dehydration, the network was imaged by AFM tapping mode in air. Both insets show different regions of the network exhibiting similar and also very different features. Elongated thick VWF fibres (left inset) and globular VWF molecules (right inset) can be distinguished within the network. Similar network structures covered a broad area of the sample surface.

mechanism. In first place, a weak bond with a high dissociation constant is formed between VWF's A1 domain and the platelet receptor *GPIIb* α . Platelets are decelerated and roll on the VWF network as a result of the flow induced torque, giving a stronger and irreversible bond involving VWF's C1 domain and platelet integrin $\alpha_{IIb}\beta_3$ with a low dissociation rate enough time to form [22]. Due to the soft character of platelets a membrane tube can form from the adhesion point on the VWF surface along the direction of the fluid flow [23]. The morphology, formation and detachment kinetics of these membrane tethers depend strongly on the acting shear field. Tether formation is an important step in mediating strong adhesion by slowing platelets down and reducing the level of shear stress experienced by individual receptor-ligand interactions [24].

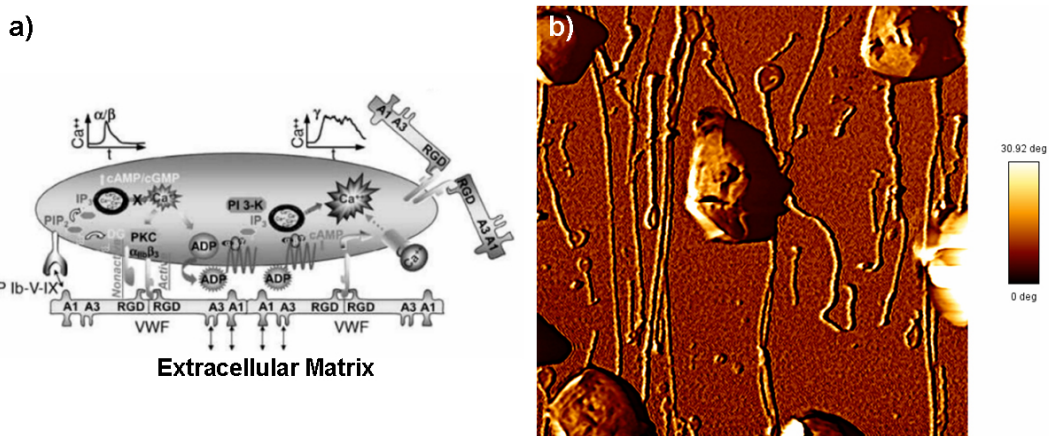


Figure 3.5: a) The scheme illustrates the biological picture of platelet binding to VWF molecules. Various receptors on different protein domains mediate the binding of VWF to both the extracellular matrix and platelets. b) Platelets were imaged after shear stress of 20000 Hz in buffer condition was applied followed by subsequent formaldehyde fixation (image size $17\mu\text{m} \times 17\mu\text{m}$). Membrane tethers were predominantly found in the direction of flow. But also kinked and broken tethers can be observed indicating multiple binding sites within the tether.

After a tight bond has formed, platelets tend to spread on the surface comprising even more binding sites for VWF while reducing the opposing drag forces at the same time. As more and more platelets aggregate on the site of vascular damage, VWF serves as a glue between multiple layers of platelets. This platelet plaque grows until further loss of blood is prevented. If the rent in the vessel wall is small, the platelet plug itself can seal the lesion. Larger damage requires further stabilization of the platelet aggregate during secondary haemostasis. Herein, water-soluble fibrinogen is transformed to water-insoluble fibrin, which forms a meshwork for embedding both platelets and erythrocytes [25]. The production of fibrin involves a cascade of multiple blood clotting factors activating each other. The dysfunction or deficiency of one of these clotting factors can decelerate or even stop blood clotting. One step in this cascade is accomplished by

so called Factor VIII. The main fraction of Factor VIII is bound to VWF which increases its stability against proteolytic cleaving inside the blood stream. Hence, VWF performs two important tasks during secondary haemostasis: It both stabilizes and provides a carrier system for Factor VIII to its point of destination.

Clot formation does not represent the end of wound healing. The regulation of the size of the growing plaque and its complete degradation after the vessel lesion is sealed and new endothelium has substituted dead cells is equally important. The protease ADAMTS-13 is capable of cleaving VWF in its A2 domain between Tyr-842 and Met-843 into fragments of about 140 and 176kDa [26]. Hence ADAMTS-13 contributes to the inactivation of VWF's binding potential for collagen and platelets. Tsai showed that the cleaving process itself depends significantly on the conformation of VWF. In two sets of experiments, he used denaturants [27] and shear stress [28] to induce a conformational change of VWF before ADAMTS-13 was added and the yield of cleaved fragments was analysed. A distinct increase in enzyme activity was found in activated VWF. Exhibiting a conformational dependent cleaving mechanism ADAMTS-13 is perfectly suited for the down-regulation and degradation of immobilized unrolled VWF and platelet plaques. Tsai further discussed the possibility that ADAMTS-13 may be involved in modulating the size of VWF in the circulation due to enhanced cleaving in high shear regimes without the necessity of its immobilization at a site of injury.

In this complex environment, a dysfunction of VWF can drastically affect both primary and secondary haemostasis. Such dysfunctions can arise as a result of any disturbance of VWF's long pathway during biosynthesis and storage as well as lack or abundance of the cleaving protease ADAMTS-13. As a matter of fact, Von Willebrand Disease (VWD), which covers all kinds of possible malfunctions associated with VWF, is the most common inherited bleeding disorder. Clinical significant VWD occurs with a prevalence of about 125/million [29], whereas about 8000/million people comprise at least a lower degree of VWF impairment [30]. For a detailed overview about all classified forms of VWD the interested reader is referred to [31].

3.1.4 Mechanical Activation of VWF

The biological or medical point of view on VWF adhesion at sites of vascular damage focuses on the binding of a variety of ligands to corresponding receptors. Such an approach bears one major shortcoming: The counterintuitive phenomenon of VWF's enhanced binding potential at increased shear flow conditions can not be accounted for by this conventional mechanism. VWF molecules develop their unique binding properties exactly in regimes of high shear flow while they do not adhere to collagen and platelets under low shear conditions. In their recent publications, Schneider et al. and Katz et al. could not only monitor a globule-stretch transition in VWF by fluorescence microscopy [1] but also elucidated first insight into both the molecular and physical origin of the observed behaviour [2]. The work of these authors is reviewed on the following pages. The secret of VWF unique behaviour is found in the perfect combination of its multimeric composition, its unusual large monomer size and its susceptibility to shear stress of the surrounding blood. Within a blood vessel the fluid velocity decreases from its centre

towards the surface (figure 3.6). This velocity gradient induces friction between adjacent layers of fluid resulting in shear stress on every particle within the blood stream. A measure for the shear stress normalized to a medium with the viscosity of $1mPas$ is given by the shear rate

$$\dot{\gamma} = \frac{\partial v}{\partial r} \quad (3.5)$$

It is defined as the gradient of the flow velocity v with respect to the vessel radius r . The highest shear rates of approximately $\dot{\gamma} \approx 470 - 4700s^{-1}$ occur at the vessel walls of small arterioles (diameter $d \approx 10 - 30\mu m$) [32]. Using a surface acoustic wave (SAW) driven microfluidic chip (details for the setup are found in [33]), a shear induced conformational change of VWF molecules from their folded globular into an elongated state was monitored under bulk conditions. The length of the VWF globule increased from a diameter of roughly $l \approx 1\mu m$ to an elongated fibre of about $l \geq 15\mu m$. This abrupt and reversible transition occurred at a critical shear rate of about $\dot{\gamma}_{crit} \approx 5000s^{-1}$. In a second experiment the adhesion potential of labelled VWF molecules to a layer of collagen was measured as a function of $\dot{\gamma}_{crit}$. Whereas almost no VWF adhesion could be observed for shear rates below $\dot{\gamma}_{crit}$, extensive binding was detected above the critical shear rate. These results provided direct evidence for the coupling between VWF's three dimensional structure and activity.

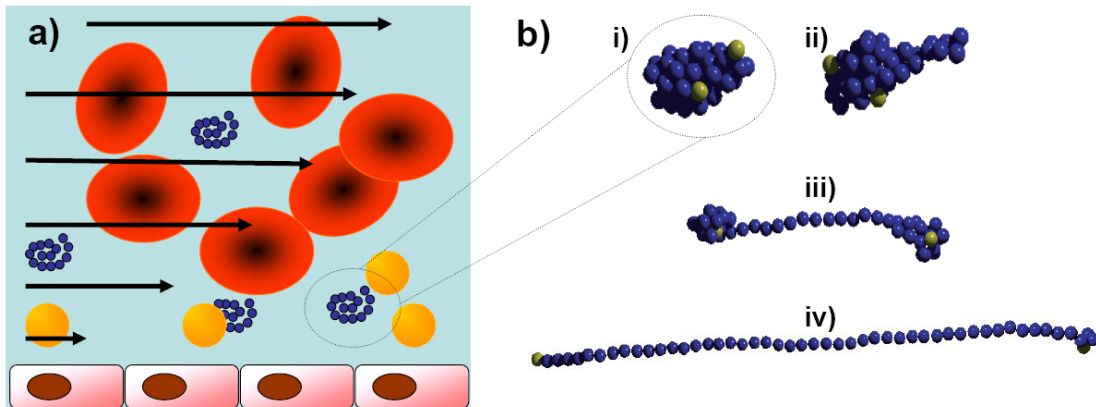


Figure 3.6: The velocity of the streaming blood (indicated by the length of the arrows) decreases from the centre of the blood vessel towards the endothelial cell surface resulting in a shear force acting on VWF molecules (blue). b) Computer simulations demonstrated a reversible transformation of a multimeric protein from a globular (i) into an unrolled state (iv). This conformational transition is achieved through intermediate states where hydrodynamic drag on protein protrusions (ii) initially elongates the protein.

Hydrodynamic computer simulations unravelled deeper insight into the physical origin of the observed behaviour at arterial shear stress. The VWF molecule is modelled as a linear string of spherical monomers. Stiff springs between these subunits replace the

covalent bonds and limit the stretching of the chain. Non-adjacent monomers interact over Lennard-Jones potentials. Furthermore, the simulations included both long range hydrodynamic effects between distant monomers and solvent-flow stagnation inside the molecule [2]. Katz et al. showed that the critical shear rate $\dot{\gamma}_{crit}$ obeys the scaling law

$$\dot{\gamma}_{crit} = \frac{\Delta U^2 \cdot L^{\frac{1}{3}} \cdot a^{-\frac{10}{3}}}{12 \cdot \eta \cdot k_B T} = \frac{\Delta U^2 \cdot N^{\frac{1}{3}} \cdot a^{-3}}{12 \cdot \eta \cdot k_B T} \quad (3.6)$$

with a temperature independent interaction potential ΔU , the contour length of the polymer L , the number of monomers N , the monomer size a , the viscosity of the medium η , the Boltzmann constant k_B and the absolute temperature T . High or low values of ΔU correspond to bad or good solvent condition, respectively. A difference between $\Delta U \approx 0.4k_B T$ and $2.0k_B T$ already yields a distinct divergence in the characteristics of the stretching transition. The packing of the monomers within the globule is drastically enhanced for higher values of ΔU . In clear contrast to a polymer under bad solvent conditions ($\Delta U \approx 2.0k_B T$) comprising an abrupt elongation at a critical shear rate, the average polymer length under good solvent conditions increases slowly but steadily with increasing shear field (figure 3.7). The first case perfectly reflects the observed activation

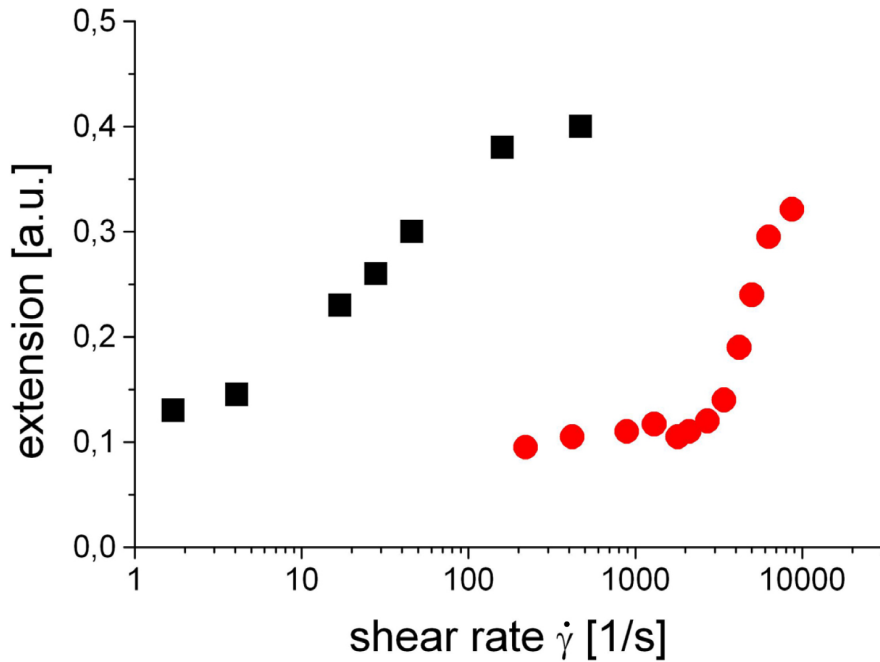


Figure 3.7: Simulation results for the normalized extension (equal to the average extension divided by the contour length) of a 50-mer as a function of the shear rate $\dot{\gamma}_{crit}$ using a monomer size $a = 80nm$ and a viscosity of $\eta = 1cP$. The coiled (black squares) and the collapsed (red circles) polymers have an attractive contact potential depth of $\Delta U = 0.416$ and $\Delta U = 2.08$ (in units of $k_B T$), respectively. This figure is taken from [1].

of the VWF molecule. In literature the terminus "coiled" denotes a loosely packed molecule while a "collapsed" polymer exhibits strong internal coupling due to a high ΔU . The simulations further elucidated reversible length fluctuations from elongated to globular states of the polymer. Whereas these fluctuations are already observed at low shear rates in the coiled state, they only occur in close vicinity of the critical shear rate $\dot{\gamma}_{crit}$ in the collapsed molecule. In summary, ΔU significantly affects both the character and the location of the transition between the globular and elongated state. The extraordinary size of the VWF dimeric subunit directly results in the adjustment of the critical shear rate $\dot{\gamma}_{crit}$ to arterial conditions. The scaling of the critical shear rate $\dot{\gamma}_{crit}$ with the monomer size a can be derived in a simple estimation of the force f in a hydrodynamic flow field on a protrusion of length l on a globular VWF molecule (see also [2]).

$$f = (\dot{\gamma}_{crit} \cdot l) \cdot \xi \cdot \frac{l}{R} \quad (3.7)$$

The first part of equation 3.7 describes the velocity difference of the streaming fluid on the protruding fibre and ξ the friction coefficients of the protrusion. $\frac{l}{R}$ denotes the disturbance of the hydrodynamic flow field around the globule. Since shear flow is a combination of both elongational and rotational flow, the elongational flow which pulls on the protein is reduced due to the rotation of the globule.. Herein, l , R and ξ scale linearly with the monomer size a . Therefore, the force f scales like $f \propto \dot{\gamma}_{crit} \cdot a^2$. This force f has to overcome the cohesive force f_{coh} that keeps the polymer in its globular conformation

$$f_{coh} = \frac{\Delta U}{a} \quad (3.8)$$

Equating both forces yields

$$\frac{\Delta U}{a} \propto \dot{\gamma}_{crit} \cdot a^2 \quad (3.9)$$

and hence

$$\dot{\gamma}_{crit} \propto a^{-3} \quad (3.10)$$

Due to the scaling with the inverse cube, the position of the critical shear rate $\dot{\gamma}_{crit}$ depends critically on the monomer size a while the shape of the transition curve is not affected. According to equation 3.6, a monomer size $a \approx 1nm$, corresponding to the size of several amino acids, would result in a critical shear rate $\dot{\gamma}_{crit}$ for polymer activation of about $10^{10}s^{-1}$. This is far from any physiological or pathophysiological condition. The monomer radius that gives a critical shear rate close to the experimental results is $80nm$, which is of the order of dimeric VWF repeating unit [34].

Although biological or chemical factors may contribute to the critical shear rate $\dot{\gamma}_{crit}$ within the blood vessel, the coupling between VWF function and conformation can be explained in terms of hydrodynamic forces, interaction potential ΔU and monomer size a .

3.2 Interaction Forces on a Molecular Scale

”Now we come to the heart of chemistry. If we can understand what holds atoms together as molecules we may also start to understand why, under certain conditions, old arrangements change in favor of new ones. We shall understand structure, and through structure, the mechanism of change” (Peter Atkins in [35]). In this sense, the basic concepts of van der Waals interaction, hydrogen bonding, water structuring and hydrophobic interaction will be reflected on the following pages in order to be able to interpret structural changes within the VWF molecule upon both shear and surface induced conformational changes. This selection is not meant to be a comprehensive review of all interaction forces but an extract of important concepts for the results and related discussions presented in this thesis. Although it can be considered as a special case of van-der-Waals interaction, an own subchapter is addressed to hydrogen bonding because of its outstanding meaning for life and proteins in particular. The last part of this chapter generalises these concepts to the interaction between extended surfaces under fluid conditions with special regard to tip - sample interactions in Atomic Force Microscopy (see chapter 5.2.2).

3.2.1 Van der Waals Interaction

The term van der Waals (vdW), as it is used in this thesis consists of the attractive interactions between permanent dipoles, permanent and induced dipoles and temporary and induced dipoles. The illustration of these forces is closely related to [36].

Permanent dipoles arise from a polar covalent bond in molecules such as HCl or H_2O . The force between two permanent dipoles is of electrostatic nature and is often referred to as Keesom - Force. The interaction potential V is determined by the distance between their centres and the mutual orientation of the vectors of their dipole moments μ_i . Thermal motion of the molecules (translation and rotation) continuously pushes the dipoles out of their equilibrium by randomly changing both distance and direction of μ_1 and μ_2 . As a result, the Keesom-potential disappears for high temperatures:

$$V_{Keesom} = -\frac{2}{3 \cdot k_B T} \cdot \left(\frac{\mu_1 \mu_2}{4\pi \cdot \epsilon_0} \right)^2 \cdot \frac{1}{r^6} \quad (3.11)$$

Herein k_B denotes the Boltzmann constant, T the absolute temperature and ϵ_0 the dielectric constant of the vacuum. Despite direct interaction of two permanent dipoles, the electric field of a polar molecule can also cause a shift of the spatial probability distribution of electrons in adjacent molecules and, thus, induce a dipole moment. The strength of the resulting attractive interaction (Debye-Force) depends basically on the polarizability α of the molecule. α itself increases with the atomic number and surface area of an element or molecule, respectively. Due to screening effects of electrons in inner shells, these elements are more susceptible to external electric fields E :

$$\mu = \alpha \cdot E \quad (3.12)$$

In contrast to the interaction of permanent dipoles, Debye-Forces are temperature-independent as the polarization of a molecule can be considered as an immediate response to the electrical field of a permanent dipole. In the general case of two different molecules featuring permanent dipole moments μ_1 and μ_2 and polarizabilities α_1 and α_2 , the dipole induced dipole energy is

$$V_{Debey} = -\frac{\mu_1^2\alpha_2 + \mu_2^2\alpha_1}{(4\pi \cdot \epsilon_0)^2} \cdot \frac{1}{r^6} \quad (3.13)$$

So far, the interaction between two non-polar molecules with uniform electron distributions has been neglected. These molecules also face a force arising from dipole-dipole attraction. Whereas the average electron residence probability equals the position of the positive nucleus, fluctuations in the electron density form temporary dipoles which polarize adjacent molecules (induced dipoles). This temperature-independent attractive force between temporary and induced dipoles in non-polar molecules is referred to as London-dispersion-force. Although small compared to the interaction of permanent dipoles, its significance is illustrated most prominent in the condensation of noble gases. The London-dispersion energy depends on both the polarizability α and the ionisation energies I of the particles:

$$V_{London} = -\frac{3}{2} \cdot \frac{\alpha_1\alpha_2}{(4\pi \cdot \epsilon_0)^2} \cdot \frac{I_1 \cdot I_2}{I_1 + I_2} \cdot \frac{1}{r^6} \quad (3.14)$$

The sum of Keesom-, Debye- and London-Forces forms the van der Waals (vdW) - Potential with its characteristic $V_{vdW} \propto -\frac{1}{r^6}$ dependence (see also Appendix C for a selection of forces with electrostatic origin). The attractive range of the vdW interaction is limited to distances wherein the wavefunctions of electrons from different atoms or molecules do not overlap. For separations smaller than $\approx 0.1nm$, approaching molecules start to face a repulsive force of quantum mechanical origin caused by Pauli's exclusion principle. Overlapping wavefunctions induce the formation and occupation of high energy electron states in order to avoid identical quantum numbers. The population of these high energy states results in a repulsive force on the binding partners. Although there are still a lot of uncertainties concerning precise mathematical structure of this repulsive potential, it is described either by an exponential or a $V_{rep} \propto \frac{1}{r^{12}}$ decay. The summation of attractive vdW and repulsive Pauli forces yields the so called Lennard-Jones-Potential (figure 3.8)

$$V_{LJ} = \epsilon \cdot \left[\left(\frac{r_0}{r}\right)^{12} - 2 \cdot \left(\frac{r_0}{r}\right)^6 \right] \quad (3.15)$$

with the equilibrium distance r_0 between the interacting particles and depth of the potential ϵ .

In order to generalize the vdW potential from a two body problem to complex macroscopic systems, the sum over all atoms or molecules of both bodies interacting with each other has to be estimated. Although the origin of the interaction between macroscopic

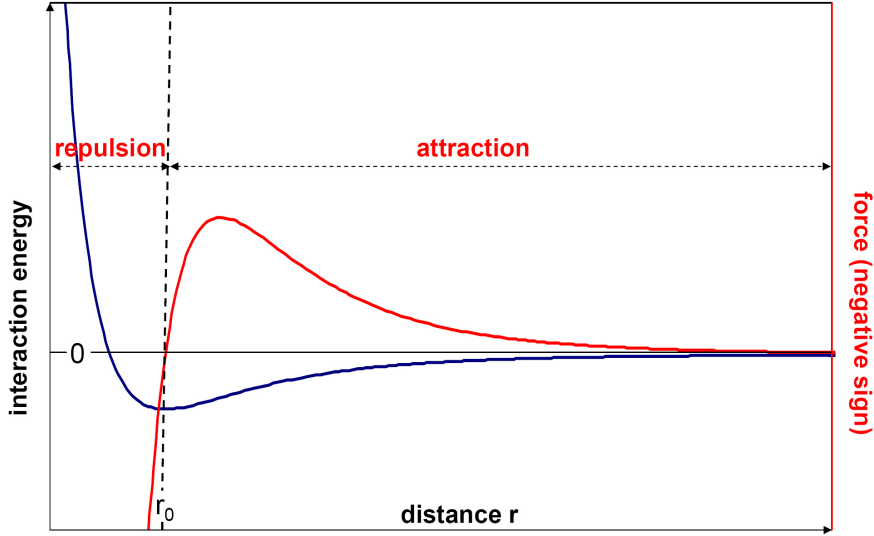


Figure 3.8: The Lennard-Jones-potential (blue) including vdW attraction and Pauli repulsion characterizes the potential energy of two particles as a function of their distance r . A stable minimum is reached at a distance r_0 . For $r > r_0$, the force (red) on the particles is attractive, whereas for lower separation distances it becomes repulsive due to the dominating r^{-12} part. For $r \gg r_0$ the attractive potential vanishes. Typical values for r_0 are in the range of a few \AA .

structures is still dipoles, the resulting energies and forces depend strongly on the geometry of the bodies [37] (Appendix C). In particular, the $V_{vdW} \propto -\frac{1}{r^6}$ behaviour of the vdW potential between two bodies can be lost. For example, the energy of two spheres with radii R_1 and R_2 changes into a $V \propto -\frac{1}{r}$ decay with their surface separation r according to:

$$V = -\frac{A_{12}}{6 \cdot r} \cdot \frac{R_1 \cdot R_2}{R_1 + R_2} \quad (3.16)$$

The material dependent Hamaker constant A_{12} describes the interaction strength between body 1 and 2 and is in the order of $A_{12} \approx 10^{-19} - 10^{-20} \text{J}$. A_{12} is a function of the Hamaker constants of the van der Waals interaction between equal components A_{ii} within each body. In real systems, the medium 0 between interacting bodies has to be taken into account. A_{12} merges into A_{012} :

$$A_{012} = \left(\sqrt{A_{11}} - \sqrt{A_{00}} \right) \cdot \left(\sqrt{A_{22}} - \sqrt{A_{00}} \right) \quad (3.17)$$

For positive Hamaker constants A_{012} , e.g. in vacuum ($A_{00} = 0$) or for identical bodies ($A_{11} = A_{22}$), the interacting force is always attractive. Depending on the medium, a repulsive van der Waals force occurs for $A_{11} < A_{00} < A_{22}$ or $A_{11} > A_{00} > A_{22}$, respectively.

3.2.2 Hydrogen Bonding

Molecules consist of two or more atoms which are connected by covalent bonds. Herein, atoms share up to three pairs of electrons to achieve the stable noble gas configuration in their valence shell. In the O_2 molecule for example four electrons are distributed equally among the two partners within a non-polar double bond. In contrast, if atoms within the molecule feature different electronegativities, a polar covalent bond is established [3]. In the extreme case of significant differences between the electronegativities, both electrons are preferentially located around one atom.

The attraction between different molecules is typically two orders of magnitude lower than experienced in covalent bonds ($436 \frac{kJ}{mol}$ for the covalent bond within the H_2 molecule (<http://www.science.uwaterloo.ca/~cchieh/cact/c120/bondel.html>)). A prominent intermolecular interaction is the hydrogen bond between molecules comprising polar covalent bonds. Electropositive H -atoms within the molecule exhibit a partial positive charge on the expense of an electronegative partner (often C , N , F), which is strongly attracting the electrons of the covalent bond. In the limiting case, an electronegative element withdraws electrons completely from the proton. Similar to the concept of vdW forces, the resulting dipole interacts electrostatically with its surrounding molecules. The high charge density of the remaining proton without screening electrons is able to attract and form tight bonds to (partially) negatively charged atoms or molecules ($\approx 10 - 40 \frac{kJ}{mol}$ [38]). Due to the small size of the proton and steric hindrance induced by the electron clouds of the reactants, access for more than one binding partner is limited. Hence, H -Bonding becomes a rather directional binding mechanism in contrast to common electrostatic interactions [36].

3.2.3 Water Structure and the Hydrophobic Force

The structure of proteins is significantly affected by the solvent. The exposure of side chains may induce the attraction or repulsion of water molecules depending on their hydrophilic / hydrophobic properties. Proteins are able to induce both water ordering or disordering while water molecules themselves may be a stabilising or destabilising factor for proteins. In this regard, water structure and ordering are introduced in this section in order to establish the concept of the hydrophobic effect as an essential contribution to protein stability.

The most familiar example for the effect of H -bonding is the structure of water. A water molecule comprises two partially positive charged hydrogens and two lone electron pairs at the oxygen atom, which participate in the binding of adjacent molecules. The number and strong directionality of its binding sites restricts the amount of partners for each water molecule to about four. Dependent on temperature and pressure, water can adopt different conformations in its crystalline state. Under ambient conditions and $0^\circ C$, each water molecule forms 4 hydrogen bonds leading to tetragonal "Ice I" (figure 3.9). This open cave-like structure is responsible for the lower density of ice compared to fluid water. Although an immense amount of literature was published within the last century, the structure of fluid water is still not completely understood. The most prominent theory

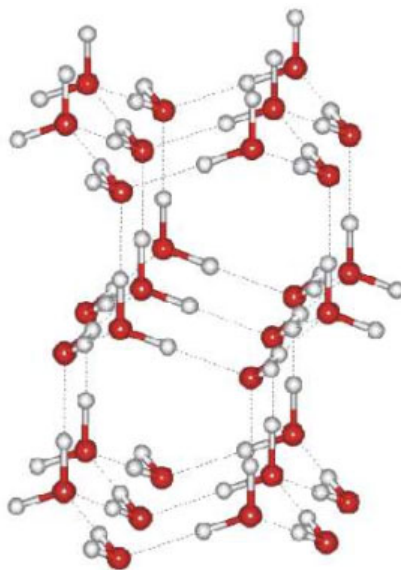


Figure 3.9: The structure of "Ice I" is identified by the perfect tetragonal structuring of water molecules. Each water molecule exhibits four binding partners by the formation of hydrogen bonds between its two lone electron pairs and two hydrogen atoms.

was introduced by Frank and Wen in 1959 [39]. They postulated the coexistence of ice-like clusters and a non-hydrogen bonded regime in a dynamic equilibrium above the melting temperature. Due to the geometry of the water molecule, its tendency to retain the ice-like tetrahedral structure is maintained in liquid water. So called "flickering (tetrahedral) clusters" with an average lifetime of about $10^{-11}s$ form and disappear continuously in a cooperative manner. The cluster size and the average number of H -bonds per water molecule are temperature dependent and contribute to water properties like viscosity or surface tension. Whereas cluster size and fraction of unbroken hydrogen bonds decrease from $0^{\circ}C$ to $100^{\circ}C$, the cluster concentration increases. It is important to note that both cluster size and the fraction of hydrogen bonded molecules do not vanish at the boiling point [40]. The properties of water depend strongly on any substance affecting its hydrogen bonding pattern. A biological relevant example is given by the interaction of ions and water. According to their charge density, ions can have both an ordering and disordering effect on water structure. Water dipoles in the vicinity of an ion face an electrostatic force while the interaction with bulk water adds the tendency to form hydrogen bonded tetrahedral structures [41]. In this regard, small or multivalent ions with strong electric fields (structure makers, antichaotropes or kosmotropes) are able to align water dipoles and contribute to water ordering while large ions break the water structure (chaotropes) [39]. A measure for this ordering effect is the viscosity

change due to the presence of ions in fluid water:

$$\frac{\eta}{\eta_0} = 1 + A \cdot c^{\frac{1}{2}} + B \cdot c \quad (3.18)$$

The viscosity of pure water η_0 changes into η as a function of the ion concentration c . The concentration-independent constant A accounts for counterion screening effects according to the Debye Hückel theory [42]. B quantifies the degree of water ordering. It comprises a positive sign for a kosmotrop and changes to negative values for less structuring chaotropic ions. Hence, viscosity enhancements can be regarded as a measure for water ordering.

A simple yet successful and instructive model for water ordering was introduced by Ben-Naim in 1971 [43]. In his two dimensional Mercedes-Benz (MB) model each water molecule is given by a flat rigid disk interacting with adjacent water disks over orientation-dependent hydrogen bonds. The hydrogen bonding sites in 2D are given in figure 3.10 by three radial arms similar to the Mercedes-Benz emblem. Among a row of other water characteristics, it perfectly describes the dependence of water ordering on ion size and the sign of its electric charge. The latter effect is caused by an asymmetry in the water dipole. The negative end of the dipole is located at the molecular centre whereas the positive one is closer to the disk's surface. Hence, anions exhibit a stronger ordering effect on water molecules due to an increased electrostatic interaction compared to cations with identical absolute charge values and radii.

Non-polar molecules, e.g. hydrocarbons, also induce structural reorganization in adjacent water molecules due to their disability to participate in hydrogen bonding. Whereas water molecules are able to form cave-like structures around small non-polar molecules with diameters of up to several Å by slightly bending their tetrahedral structure, potential H -bonding sites are lost for bigger molecules (figure 3.11). In order to minimize their energy, water molecules reorient to achieve a maximum of H -bonding partners when facing non-polar solutes. This reorientation induces a higher degree of order into the system and decreases its entropy. An instructive example may be the solvation of *n*-butane in water at room temperature [36]:

$$\Delta G = \Delta H - T\Delta S = -4.3 \frac{kJ}{mol} + 28.7 \frac{kJ}{mol} = 24.5 \frac{kJ}{mol} \quad (3.19)$$

The change in free enthalpy ΔG of the system by incorporating the alkane into the water structure comprises an unfavourable positive value although the enthalpic part ΔH still favours solvation. Due to the reorientation of water molecules the entropy part $T\Delta H$ dominates over the mixing enthalpy, thus, making dissolution highly unfavourable. Non-polar substances which show a very poor solubility in water for entropic reasons are referred to as hydrophobic molecules.

Schellman introduced the solubility of hydrophobic molecules itself as a measure for the strength of the hydrophobic interaction [45]. His model is able to explain the temperature dependence of the hydrophobic interaction by comparing the solubility (and hence the equilibrium concentrations) of a hydrocarbon in water ρ^w with that in a hydrophobic reference state ρ^r . Instead of focussing on energy relations, Schellman suggests to

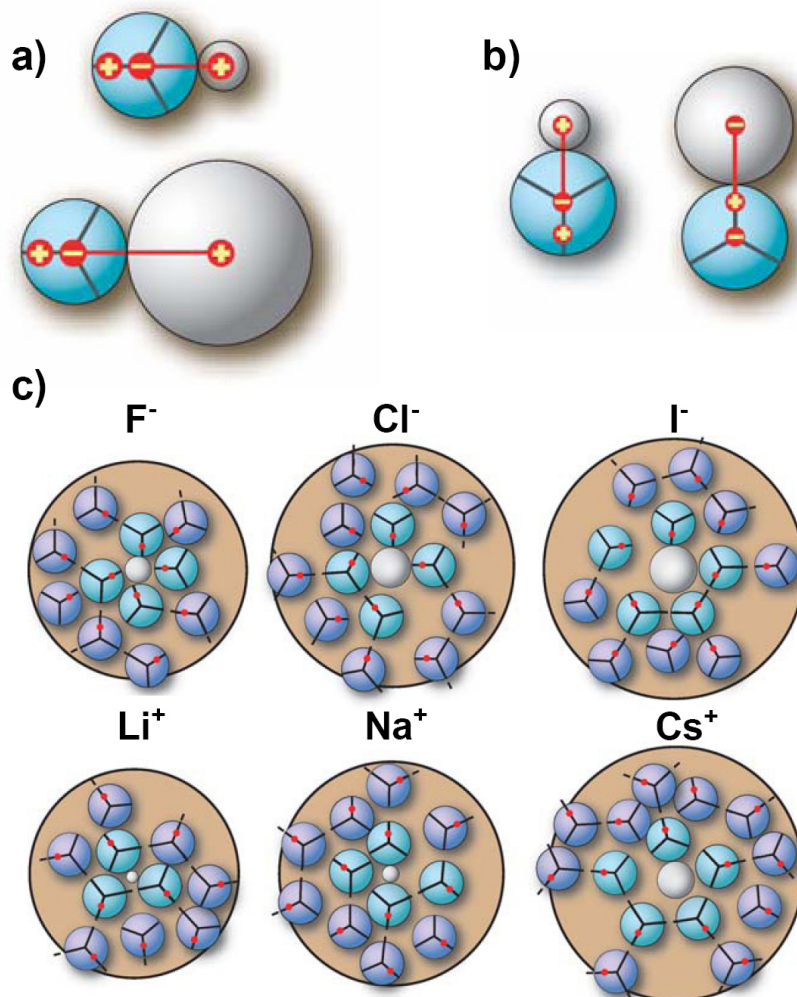


Figure 3.10: In the MB model water molecules are described as two dimensional disks including a dipole moment and three arms for in plane hydrogen bonding. In a) both the orientation of the water dipole to a cation and its dependence on the ion size are illustrated. b) According to the charge of the ion, the dipole of MB water is orientated. c) Around a small ion with its high charge density, water molecules are predominantly aligned electrostatically. In contrast, large ions like I^- or Cs^+ comprise weaker electrostatic fields and water molecules arrange in the favourable hydrogen bonding structure of bulk water (e.g. a hexagonal structure in 2D in contrast to a tetrahedral structure in 3D). The red dots on the water discs indicate the positive end of the dipole. This figure is taken from [42].

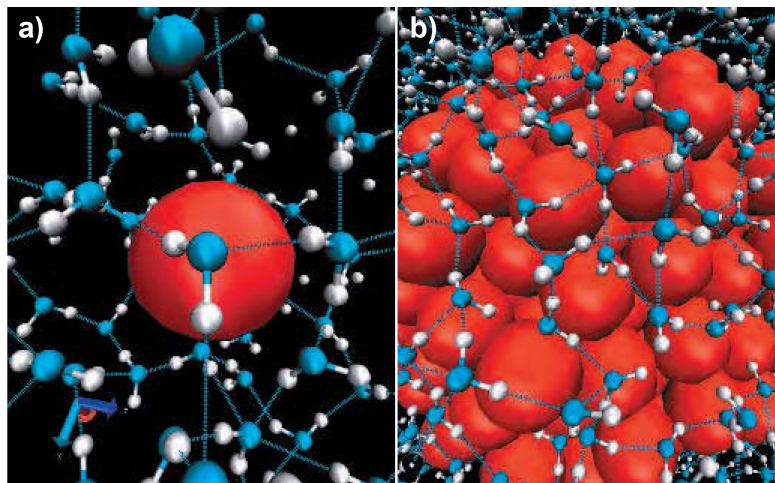


Figure 3.11: In this molecular-dynamics simulations, water molecules near hydrophobic cavities are modelled by blue and white particles representing oxygen and hydrogen atoms, respectively. The dashed lines indicate hydrogen bonds. The space-filling size of the hydrophobic (red) particle in a) is similar to that of a methane molecule. The hydrophobic cluster in b) contains 135 hexagonally close-packed particles that forms a roughly spherical unit of radius larger than $1nm$. In both cases, the water molecules shown are those that are within $0.8nm$ of at least one methane-like particle. For the single cavity pictured in a), each water molecule can readily participate in four hydrogen bonds (owing to thermal motions, hydrogen bonding in liquid water is disordered). In b), the cluster is sufficiently large that hydrogen bonds cannot simply go around the hydrophobic region. In this case, water molecules near the hydrophobic cluster have typically three or fewer hydrogen bonds. This figure is taken from Ref. [44].

consider $\frac{\Delta G}{T}$ with its direct relation to the probabilistic view of a Boltzmann distribution:

$$\frac{\rho^w}{\rho^r} = \exp\left(-\frac{\Delta G}{RT}\right) \quad (3.20)$$

Maintaining hydrogen bonds in the vicinity of a hydrophobic solute becomes less important for higher temperatures. Therefore, the entropic part ΔS increases with temperature as the amount of hydrogen bonded water molecules in the bulk decreases. ΔS approaches zero at a temperature T_S (above the boiling point of water!) when water molecules lose their tendency for hydrogen bonding completely. ΔH is also an increasing function, equals zero near room temperature and comprises a positive sign in the high temperature regime (figure 3.12). ΔH is actually a sum of two enthalpy contributions. The first summand consists of the large positive (and hence energetically unfavourable) mixing enthalpy and comprises only weak temperature dependence. It results basically from the energy for cavity formation accompanied by the breakage of hydrogen bonds

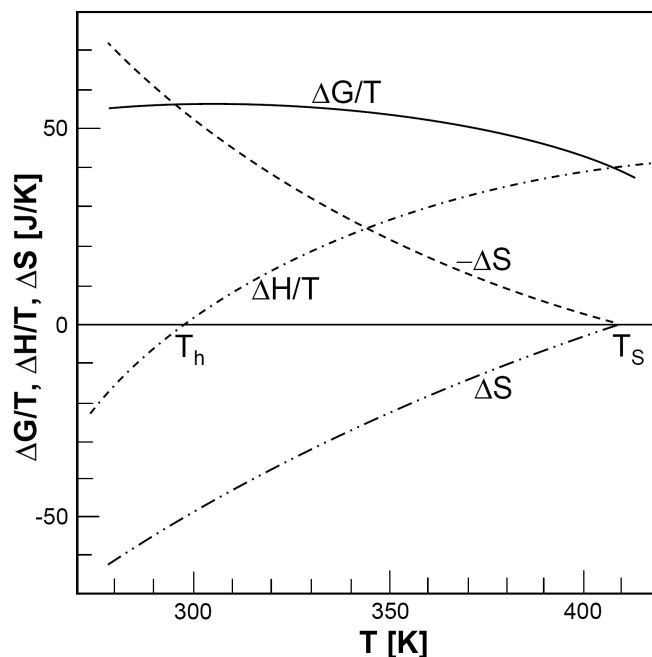


Figure 3.12: The contributions $\Delta H/T$ and ΔS to the total energy of liquid benzene in water are illustrated as a function of temperature. $\Delta G/T$ exhibits a maximum and thus a solubility minimum of the hydrocarbon in water around room temperature. This figure is taken from [45].

due to the incorporation of the hydrophobic solute and involves significant changes in the number of molecular interactions within the regular water structure. This part of ΔH decreases slowly with increasing temperature analog to the amount of hydrogen bond breakage in pure water. Nevertheless, a rather large positive value still remains. The second part arises from the induction of structure within the water molecules due to the hydrophobic solute (hydration of the solute) and increases steadily with increasing temperature. It exhibits a large negative value at room temperature and equals 0 at about 140°C , where the tendency of water structuring is lost completely due to destructive thermal energy [46]. Taken together, these two enthalpy parts annihilate each other near room temperature. ΔH or $\frac{\Delta H}{T}$, respectively, cross zero approximately at room temperature and comprising positive values for higher temperatures. Combining the observations for the entropy and enthalpy, $\frac{\Delta G}{T}$ exhibits a maximum and thus a solubility minimum of hydrocarbons in water around room temperature.

It is noteworthy, considering only the hydration of a hydrophobic solute, the energetically favourable enthalpy term would induce the dissolution of an extended cluster consisting of single hydrophobic particles (figure 3.11b). Such a favourable wetting of hydrophobic substances is in conflict with our common understanding and emphasises the necessity to take a comprehensive thermodynamic view on the hydrophobic effect including both mixing enthalpy and entropy contributions.

3.2.4 Biophysical Sensing

Interactions in real systems are not limited to single molecules or atoms but involve extended surfaces. The precise knowledge of possible interaction mechanisms of VWF to solid surfaces, membranes or other VWF polymers will provide the basis to assign certain patterns to their physical origin (see also chapter 5.2.2). An excerpt of fundamental interaction forces is given in this section.

The force between surfaces, macroscopic particles or an Atomic Force Microscopy (AFM) tip with a sample is given by the derivative of the underlying interaction potential U with respect to the distance r :

$$F = -\text{grad}(U) \quad (3.21)$$

On the following pages, the main contributions to the interaction potential U in a fluid buffer environment will be listed with special regard to biophysical sensing in AFM measurements (see also chapter 4 and 5.2.2). These include van der Waals (vdW) -, electrostatic -, double layer -, oscillatory -, hydration -, hydrophobic - and steric forces.

vdW forces are generally considered first, when specifying the contributions to the cantilever deflection. This kind of interaction is strongly dependent on the geometry of the tip and the material of the cantilever, the surface and medium [37]. An appropriate choice of the relations between the Hamaker constants of tip, medium and surface can enhance, reduce or even eliminate vdW forces. In the case of Si_3N_4 tips, like they were commonly used in our experiments, a medium change from water to ethanol decreases the attractive forces on a mica surface by an order of magnitude [47].

Furthermore, silicon nitride as well as glass and mica are known to carry negative surface charges under water conditions [48]. The charging of a surface arises either from the dissociation of surface groups or the adsorption of ions. Scanning a charged surface with a charged tip will expose the charge distribution of the sample rather than its height profile and therefore may easily lead to delusive results. Tip and surface charge and hence both the strength and the sign of the electrostatic interaction can be effectively regulated by tuning the pH of the solution [49]. In biological buffer systems containing a variety of salts at different concentrations, the electrostatic fields of both tip and surface are screened by free ions. Most of the screening counterions are located within $1nm$ to the surface forming an electric double layer at the fluid-solid interface (figure 3.13). The actual counterion distribution follows Boltzmann's law and generates an exponentially decaying electric field with a typical decay length k (Debye length). k is significantly influenced by the ion concentration and decreases from about 10 to $1nm$ when the concentrations of monovalent ions increases from $1mM$ to $100mM$ [36]. Divalent ions have an even more pronounced effect on screening surface charges and lowering the electrostatic potential. Double layer forces between two similarly charged surfaces are always repulsive [50] and emerge from osmotic rather than electrostatic effects. The origin of the double layer is found in the balance between electrostatic attraction and osmotic repulsion. Ions are electrostatically attracted to the oppositely charged surface and experience an osmotic gradient towards the diminished bulk ion concentration. When two surfaces with similar double layer structures are brought into close contact, the counterions are forced to move towards the surfaces against their osmotic gradient resulting in

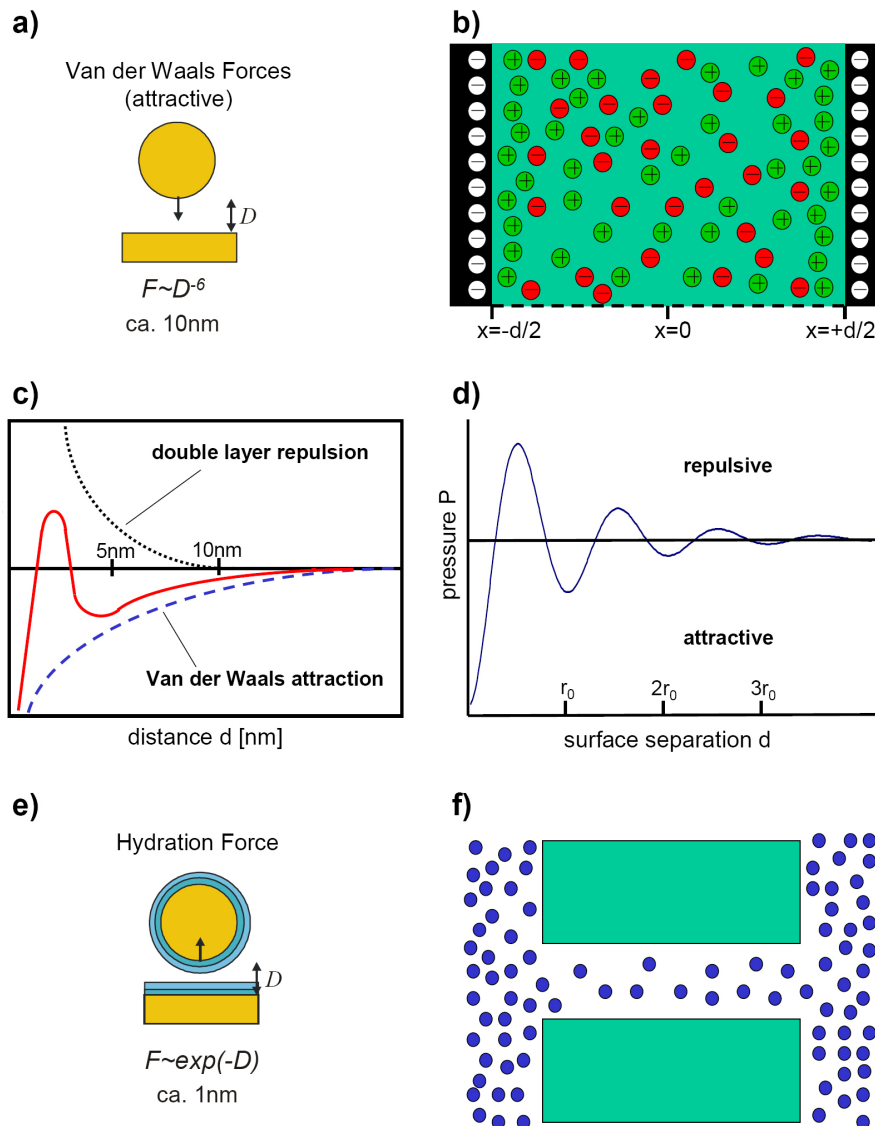


Figure 3.13: Van der Waals Forces typically decay within 10nm in a fluid medium. b) Counterions accumulate at charged surface. The density of the counterion exhibits an exponential decay $\rho = \rho_0 \cdot \exp(-k \cdot |x|)$ with the bulk density of counterions ρ_0 and the decay length k (k is only a function of the surface potential and ion valence). Decreasing the distance d between two similar charged surfaces leads to a repulsive double layer force. c) In combination with the attractive vdW interaction, the double layer repulsion forms the so called DLVO interaction potential (red) exhibiting a secondary minimum and a global minimum which is separated by a repulsive barrier. The height of this barrier decreases with increasing salt concentration. d) In the absence of ions, two approaching surfaces may experience an oscillatory force with varying sign according to the packing density of the fluid molecules. r_0 is in the range of 3\AA for water molecules. e) Hydration forces arise from the dehydration of ions when two surfaces come into close contact (exponential decay within several \AA). f) Similar, the attractive hydrophobic force originates from a decrease in water density in between hydrophobic surfaces at distances up to 10nm.

a repulsive force.

Ions themselves can induce short range repulsion due to their ability to align water molecules (see also chapter 3.2.3). A repulsive force arises when two surfaces reach a separation distance corresponding to the radius of a hydrated ion. Further approach induces an energetically unfavourable state by the impelled dissociation of ions from their bound water molecules [49]. In the absence of ions, water density differences at atomically flat surfaces may lead to an oscillatory force. Oscillatory forces do not require any attractive liquid-liquid or liquid-wall interaction. Fluid molecules are ordered in layers with varying packing density as a function of the surface separation. Hence, an AFM tip, which approaches a surface, experiences alternating attraction and repulsion (figure 3.13) going along with an alternating density profile. The wavelength of this force is determined by the size of the molecules. The density and repulsion maxima arise at separation distances of multiple integers of the fluid molecules size. In between, the packing density decreases and the surfaces are attracted (for details see Ref. [36]). Similarly, hydrophobic surfaces experience an attractive interaction due to a decrease in water density in between the surfaces. The interaction range is distinct longer compared to the oscillatory force. Typically, hydrophobic forces decay exponentially with a characteristic decay length of 1 to $2nm$ between 1 and $10nm$ [51]. Besides these various kinds of interactions, any coating of the surfaces with polymers, antibodies and other molecules can cause both steric repulsion or specific and non-specific attraction.

In summary, the interaction potential U and therefore the force between AFM tip and sample can be very complex involving variable interactions. Depending on the question under investigation, the adequate choice of medium, salt concentration and tip modification can minimize the forces on the sample in order to prevent its deformation or even destruction while enhancing the imaging contrast at the same time.

4 Materials and Methods

A key in the understanding of life science is hidden in the interaction of various kinds of molecules. In biology, these processes frequently involve the reduction of reactions from three to two dimensions, i.e. surfaces. In order to mimic and analyse such processes, interplay of various methods with each contributing its part to a unifying picture is required. Within this variety of techniques, the measurements performed with the multifunctional Atomic Force Microscope (AFM) have outstanding character for the unravelling of numerous secrets of blood clotting. After the illustration of possible interaction forces of an Atomic Force Microscopy (AFM) tip with surfaces in the last chapter, the principles and benefits of the AFM will now be reflected. This is accomplished with special regard to the investigations of VWF covered biological surfaces presented in the results part of this thesis. The last part of this section introduces a potent hybrid system combining the advantages of optical microscopy, Surface Acoustic Wave (SAW) driven microfluidics and Atomic Force Microscopy. The development of this hybrid system within the framework of this thesis provided an optically and mechanically accessible blood vessel for the investigation of blood clotting under dynamic conditions.

4.1 Atomic Force Microscopy

Similar to a turn table player, an Atomic Force Microscope translocates a needle over a surface in order to quantify height changes. Whereas measured data within a gramophone are converted into an acoustic signal, an AFM creates a topographic image of the surface. With a lateral resolution down to the range of atoms [52], an AFM outplays a gramophone by several orders of magnitude. However, the function of an AFM is not limited to imaging techniques. The high resolution in the subnanometer regime coupled with a minute control for tip displacement allows both the measurement of marginal interaction forces and the precise manipulation of matter in the nm and μm range [53, 54]. In the next sections, the basic principles of the AFM technique will be sketched including AFM Force Spectroscopy measurements and the imaging modes used in this thesis.

4.1.1 Setup and Basic Principle

The heart of every AFM setup is a cantilever with a sharp tip at its end. After positioning of the probe above the sample by an optical microscope, it is lowered to the surface by a piezoelectric motor, which is controlled by an automated feedback system. Parameters such as scan area, probe force and scan rate are input into the system before the scan is put into motion. The cantilever arm itself can be modelled as a spring with stiffness k [55]. According to Hook's law, the interaction force F between tip and surface is directly

related to the mechanical displacement of the cantilever x :

$$F = k \cdot x \quad (4.1)$$

In order to quantify the cantilever deflection, laser light is reflected off the shiny top surface of the cantilever into a photodiode detector (light-detection method). Using a "4 Quadrant" photodiode, both lateral and vertical deflection, e.g. bending and torque of the cantilever can be analyzed. The lateral resolution is given by the radius of curvature of the tip in first place which is in the range of 10 to 50nm for most of the commercially available tips.

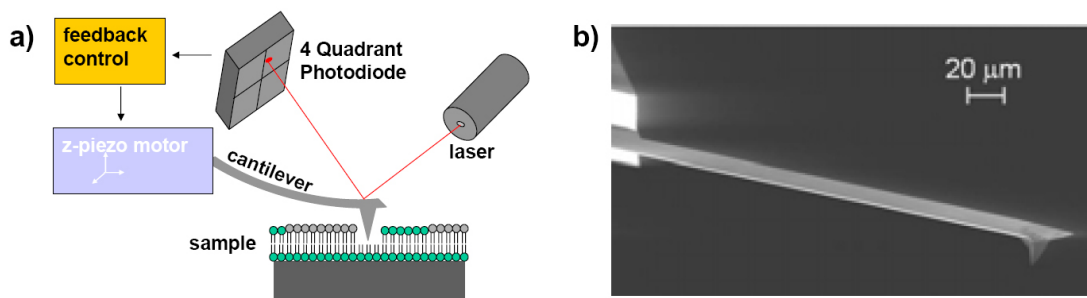


Figure 4.1: a) The scheme illustrates the principle setup of an AFM scanning a rough surface. The deflection of a cantilever arm due to the interaction of the tip with the surface is analysed by the change of the signal of a laser beam on a 4 Quadrant photodiode. This signal is converted into a topographical image of the surface. A feedback loop controls a piezo motor which moves the cantilever tip up and down according to the surface topography. b) The cantilever arm with the tip at its end is the force sensitive part of the AFM.

The signal at the photodiode can be enhanced by coating the upper side of the cantilever with a reflecting metal. However, such a composition is very sensitive to minute temperature changes causing long equilibration times and cantilever drift before and during measurements. In most AFM setups a mirror in between tip and photodetector allows to position the laser spot directly into the middle of the diode and to account for different refractive indices of different media. Cantilevers are available in a multitude of geometries, force constants and resonance frequencies. Dependent on the sample and the question under investigation, the choice of the appropriate cantilever and tip is the most important step towards maximum performance of the system.

4.1.2 Atomic Force Spectroscopy

In AFM Force Spectroscopy, the cantilever tip is used as a tactile sensing tool for the interaction forces with a single point of the surface. In this mode, the base of the cantilever is moved in vertical direction towards the surface and retracted again. The cantilever

deflection as a function of z-piezo position is monitored in so called force - distance cycles (figure 4.2). It can be roughly divided in the non-contact region, the contact

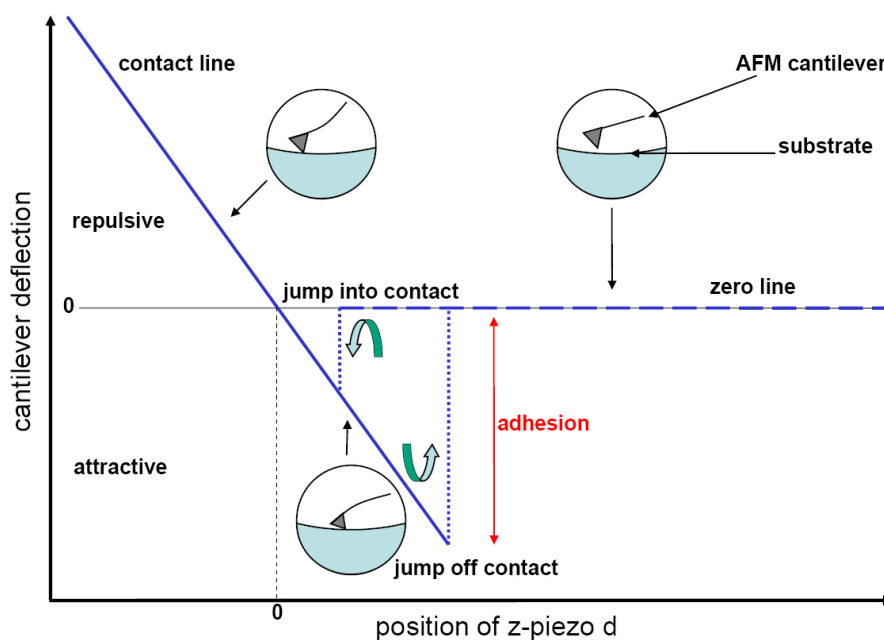


Figure 4.2: A typical force - distance cycle displays the cantilever deflection as a function of the position of the z-piezo (NOTE: The position of the z-piezo equals the distance between tip and surface only in the unbended state!). It can be roughly divided in the non-contact region, the contact line and the null line. The rupture forces are statistically analysed using custom-designed evaluation software [56].

line and the null line [58]. Null or base lines are obtained when the tip is far apart from the sample and there is approximately no cantilever deflection. A shift in the null lines may give information about the viscosity of the solvent when working in liquids. The tip contacts the sample at the intersection between null- and contact line ($d = 0$). Further approach of the z-piezo leads to an upward bending till a preset contact pressure is reached. In between null- and contact line, the non-contact region displays the interaction properties of tip and sample. Close to the surface ($d > 0$), the tip might abruptly "jump into contact", when attractive interaction forces overcome the cantilever stiffness [59]. Similarly, the adhesion is overcome at the "jump off contact" point upon retraction. The rupture force, which is proportional to the distance between the peak and the null line, is commonly evaluated as a measure of the interaction strength between tip and sample. For maximum force resolution, soft cantilevers with force constants $k < 0.1 \frac{mN}{m}$ are frequently used. The adhesion work for both jump into contact and jump off contact equals the area between the negative part of the approach or withdrawal curve, respectively, and the null line. The shape of the contact line as well as the non-contact region

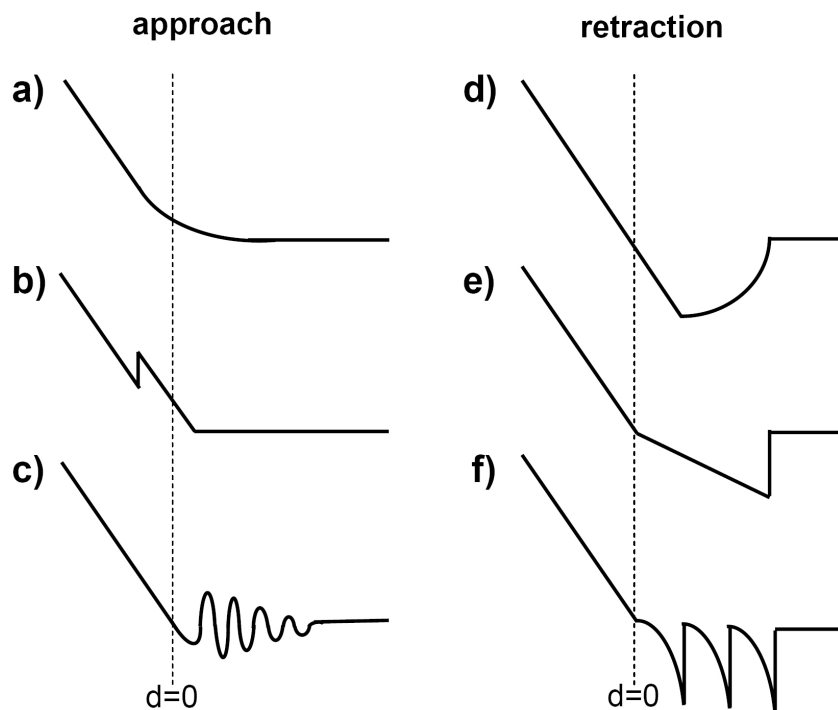


Figure 4.3: Any deviation of both approach and retraction curves from the typical force - distance cycle in figure 4.2 includes information about the special kind of tip - sample interaction. a) A smooth increase of the approach curve before contact to the solid surface at $d = 0$ indicates repulsive interaction, e.g. electrostatic repulsion (not shown: the same holds for a decrease of the curve as a result of an attractive interaction). On a different length scale, the indentation of a soft sample by the AFM tip displays similar characteristics. b) The squeezing of a stiff but penetrable layer (e.g. phospholipid membrane) on the solid surface may result in an additional peak in the contact line. The cantilever contacts the membrane (at $d =$ membrane thickness) and penetrates it at a threshold force. c) Oscillatory forces may arise within a few molecular diameters between tip and sample (see also chapter 3.2.4). The retraction displays the adhesive properties between tip and sample. d) If hydrophobic forces dominate the tip sample interaction, the jump off contact is replaced by a rather smooth convergence of the cantilever deflection to the null line. e) Smaller slopes of the non-contact in comparison to the contact regime indicate the bending of a soft material between tip and surface. f) Unravelling of protein samples between tip and substrate increases the effective length of the polymer. The entropic elasticity of the protein can be formally described by the worm-like chain model [57]. The interactions reflected in a) - f) (including jump into contact) may be present at the same time.

may provide valuable information on sample stiffness and the kind of interacting forces. The origin of various force - distance cycles is discussed in figure 4.3.

In recent years, AFM Force Spectroscopy became a powerful tool in investigating minute interaction forces within biological systems by applying improved tip chemistry for the immobilization of a broad spectrum of molecules onto the AFM tip. Quantitative and qualitative information of the elasticity of single molecules [60], conformational transitions in proteins [61], mechanical stability of secondary structure elements [57], stability of chemical bonds [62] or the adsorption and desorption energies [63] could be obtained. An interesting expansion of pure force distance cycles is the "Force Mapping" method. In Force Mapping, single force-distance curves are recorded along a predefined grid. On each point, the rupture events are analysed and combined to a map displaying the interaction strength between functionalized tip and surface [64]. A combination of Force Mapping and imaging is the force recognition imaging. The AFM tip with an immobilized antibody scans biological surfaces for specific lock and key interactions with its corresponding antigen [65].

4.1.3 Imaging Modes

In contrast to Force Spectroscopy measurements, the purpose of AFM imaging is the development of a topographical picture rather than the recording of interaction forces at selected points on the surface. A rough division is made between static and dynamic imaging modes. The latter include oscillations of the cantilever which reduce the direct contact and therefore the forces between tip and surface. Among other things, the choice of the appropriate imaging mode depends on several factors like convolution effects, sample elasticity, adhesion properties and medium. In the present work (section 5.2.2), contact and intermittent contact mode imaging was used and is described in the following section.

Contact Mode Imaging

Contact mode operates in the repulsive part of the Lennard-Jones potential (see chapter 3.2.1) and is a rather straight forward way of analysing the height profile of a sample. The tip is brought into direct contact to the surface. Line-by-line scanning cycles are performed either at a constant deflection of the cantilever (constant force mode) or at constant height of the z-piezo above the surface (constant height mode). The constant height mode is generally not favourable for biological samples with pronounced height differences of dozens of nm and beyond. Force constants for contact mode imaging in fluids are typically in the range of $k \approx 7 - 40 \frac{mN}{m}$ [66]. These cantilevers exhibit a sufficient balance between susceptibility for thermal noise and sensitivity to account for minimal height differences of the sample. Contact mode is generally a very robust way of imaging surfaces against external errors such as height changes or artefacts. On the other hand, soft samples may be indented and modified by the scanning process itself. Especially when working with adhesive material, a pronounced disadvantage is the sticking of matter to the tip which normally requires the replacement of this cantilever. Furthermore,

lateral forces can lead to displacement or destruction of soft or loosely bound samples. These conditions already lead to disqualification of this method for a variety of biological samples. Some of the disadvantages can be overcome with dynamic imaging modes.

Intermittent Contact Mode

In order to prevent indentation or even destruction of soft samples by a permanent application of large vertical and lateral forces, both the force and the contact time of the cantilever to the surface should be reduced. In intermittent contact mode the cantilever performs continuous oscillations close to its resonance frequency (typically in the range of tens of kHz for measurements in fluids [66]) within the repulsive and attractive part of the potential. Within an oscillation, the surface is only briefly at its reversal point. This reduces most of the lateral forces responsible for the displacement of parts of the sample and enables even scanning of pronounced height differences. The choice of the appropriate cantilever is still a compromise between basically two considerations. The force constant has to be small enough to assure satisfactory force resolution. At the same time, it must be high enough to maximize the resonance frequency in order to be insensitive against thermal fluctuations (the cantilevers used in the experiments are found in Appendix A).

The control variable in this modus is the maintenance of constant oscillation amplitude at a constant driving frequency. Far from any surface, the cantilever (effective mass m_{eff}) deflection displays harmonic oscillation $z(t)$ induced by an external sinusoidal driving force with amplitude F_0 and frequency ω :

$$m_{eff} \cdot \ddot{z} + \alpha \cdot \dot{z} + k \cdot z = F_0 \cdot \cos(\omega \cdot t) \quad (4.2)$$

The second term on the left side denotes Stokes friction (friction coefficient α). A sine function with phase φ solves this differential equation:

$$z(t) = A \cdot \sin(\omega \cdot t + \varphi) \quad (4.3)$$

with amplitude $A = \frac{F_0}{m_{eff} \cdot \omega_0^2} \frac{\omega_0^2}{\sqrt{(\omega_0^2 - \omega^2)^2 + \left(\frac{\alpha \cdot \omega}{m_{eff}}\right)^2}}$ and phase $\tan \varphi = \frac{\alpha \cdot \omega}{m_{eff} \cdot (\omega_0^2 - \omega^2)}$ with the eigen-

frequency of the cantilever $\omega_0 = \sqrt{\frac{k}{m_{eff}}}$. In the vicinity of a surface, the harmonic oscillator experiences an additional force due to the interaction potential of the tip and the sample. Although an analytical solution of equation 4.2 is not possible any more, numerical calculations demonstrate a shift of the resonance peak towards smaller frequencies for constant damping α . Within a measurement in intermittent contact mode, the driving frequency is chosen in the left flank of the resonance peak under bulk conditions. When approaching the surface, the resonance peak is shifted to smaller values and the amplitude of the cantilever oscillations increases. The feedback control removes the cantilever from the surface to assure constant amplitude. The choice of the amplitude setpoint defines the force on the sample. A high amplitude setpoint minimizes the contact between tip and surface and therefore possible sample destruction. Hence, constant

amplitude of the oscillation requires constant distance to the surface. The movements of the z-piezo induced by the feedback control yields the height image of the surface.

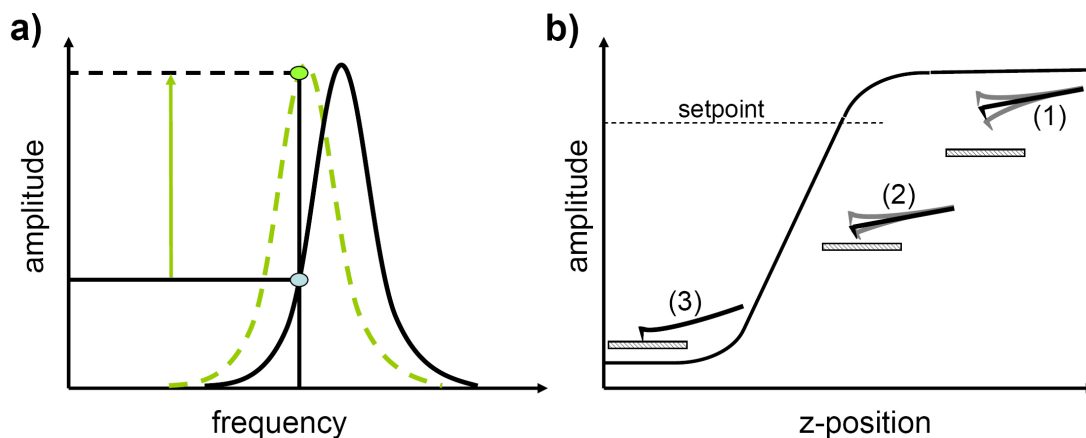


Figure 4.4: The interaction of the tip with the surface shifts the resonance peak towards lower frequencies. Hence, due to the choice of the driving frequency in the left flank of the peak, the amplitude of the oscillation increases. b) The amplitude for a free oscillating cantilever is maximal (i). When the cantilever contacts the surface, the amplitude is reduced due to the interaction with the surface. Further approach reduces the amplitude till the cantilever is directly on the surface. The setpoint of the amplitude is generally chosen to be in a regime where the cantilever is able to perform a major part of its oscillation circle.

An additional benefit compared to contact mode scans is the analysis of the phase information. During an experiment, the cantilever is driven near its resonance frequency and vibrates with the same frequency. Dependent on the conditions of tip and sample, there will be a phase shift between the drive signal and the cantilever movement. This phase shift is sensitive to the properties of the sample. It is directly related to the dissipated energy within the repulsive part of the interaction and yields valuable information about material properties of the surface even in the absence of height differences.

4.2 The Lab on a Chip - AFM -Hybrid

Atomic Force Microscopy has proven to be a fruitful tool to investigate biological question by applying rather static imaging methods and force measurements. In order to provide a more detailed insight into the structural and dynamic properties of VWF, the conventional AFM was extended to account for VWF's hydrodynamic properties (section 3.1.4). Within the framework of this thesis, a Surface Acoustic Wave (SAW) driven microfluidic reaction chamber was integrated into an AFM mounted on an inverted optical microscope. This unique hybrid system demonstrated its ability to cope with the secrets of an equally unique protein under both static and dynamic conditions. On the following pages, the excitation of acoustic streaming in fluids by Surface Acoustic Waves

(SAWs) will be reflected. Ultimately, the SAW actuation unit will be integrated into an Atomic Force Microscope forming the Lab on a Chip - AFM - Hybrid. Specific applications of this system in stream line tuning, VWF adhesion and network manipulation are found in the results-part of this thesis (chapter 5).

4.2.1 Surface Acoustic Wave (SAW) driven Microfluidics

Microfluidic applications including commonly used flow chambers are often confined by the limited performance of tubes, valves and actuation techniques in handling small sample volumes [67]. Direct contact of mechanical parts with the sample gives rise to contamination, limits the accessibility of the system and is not feasible for expensive or rare sample materials due to the necessity to operate in the *ml* regime [68, 69].

Surface Acoustic Wave (SAW) driven microfluidics can overcome these problems. This technique is based on the interaction of a SAW on a piezoelectric material and a fluid at its surface. In order to induce fluid movement, a so called Rayleigh wave is excited on $LiNbO_3$ by applying an alternating high frequency voltage on interdigital transducer (IDT) electrodes (for details see Ref. [70]). Rayleigh waves oscillate in an out-of-plane movement including both longitudinal and transversal components. An IDT structure is deposited on top of the substrate using standard lithography. The distance $\frac{\lambda}{2}$ between two fingers of the electrodes is chosen in the order of several μm and determines the excitation frequency f of the SAW with a material dependent propagation velocity c_{SAW} :

$$f = \frac{c_{SAW}}{\lambda} \quad (4.4)$$

The corresponding SAW frequencies generally range between hundreds of MHz . Since the SAW is basically a sound wave travelling along a solid / air interface with poor impedance coupling (high difference in sound velocity), little energy is dissipated in this mode. However, when a SAW encounters a liquid placed on the upper half-space of the chip (figure 4.5 b), energy is transmitted into the liquid due to the better matching of the sound velocity between the solid and the liquid [71]. As a result of the viscous attenuation, the amplitude of the SAW decays exponentially within the liquid with a characteristic length scale of a few μm (leaky SAW). The radiation angle θ_R of the leaky SAW depends solely on the sound velocities of the substrate v_S and the fluid v_F [72]

$$\theta_R = \arcsin\left(\frac{v_S}{v_F}\right) \quad (4.5)$$

In addition, the SAW creates a pressure gradient in the direction of the sound propagation leading to fluid streaming along the radiation axis [73].

By means of optical lithography a broad variety of different hydrophobic / hydrophilic channel structures and with it also a broad variety of different flow patterns can be processed onto the chip substrate.

4.2.2 The Hybrid System

The completely planar SAW driven fluid actuation system enables the technological freedom to create a continuous flow in any desired geometry (artificial blood vessel)

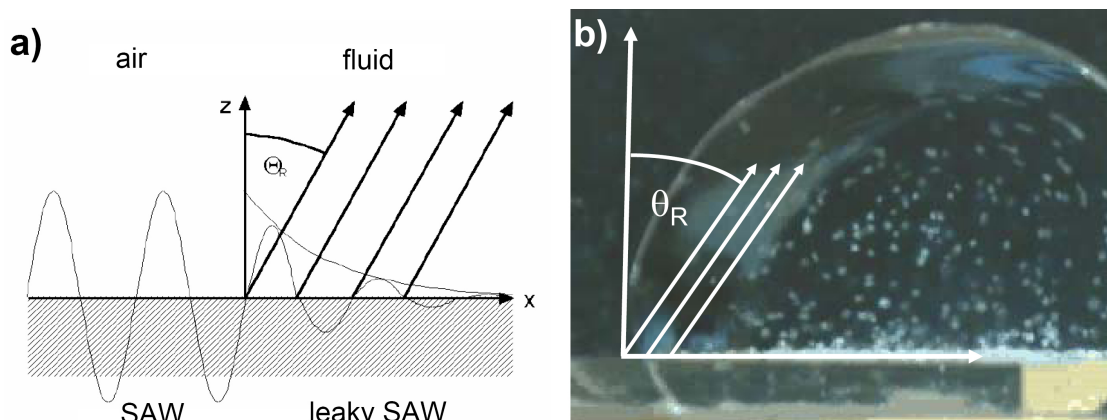


Figure 4.5: a) The SAW is propagating from left to right (amplitude $\approx 1nm$), and hits the liquid at $x = 0$. Due to the viscous attenuation, the amplitude of the SAW decays exponentially in the liquid. The leaky SAW creates a longitudinal sound wave, which is radiated into the fluid under a refraction angle θ_R . b) A leaky SAW induces fluid streaming in the droplet. The movement of the beads perfectly illustrates the refraction angle θ_R . This figure is taken from [74].

[71]. No drain and hence no supply is necessary, which allows investigating the identical solution of proteins, cells, vesicles, etc. without the loss of material or a change in any crucial parameter for long periods of time ($\approx 1h$). The planar setup, providing full optical accessibility of the light path between AFM tip and the fluidic track, is completed by an inverted microscope for recording the microfluidic channel and the AFM tip simultaneously [75]. This control system enables the online monitoring of any accessible event and thus provides the possibility for an immediate response with the AFM to every important change of the system. Additionally, optical images of stained samples to a height profile for instance can facilitate data interpretation. In this regard, optical microscopy provides a direct reference system for AFM results. Our hybrid system combines the advantages of three different experimental approaches and does not simply serve as an inbuilt reference systems. The assembled techniques supply information from different perspectives for the same question creating a unique and more complemented picture of the scientific problem.

This SAW driven artificial blood vessel provides the ground for testing variable blood flow conditions by applying adjustable shear stress. Although the fluid streaming induces a lot of vibration on the cantilever and hence too much noise for simultaneous imaging, force spectroscopy under certain circumstances is still possible. Nevertheless our setup provides distinct advantages in imaging too. In measurements of the time course of stimulated sample alterations, several problems have to be overcome. One is the time scale till a reagent shows an impact on the sample. Another is the recovery of the region of interest (ROI) after this impact has taken place. Whereas chemical interactions such as changes in pH or salt concentration can be obtained without moving either

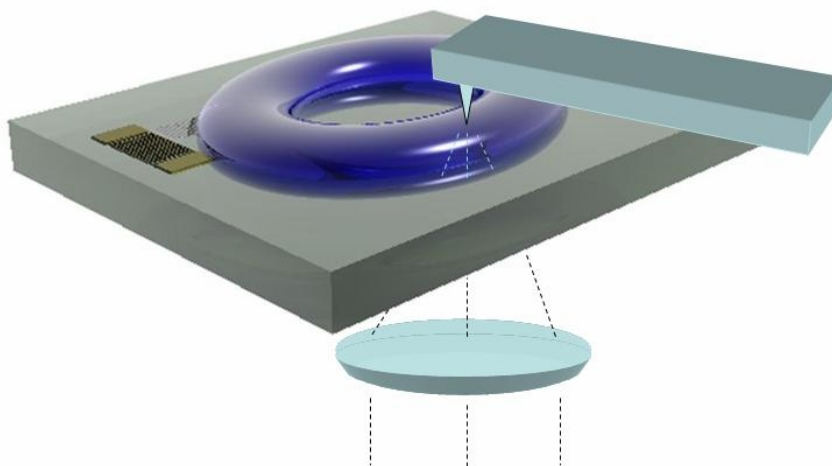


Figure 4.6: The microfluidic set up. The unique combination of a microscope, an AFM tip and a SAW driven pumping system enables both studying the formation of macromolecular VWF networks and conglomerates in life time and the mechanical manipulation of VWF aggregates and bundle pulling in particular.

sample or tip, the equilibration process and therefore the reaction of the system is diffusion limited. Our microfluidic reactor can induce an immediate response due to its pronounced mixing properties [76, 77] and prevent aging of biological samples as a result of extended waiting times. Furthermore, without the necessity to move the sample at any time, the probability of contamination is dramatically reduced while the ROI is maintained to the limit of normal cantilever drift.

5 Results and Discussion

In the course of wound healing, VWF molecules bind to both injured endothelial cells and platelets, form networks and seal vessel lesions. This process is accompanied by a mechanically induced transition from a collapsed to an elongated VWF conformation, which seems to be the origin of the protein's unique properties (see also sections 3.1.3 and 3.1.4). From a physical point of view, most of the basic questions concerning the proper functioning of VWF in blood clotting are not understood at all: What is the origin of VWF's all-or-none activation behaviour? What kinds of forces stabilise the VWF molecule? What are the driving forces for network formation and self-association? How does VWF bind to and form networks on endothelial cells and platelets? In this section, these open questions will be thoroughly approached and the results will be connected to a comprehensive image of VWF's role in wound healing.

5.1 VWF-VWF-Interaction

Experiments using SAW driven microfluidics (chapter 4.2.1) have proven that arterial shear forces are able to induce VWF activation. Simulations further revealed that the monomer-monomer interaction potential within the globular VWF molecule defines the fingerprint of this structural transition. However, there is considerable uncertainty concerning the type of the effective interaction forces between monomers within the VWF globule as well as inside an extended VWF network. In the following chapters, a detailed picture of the influence of a surface or a geometrical obstacle on VWF activation and network formation will be elaborated and completed by the analysis of the interior dynamics of these VWF conglomerates. The investigation of the influence of the hydrophobic effect and pH changes on the protein solubility are integrated into a VWF phase diagram displaying the protein's activity under physiologic and pathological conditions.

5.1.1 Formation of Ultralarge VWF Aggregates

Schneider et al. demonstrated that shear stress of about $5000s^{-1}$ is capable to induce the elongation of fluorescently labelled VWF molecules in the absence of any surface [1]. Nevertheless, the surface itself, for example at a site of vascular damage, may significantly affect the activation process of VWF. It may modify the streaming properties and the forces on single molecules compared to the intact blood vessel. In the following section, the influence of the surface on VWF elongation and network formation will be investigated by manipulating the stream lines in our newly developed Lab on a Chip - AFM - hybrid system (see also chapter 4.2).

Results

In a first set of experiments, $30\mu\text{l}$ droplets with a VWF concentration of $c \approx 10 \frac{\mu\text{g}}{\text{ml}}$ diluted in PBS++ buffer were placed on a Surface Acoustic Wave (SAW) reaction chamber (figure 5.1). Herein, c is chosen to match human blood concentration. To avoid evaporation during the application of shear stress for 10min , the sample was covered with a beaker. The size distribution of the resulting networks and conglomerates was analysed as a function of shear flow using a cell counting grid and optical microscopy. Due to the large size of the resulting ULVWF fibres and networks we were able to observe the protein structures in an inverted microscope without additional labelling.

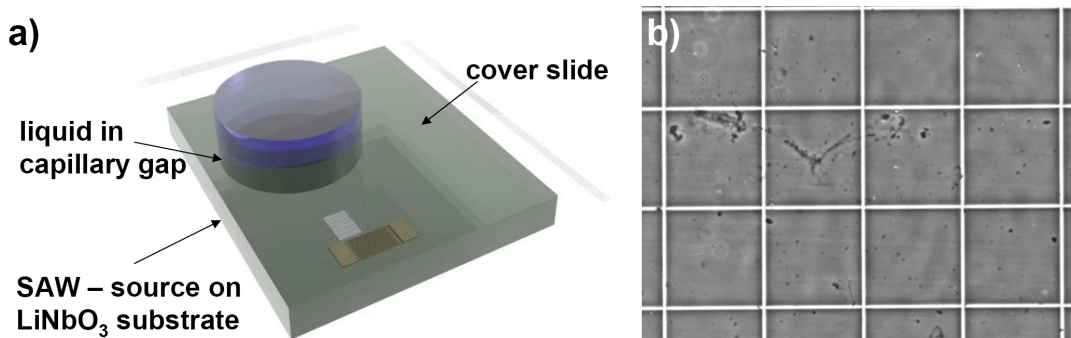


Figure 5.1: a) A droplet of VWF buffer solution was added on a cover slide. The Surface Acoustic Wave (SAW) was coupled into the droplet and induced fluid flow. b) After the application of shear flow, a cell counting grid was placed onto the droplet and VWF networks and conglomerates were quantified. The image shows an extended V-shaped network and a multitude of smaller aggregates. The side length of the squares is $50\mu\text{m}$.

A significant increase of ultralarge networks (ULVWF) ($> 25\mu\text{m}$) was found to occur at shear rates above $\dot{\gamma}_{crit} > 2000\text{s}^{-1} \pm 500\text{s}^{-1}$. This experimental error arises from the difficult determination of the shear rates. The stream lines within a small droplet exhibit a complex pattern with varying velocity gradients at different positions [76]. The highest wall shear rates, which were used for our estimations, are realized directly above the Interdigital Transducer (IDT) structure that creates the fluid flow. The effective shear rate decreases with increasing distance to this pumping source. As the network formation was examined on an extended area around the IDTs, the actual $\dot{\gamma}_{crit}$ for VWF activation should be found rather in the range of 1500s^{-1} than 2500s^{-1} . Therewith, a discrepancy of a factor of $\approx 2 - 3$ arises between the critical shear rates for VWF activation under bulk conditions and on glass substrates.

Clefts, constrictions and protruding parts of cells and extracellular matrix at a site of vascular injury create additional accessible surface for VWF molecules compared to an intact vessel. Furthermore, the local streaming pattern of the blood is considerably affected. The disturbance of the stream lines itself may directly influence VWF adhesion.

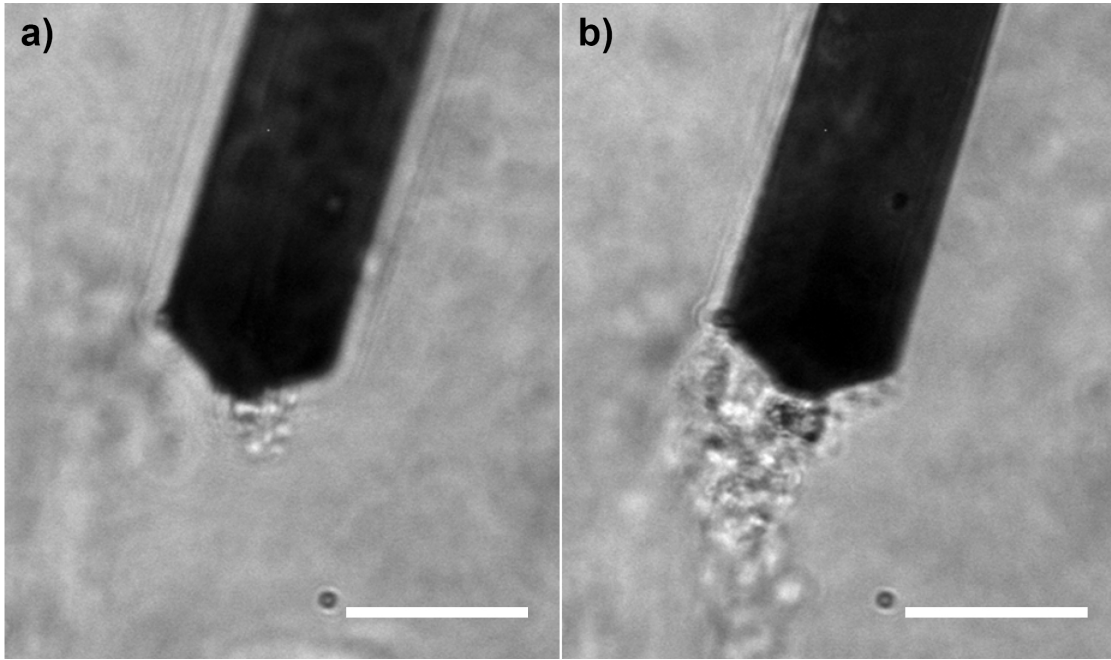


Figure 5.2: VWF adhesion on the cantilever tip at shear rates of about a) $800s^{-1}$ and b) $1300s^{-1}$ exhibits a pronounced quantitative difference after $1min$ ($c_{VWF} = 10\frac{\mu g}{ml}$). (Scale bar $\approx 40\mu m$)

By placing an AFM cantilever into our lab on a chip - AFM hybrid system, precise manipulation of the stream lines mimicking the flow conditions at a damaged vessel wall became possible. The AFM cantilever was solely used as an anchoring point for VWF adhesion and not to quantify interaction forces of any kind. According to the position of the cantilever in the droplet and the applied power to the IDT pumping system, various streaming conditions can be realized. For the analysis of VWF adhesion, a position featuring almost parallel stream lines to the cantilever direction was chosen. VWF agglomeration was monitored as a function of shear rate around the cantilever tip (figure 5.2). At a critical shear rate $\dot{\gamma}_{crit} \approx 1300s^{-1} \pm 100s^{-1}$ VWF binding significantly increased. The shear rates were calculated by analysing the flow velocity of beads as a function of their distance to the AFM tip. To achieve the actual flow profile, a series of images of a high speed camera was superimposed revealing the stream lines as a function of applied power on the IDTs (figure 5.3).

Furthermore, changing the flow velocity modified the stream lines around the AFM tip (figure 5.3). With increasing velocity and shear rate, a depletion zone featuring low residence probability of beads occurred behind the cantilever. Beads which were infrequently found in this depletion zone, exhibit small and sometimes negative velocities compared to the surrounding stream.

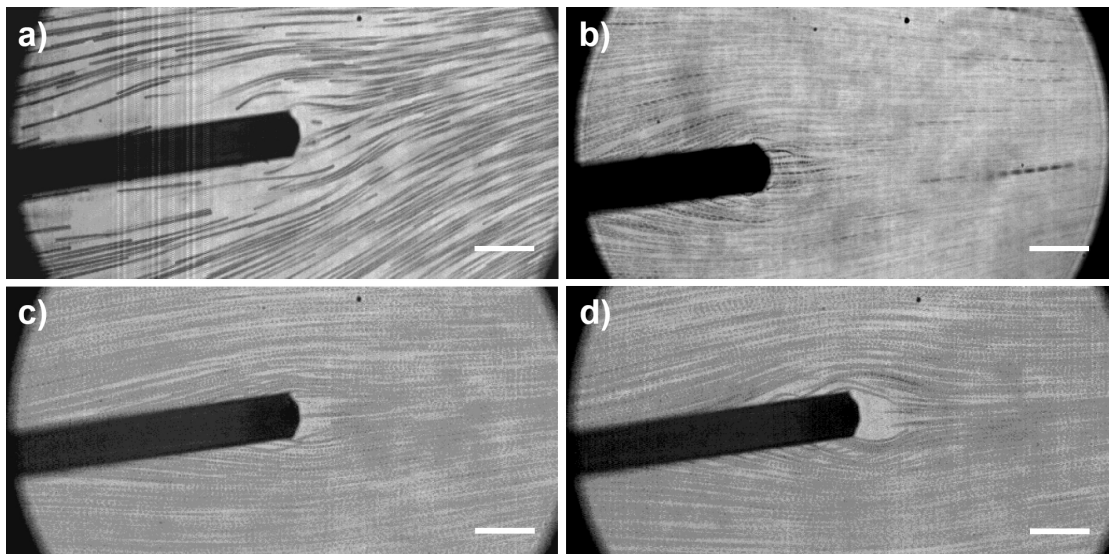


Figure 5.3: The visualization of the stream lines is achieved by superimposing a series of successive images of moving beads around the cantilever. The shear rate in close vicinity to the cantilever was calculated to be a) $130s^{-1}$, b) $750s^{-1}$, c) $1300s^{-1}$ and d) $2000s^{-1}$. For higher shear rates, a depletion area behind the cantilever emerged. (Scale bar $\approx 40\mu m$)

Discussion

Apart from the use of unstained VWF without any chemical or physical modifications, the analysis of the VWF network formation process in a flow chamber represents a clear advantage over single molecule measurements [1] as it provides the possibility to investigate an average effect caused by numerous single activation events. In order to mimic the streaming conditions at damaged endothelial cells, surfaces and protrusions into the fluid flow were introduced into the analysis. Here, a significant decrease of the critical shear rate by more than 50% was found in comparison to bulk measurements.

An explanation for the effect of a wall on VWF activation is given in a theoretical work of Alexander-Katz in 2007 [78]. There, he extended the hydrodynamic simulations on VWF activation summarized in chapter 3.1.4 from 3D bulk conditions to those in vicinity of a planar wall. The collapsed polymer is then modelled by a chain of interconnected monomers which experience Lennard-Jones interaction [2]. Similar to the simulations in the bulk, the polymer at a fixed position near a solid surface undergoes strong size fluctuations at a critical shear rate $\dot{\gamma}_{crit}$. Keeping this critical wall shear rate constant while removing the globule from the surface completely abolishes the fluctuations and stretching of the polymer. In other words, the influence of the wall reduces the critical shear rate for VWF activation. The reason for this behaviour is found in the cooperative movement between the polymer and adjacent layers of fluid. At constant, but under-critical shear rate, the globule simply rotates in the x -direction. Solvent molecules in close vicinity to the globule are coupled to this rotation by drag forces (figure 5.4). The

reduction of the distance of the globule to a solid wall while keeping the shear rate constant distorts the coupled movement at the lower part of the polymer and its solvent layer. Close to the wall, both rotation and translation of the globule are slowed down. As the shear rate of the surrounding flow is kept constant, the net forces on the globule increase resulting in an enhanced activation probability near the surface.

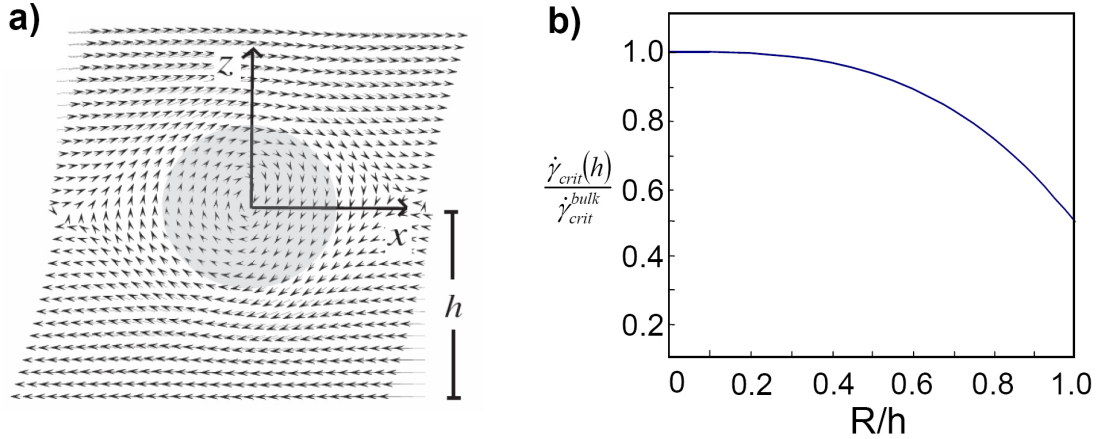


Figure 5.4: The globule (grey circle) rotates in a constant shear field with increasing flow velocity $v(x)$ in z -direction. The arrows denote the direction and velocity of every particle in a co-moving coordinate frame. Around the globule, drag forces induce adjacent solvent molecules to participate in the rotation and hence alter the stream lines compared to the pure flow field. b) According to equation 5.1 the critical shear rate decreases when approaching the surface. This effect is only pronounced in close vicinity to the solid wall (figures taken from Reference [78]).

The critical shear rate $\dot{\gamma}_{crit}(h)$ of the polymer with radius R as a function of distance h from the surface is ($\dot{\gamma}_{crit}^{bulk}$: critical shear rate of the polymer in the absence of any surface) [78]:

$$\dot{\gamma}_{crit}(h) = \left[1 - c_{\gamma} \cdot \left(\frac{R}{h} \right)^3 \right] \cdot \dot{\gamma}_{crit}^{bulk} \quad (5.1)$$

For a polymer consisting of 80 to 120 monomeric subunits, which is an accurate description of large VWF multimers, the size dependent coefficient c_{γ} is approximately 0.5. A distinguishable effect is limited to distances close to the wall (figure 5.4 b). Already for distances of twice the globule radius $h = 2R$, the critical shear rate of the globule almost corresponds to the one in the bulk.

Mimicking the disturbance of the flow profile at a site of vascular injury, the introduction of an AFM tip into the artificial blood stream served as a contact point for VWF adhesion. A critical shear rate of approximately $1300s^{-1} \pm 100s^{-1}$ was found to induce VWF conglomeration at the AFM tip. This is in close vicinity to the lower range of the critical shear rate for VWF activation on a plane surface. The small deviation in

the actual shear rates between these two measurements may be a result of an error in the estimation of the actual shear rates. On the other hand, there may be an additional mechanism. In this sense, an interesting aspect is the emergence of a depletion zone behind the cantilever exactly at a shear rate of $1300s^{-1}$, which became even more pronounced at higher fluid velocities. Compared to the surrounding medium, only few beads with small velocities and sometimes opposite flow direction were found in this zone. Due to drag forces as a consequence of a high velocity gradient between the depletion zone and the adjacent medium, the development of vortices in the depletion zone seems reasonable (figure 5.5) [79]. The lack of beads right behind the cantilever goes along with this assumption. Similar to a centrifuge, a vortex accumulates particles when the ratio $\frac{\rho_P}{\rho_M}$ between the density of the particles ρ_P and the medium ρ_M is smaller than one and expels them when $\rho_P > \rho_M$ as it is in the case of both beads and VWF. Nevertheless, dense particles can be accumulated in areas of diminished fluid motion between vortices and surface [80]. Due to its extended three dimensional design, the vortex geometry may be not limited to the plane of the cantilever arm. Although it perfectly accounts for the observed VWF accumulation, a more precise analysis including elaborate three dimensional flow monitoring is necessary to proof or disproof such a model.

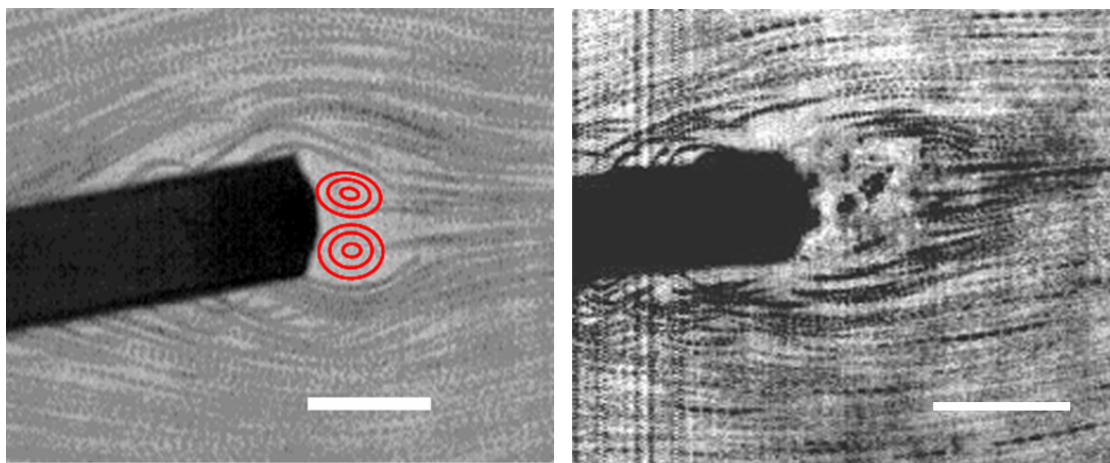


Figure 5.5: a) Vortices may arise and form the depletion zone above a threshold fluid velocity. The vortex pattern won't be limited to a two dimensional structure as indicated by the sketch, but also form around the cantilever tip. b) The depletion zone disappears as a meshwork of VWF molecules attaches on the edge of the cantilever. This directly influences the streaming pattern. (Scale bar $\approx 40\mu m$)

As more and more VWF proteins adhere to the cantilever, the protein conglomerate grows into and finally eliminates the depletion zone (figure 5.5 b). The actual binding mechanism of VWF to the cantilever may involve only shear induced polymer activation. Nevertheless, particle accumulation as a result of stream line manipulation or a combination of both accumulation and shear induced activations seems possible.

The presented findings have outstanding biological impact: Whereas a shear rate of $5000s^{-1}$ is necessary to unroll VWF under bulk conditions, the presence of a rough surface comprising obstacles to the surrounding flow decreases the critical shear rates roughly by a factor of 3. The reduction of the $\dot{\gamma}_{crit}$ close to vessel walls is a crucial evolutionary adjustment of nature to avoid dangerous platelet binding accompanied by thrombus formation in the vessel interior. It assures that blood clot formation is restricted to regions close to the damaged vessel surface. Our hybrid system with a cantilever protruding into the fluid flow proved to be perfectly suited to mimic the flow conditions at injured vessel walls. Parts of destructed endothelial cells or exposed extracellular tissue in the blood stream may be able to change the local streaming pattern in a way that results in an accumulation of VWF and further enhances its binding potential to sites of injury.

These investigations introduced stream line tuning and enhanced effective shear flow in the vicinity of surfaces and spatial restrictions at sites of vascular damage into the concept of blood clotting and will specify existing concepts of VWF adhesion.

5.1.2 Relaxation of Ultralarge VWF Bundles

One of the key features of the dynamics of (bio-)polymer systems is its relaxation spectrum, since it contains the relevant time scales for the polymer to reach its equilibrium configuration from an imposed non-equilibrium state [81]. By using the appropriate model, one can in principle extract the relaxation time τ and relate it to internal chain dynamics being controlled through the monomer-monomer interactions. Therefore, the investigating of the relaxation dynamics as a function of the different variables represents an important step towards a deeper understanding of the mechanical properties of ultralarge VWF (ULVWF) bundles. Moreover, it provides the basis to test theoretical models describing the relaxation of these assemblies. Using our hybrid setup, the formation of ULVWF networks could be induced and the relaxation of bundles of different lengths pulled from VWF networks by an AFM cantilever tip was investigated.

Results

In the course of an experiment, the AFM cantilever tip is approached to a protein network which was created by shear flow induced VWF conglomeration beforehand. The attached VWF bundles are then gently pulled by the AFM tip until they finally rupture. Due to the planar and optical transparent hybrid system, both the AFM tip and the bundle relaxation could be recorded simultaneously with an inverted microscope. Acquired data of the time course of the relaxation process were analysed using standard imaging software. In figure 5.6 a), a ULVWF bundle was immobilized onto the AFM tip and exposed to mechanical stress. The protein binding to the AFM tip is achieved without any surface functionalization. To have a strong grip on the bundle, the tip was allowed to equilibrate for several minutes just in contact with the protein assembly. A thick multi-fibre bundle was then formed by gently retracting the AFM tip. Only bundles of similar thickness ($< 1\mu m$) were analysed.

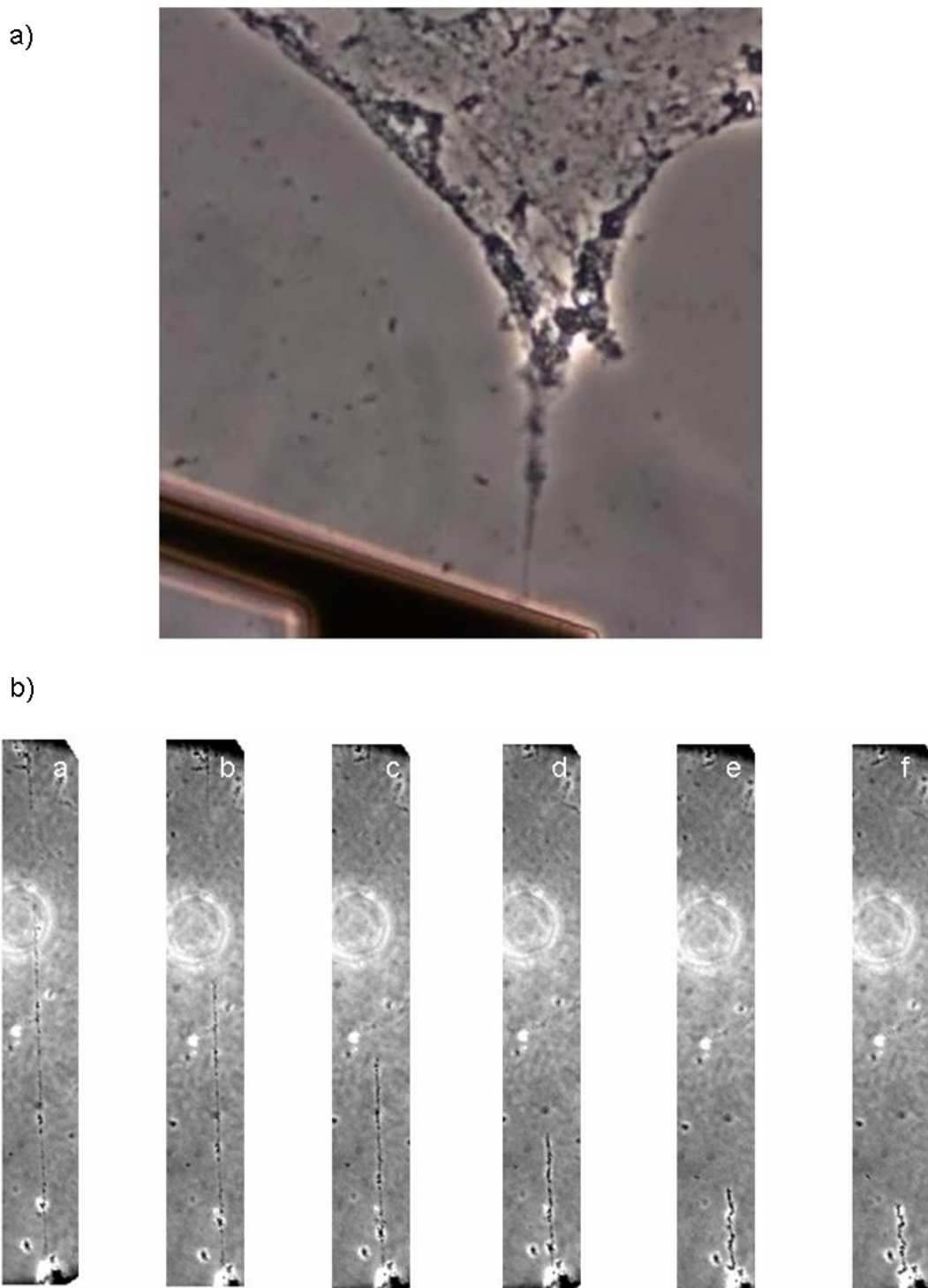


Figure 5.6: a) A bundle was immobilized on AFM tip and pulled out a ULVWF network. b) The time course of the bundle relaxation after rupture was monitored by optical microscopy (each image of the sequence is approximately $840\mu\text{m}$ in height and $120\mu\text{m}$ in width).

The relaxation of the bundle, governed by strong attractive interactions and entropic penalties associated with the stretched conformation was followed after it ruptured from the ULVWF assembly (figure 5.6 b). From the sequence shown in the figure, it is important to note that the filament remains fairly straight during the contraction process. The stretching and retraction proceeded by an inhomogeneous coarsening of the bundle in the apparent form of pearls.

On a more quantitative basis, the dynamics of the system were monitored by measuring the end-to-end length of the bundle as a function of time. The maximum length L_0 was determined by the distance between the AFM tip and the point where rupture occurred. A typical trace of the end-to-end distance (i.e. the distance from the AFM tip to the free end of the ULVWF) as a function of time is presented in figure 5.7 a). The relaxation has two characteristic time scales (see inset), and both of these periods are well described by stretched exponentials of the form: $L \propto e^{-(\frac{t}{\tau})^\beta}$ with $\beta \approx 0.5$. This is corroborated by observing the nice fit to the data over the full range using a sum of two extended exponentials denoted by the continuous curve.

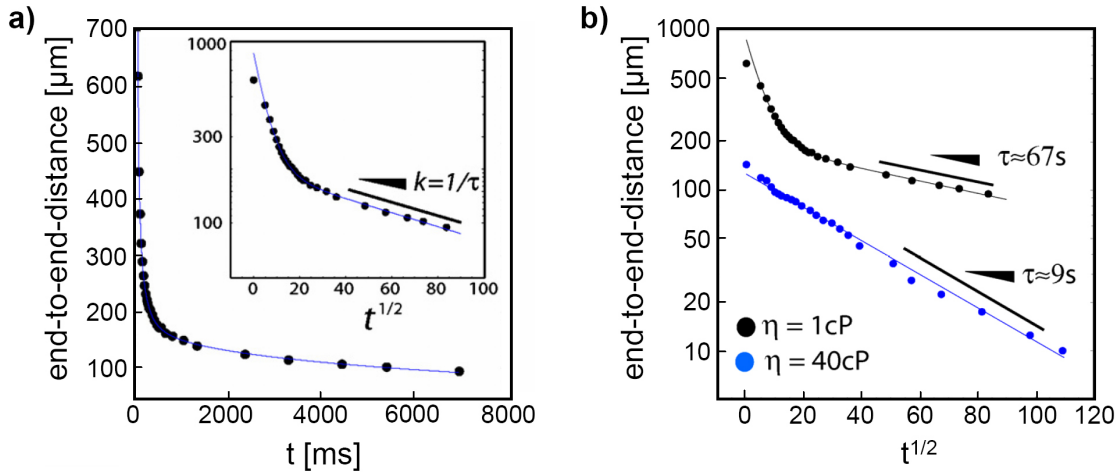


Figure 5.7: a) The end-to-end distance is plotted as a function of time. In the inset, the same data plotted in a log-linear scale, and the x -axis is taken to be $t^{1/2}$. The continuous line is a fit to the data using: $L_1 \cdot \exp(-\frac{t}{s_1})^{0.5} + L_2 \cdot \exp(-\frac{t}{s_2})^{0.5}$, where $L_1 = 676 \mu\text{m}$, $L_2 = 194 \mu\text{m}$, $s_1 = 156 \text{ms}$, $s_2 = 156 \text{ms}$. b) The end-to-end distance as a function of $t^{1/2}$ is plotted in a log-linear scale for different viscosities. The upper (black) curve corresponds to a viscosity of 1cP , and the lower (blue) curve corresponds to a viscosity of 40cP .

The fact that the relaxation process follows a stretched exponential implies that the underlying dynamics is governed by hopping events between random minima in a rough energy landscape. Equivalently, the relaxation spectrum is composed of a broad (random) distribution of exponential processes [82]. Such relaxation behaviour is common in nature, and has been found in different contexts. In particular, it has been observed

in the relaxation of DNA [83] and in proteins [84]. In these studies, the origin of the relaxation spectrum arises from the averaging over a multitude of parallel non-interacting (presumably exponential) relaxation processes. In the context of single polymer relaxation, Cherayil et al. have shown [85] that after inclusion of memory effects to the dynamics of the system, the relaxation is a stretched exponential with a exponent of $\beta \approx 0.5$. The memory effects included in this work accounted for the fact that a given conformation at earlier times affects the distribution of conformations at a later time along the relaxation process.

VWF bundle relaxation presents new features compared to those described previously: i) it has two clear relaxation time scales, and ii) the relaxation of the individual molecules is coupled to the one of all others in a non-trivial fashion. In this sense, VWF bundle relaxation is a more complex problem than those studied before. One of the striking features of this finding is that the longest relaxation rate k , corresponding to the inverse of the longest relaxation time τ , seems not to be dependent of the initial length of the bundle. This implies that the dynamics of relaxation is dominated by conformational constraints, as well as effective internal friction limiting the rate of deformation of the object itself.

To further unravel the physical origin of the observed phenomenon, the effect of viscosity of the solvent on the long and short timescales of the bundle relaxation was studied by adding glycerol as a thickening agent. In figure 5.7 b, two different traces of the end-to-end distance at different viscosities (1cP and 40cP) are shown. In the high viscosity system, the initial temporal decay is slowed down in a way that the full relaxation can be well described by a single stretched exponential. Interestingly, the slowest relaxation rate is now faster than the one for pure buffer solution with lower viscosity.

Discussion

The relaxation of the bundles does not follow a simply exponential law, but rather is well described by stretched exponentials with an exponent $\beta = 0.5$ throughout all relaxation experiments. In the low viscosity case (essentially that of water), two characteristic decay rates are found. On the other hand, only a single relaxation time is observed in a high viscous environment. However, the relaxation spectrum found here is still different from the one of a single collapsing polymer. There, the relaxation of the end-to-end distance is supra-exponential, comprising a growing rate of compactification as the polymer relaxes [86]. If at all, there's only evidence of such a relaxation type during the first few 100ms after rupture. This observation is not too surprising, as the ULVWF consists of many single fibres of different lengths relaxing at the same time in a complex fashion. Comparing it to the dynamics of a single polymer seems to be at least to be doubted. The complexity of the system arises because the relaxation of one fibre affects the relaxation of the other fibres, and vice versa. For a better feeling of why the observed relaxation is a stretched exponential, it is probably better to describe the bundle as a single entity relaxing in a rough potential landscape determined by the configurations of the VWF single fibre constituents. The manifold of configurations is presumably strongly dependent on the number of self-association contacts, and hopping from one state to

the other can only be done through thermally activated processes. The average barrier height will be reduced in the highly stretched state because of entropic forces, and thus the rate of relaxation should be faster at the beginning. Nonetheless, this argument would imply that one would see a continuous change in the relaxation of the bundle, and not two clear relaxation times as it is found here. An alternative explanation is that there are two attractive interactions of different origins, which in this case would presumably correspond to self-association and hydrophobic attraction among monomers, driving the relaxation in each of these two regimes. So far, it is still unclear which of these interactions is the dominant one in the collapse of VWF, but we might argue that at long times, the hydrophobic interactions must become important since in principle the majority of the possible self-association contacts within the bundle should be present and only unfavourable surface interactions with the solvent and entropy can drive the further decrease in size. Nevertheless, hydrogen bonding might also play a crucial role and a complete description should include the three different interactions. The entropic contribution, on the other hand, is presumably negligible at the latter stages, since the thickness of the bundle (as measured with optical microscopy) is about $10\mu m$, a value that exceeds that of an individual molecule of a VWF ($\approx 5\mu m$, assuming that a single fibre is $100\mu m$ long and obeys random walk statistics). Nevertheless, one should be careful since entropy might still play a role if the polymers remain stretched within the bundle due to strong constraints on its mobility, a fact that can be indirectly assumed by seeing the snapshots of the relaxation where the filament remained rather straight (figure 5.6 b).

From another perspective, the fast relaxation at short times may lead to jamming or highly constrained dynamics (corresponding to deep metastable minima) because it does not have enough time to sample the local energy landscape. If one decelerates the initial relaxation by using a highly viscous solvent, the system will be closer to equilibrium as it relaxes and will not longer get trapped in deep minima. In fact, the longest relaxation time should be shorter for this system. This is perfectly illustrated in figure 5.7, where the rate of compactification at long times is larger for the bundle in the higher viscosity medium, while the initial relaxation is strongly slowed down. The reorganization within the bundle at the initial stages of relaxation leads to faster relaxation at long times.

5.1.3 Impact of the Hydrophobic Effect on VWF Network Formation

The origin of VWF's stretching behaviour can be traced back to attractive interactions ΔU among VWF monomers that maintain the multimer in a compact globular conformation [1, 2, 78]. Clearly, a modest reduction in ΔU will result in a significant decrease of the critical shear rate according to $\dot{\gamma}_{crit} \propto (\Delta U)^2$. Any solvent which decreases ΔU will increase the amount of stretched VWF fibres and make self aggregation and network formation more likely. In addition, the relaxation behaviour of ULVWF bundles elucidated strong interactions of single elongated fibres within an extended network. These necessarily include monomer-monomer interactions between different fibres which should obey the same potential ΔU . The investigation of the effect of hydrophobic forces on the interaction potential ΔU and hence VWF multimerization and self-association will

be the subject of this section.

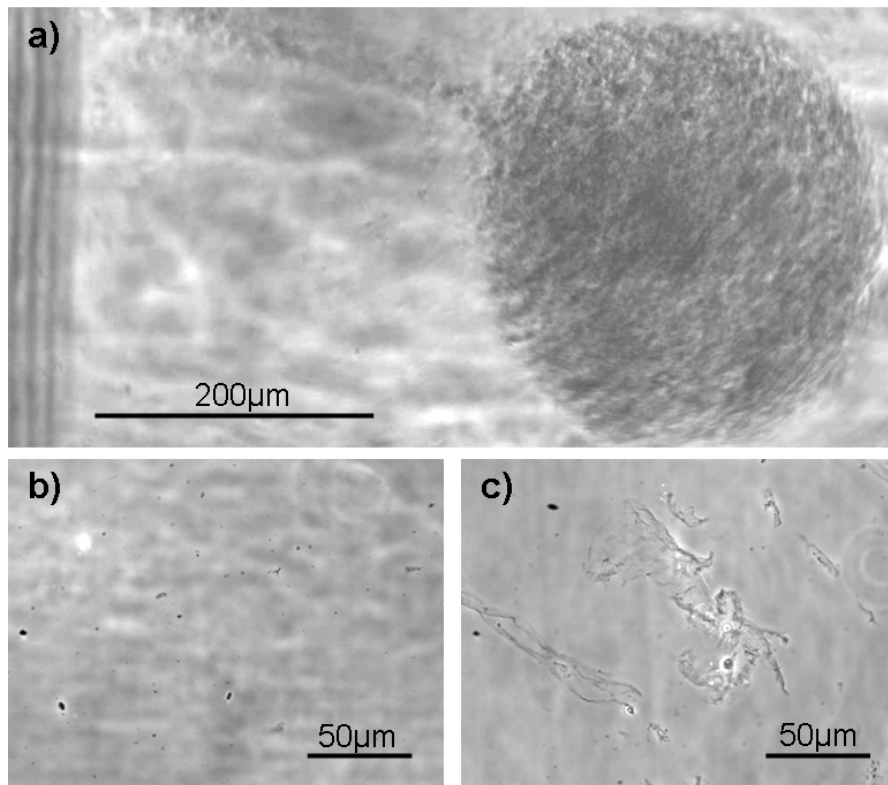


Figure 5.8: a) Gentle agitation led to the formation of macroscopic three dimensional VWF conglomerates in a highly concentrated VWF buffer solution ($c_{VWF} \approx 500 \frac{\mu g}{ml}$) in the presence of $100mM$ ammonium sulphate. b) For a VWF concentration of $c_{VWF} \approx 10 \frac{\mu g}{ml}$, a wall shear rate of approximately $1000s^{-1}$ was not sufficient to unroll the polymer after the addition of $100mM$ ammonium sulphate. c) Keeping the shear rate constant while increasing the Ammonium sulphate concentration to $1M$, excessive network formation occurred.

Results

The influence of the hydrophobic effect on the monomer-monomer interaction was investigated in our SAW driven microfluidic reaction chamber in two different ways. In a first set of experiments, the solvent's polarity was decreased by the addition of ethanol. Moreover, the influence of the antichaotropic agent ammonium sulphate, which is known to enhance protein stability by increasing the hydrophobic effect, on VWF activation is tested. If the hydrophobic effect has a dominant influence on the interaction potential ΔU , a distinct decrease of the critical shear rate $\dot{\gamma}_{crit}$ should be found in the first case. On the other hand, ammonium sulphate should strengthen the monomer-monomer interaction and increase ΔU [87, 88]. The course of an experiment follows chapter 5.1.1.

In perfect accordance with theory, the critical shear rate for network formation decreased from approximately $\dot{\gamma}_{crit} \approx 2000s^{-1}$ under hydrophilic buffer conditions to approximately $\dot{\gamma}_{crit} \approx 1000s^{-1}$ in the ethanol (50/50vol/vol) containing solution [89, 90]. No difference in the appearance of the networks and conglomerates between the pure buffer system and the ethanol/buffer mixture could be monitored by optical microscopy.

In a next experiment, the antichaotropic (kosmotropic) salt ammonium sulphate was added to the buffer solution at concentrations of 100mM, 500mM and 1M. In order to test for the salting out potential of the kosmotrope in first place [91, 92], a highly concentrated VWF solution ($c \approx 500 \frac{\mu g}{ml}$) was subjected to 100mM ammonium sulphate. Gentle SAW induced agitation produced macroscopic three dimensional protein conglomerates in the mm range (figure 5.8). The assembly process was completed within a few seconds after the addition of ammonium sulphate. A rough size estimation yields that the conglomerate displayed in figure 5.8 a) contains a large proportion of VWF molecules from solution. Reducing the amount of VWF to a physiologic concentration ($\approx 10 \frac{\mu g}{ml}$) and adding 100mM of the kosmotrope resulted in numerous small instead of one macroscopic aggregate (figure 5.8 b). The addition of 500mM and 1M ammonium sulphate displayed the same tendency.

Furthermore, shear stress was applied to VWF buffer solutions ($c_{VWF} \approx 10 \frac{\mu g}{ml}$) containing various concentrations of ammonium sulphate. Iso-shear experiments at approximately $1000s^{-1}$ exhibited no or only minimal network formation for 100 and 500mM of the kosmotrope whereas this shear rate was sufficient to induce excessive network formation at 1M ammonium sulphate (figure 5.8 c).

Discussion

A crucial parameter for protein stability on a molecular level between single amino acids as well as for the collapse of multimeric biopolymers like VWF is the hydrophobic effect [87]. In hydrophilic water environment, proteins tend to minimize their energy by burying hydrophobic residues within the molecule whereas hydrophilic parts are exposed on the outside. Therefore, any process which strengthens the hydrophobic effect should also increase the protein's stability against denaturation. While monitoring the dynamics of ULVWF aggregate formation in the microfluidic reaction chamber, hydrophobic interactions are introduced as an important parameter for fine-tuning and regulating the critical mechanical forces of VWF activation. On closer examination, the results presented above seem counterintuitive. The critical shear rate is reduced for both a decrease of the hydrophobicity due to ethanol and an increase of the hydrophobicity due to the antichaotropic salt.

In a medium containing 50vol% ethanol, enhanced network formation was monitored at a critical shear rate of $\dot{\gamma}_{crit} \approx 1000s^{-1}$ compared to $\approx 2000s^{-1}$ under pure buffer conditions. Ethanol decreases the hydrophilic properties of water media going along with a solubility change of proteins in solution. In the case of VWF, a decrease in protein stability and critical shear rate can be directly referred to an enhanced solubility of its constituting monomers in a more hydrophobic environment [93]. Herein, the stabilizing effect of the monomer-monomer interaction potential ΔU , which supports the collapsed

VWF conformation, is weakened. This is in perfect agreement with the assumption of a considerable influence of hydrophobic interactions in VWF activation.

On the other hand, the origin of the effect of ammonium sulphate on an enhanced network and aggregate formation remains open, so far. Independent of the applied shear stress, there was a distinct "salting out" effect upon the addition of ammonium sulphate. Salting out is found to increase with increasing concentration of the antichaotropic agent resulting in enhanced conglomerate sizes [94]. At high VWF concentrations, the formation of macroscopic three dimensional protein conglomerates up to the *mm* range was observed. A preceding conformational change within the VWF molecules for this conglomeration in the sense of mechanical unrolling can be ruled out. For physiological concentrations of VWF, ammonium sulphate produced a multitude of small aggregates. Although not totally understood yet, salting out is thought to be driven by a change in the surface tension at the polymer-water interface associated with an enhanced cost of protein hydration [44, 95]. Exerting mechanical forces via an AFM tip on such conglomerates resulted in the formation of ULVWF bundles similar to the bundle in figure 5.6. This finding has a considerable consequence: Functional VWF bundles or even networks can evolve from VWF conglomerates, which preformed without a conformational transition of its constituting single molecules. Nevertheless, the critical shear rate for VWF activation and network formation should increase as a result of enhanced hydrophobic interaction rather than decrease as it was found for high ammonium sulphate concentrations. Further experiments approaching directly the molecular impact of antichaotropic agents on the protein structure itself may be able to solve this dilemma.

Whatever the actual origin of the action of ammonium sulphate may be, hydrophobic interactions have a major influence on VWF-VWF interaction. A weakening of the hydrophilic properties of the buffer media upon ethanol addition led to enhanced aggregation of VWF polymers into ULVWF conglomerates. Although structural changes within the VWF molecule can not be completely ruled out, the network formation process still requires a critical shear rate and seems to follow the same mechanism as it does under normal buffer conditions. In an ethanol enriched buffer system, single VWF molecules unroll due to hydrodynamic stress and decreased monomer-monomer interaction and form extended networks in their activated elongated conformation. In an environment containing ammonium sulphate, salting out effects induce the formation of large VWF aggregates. Exposed to mechanical forces, these aggregates can still be transformed into physiologically active networks.

5.1.4 Regulation of VWF Activation by Physiologic pH Changes

While the large sub-unit of VWF polymers has been identified as the molecular origin for the globule-stretch transition at arterial shear conditions, small variations in ΔU can be used to fine-tune the mechanical response of VWF. After the investigation of hydrophobic forces provided first insight into the physical character of the monomer-monomer interaction, the role of electrostatics and protonation effects on ΔU is approached in the following section. A way to control the electrostatic charge of proteins and amino acids is the protonation or deprotonation of accessible side chains by an adjustment of the *pH*

of the external solution. Within our blood stream, the pH value is regulated very precisely between 7.35 and 7.40. Deviations from that value represent pathophysiological conditions rather than natural pH -fluctuations. The findings presented here include the dependence of VWF stability on pH changes and divalent ion concentration and are of outstanding interest for biology and medicine at sites of pathologically altered tissue.

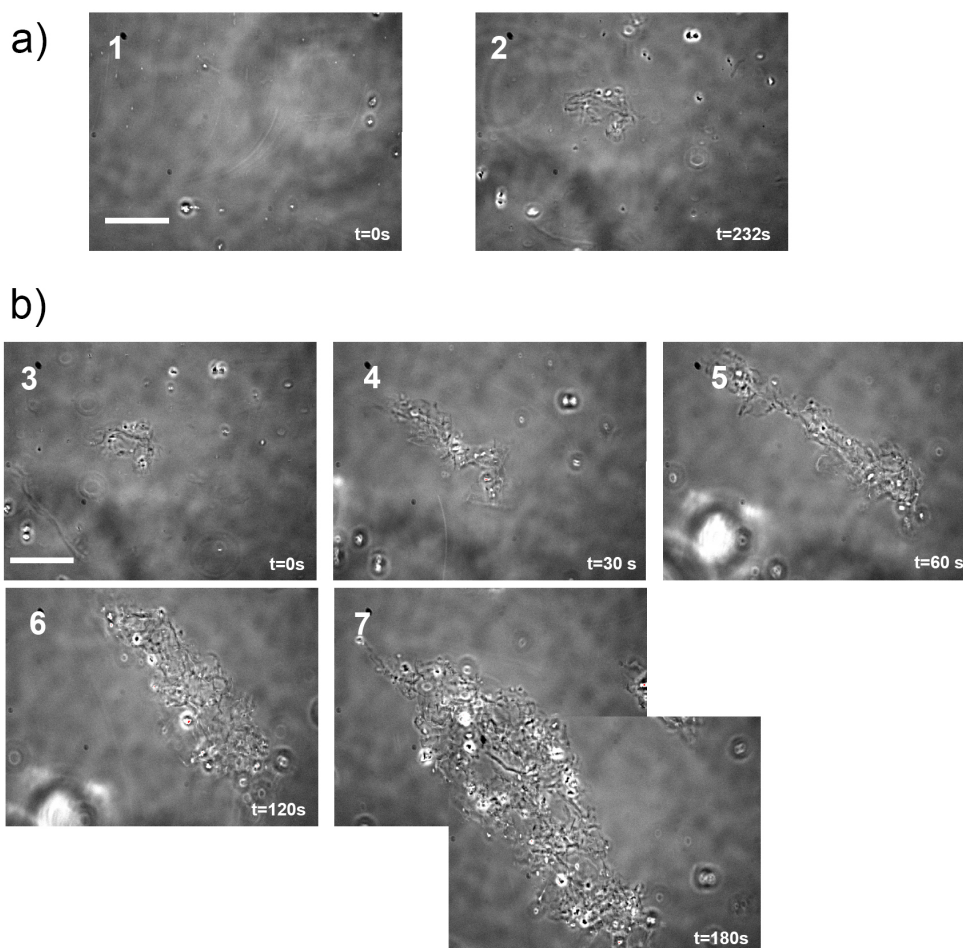


Figure 5.9: a) Subjected to shear flow around $1000s^{-1}$ no, or only little tendency to form aggregates is found. Only after $\approx 4min$ of shear flow single individual aggregates can be found. The rate of growth of such aggregates is barely detectable. b) When adding HCl directly into the flow to induce a pH drop below $pH \approx 7$ the network starts to grow immediately and rapidly (image 3 - 7). (Scale bar $40\mu m$)

Results

In addition to our SAW driven microfluidic reaction chamber, a custom designed cone and plate shear force apparatus is exploited to visualize single molecule activation of

fluorescently labelled VWF molecules. The combination of these techniques enabled studying both the process of ULVWF network formation and single molecule activation with a sufficient number of individual fibres. In the optical accessible shear cell, $\dot{\gamma}_{crit}$ can be accurately detected by fluorescence microscopy as the degree of elongated VWF corresponds precisely to the amount of surface bound VWF [1].

First evidence of a strong dependence of the dynamics of shear-driven VWF assembly into ULVWF networks on pH is illustrated in figure 5.9. At physiological concentrations ($c \approx 20 \frac{\mu g}{ml}$) and a pH of 7.4, ULVWF-networks do not form under a shear rate of $1000s^{-1}$ over a period of several minutes (figure 5.9 a). However, adding a small amount of HCl while keeping the shear flow constant led to the immediate formation of extended networks. Details of the dynamics of the network formation were monitored and are shown in Figure 5.9 b). It is important to note that in our system the pH equilibration occurs almost instantaneously due to the presence of acoustic mixing [96, 73] rather than being diffusion limited. The haemostatic activity of these networks is a crucial parameter from a physiological and medical point of view. To test for the activity to immobilize platelets, ULVWF networks were prepared at a shear rate of $\approx 1000s^{-1}$ and $pH \approx 6.0$. When adding platelets under flow conditions, they became attached along these networks verifying that the proteins completely retain their functionality (figure 5.10). Analysis of

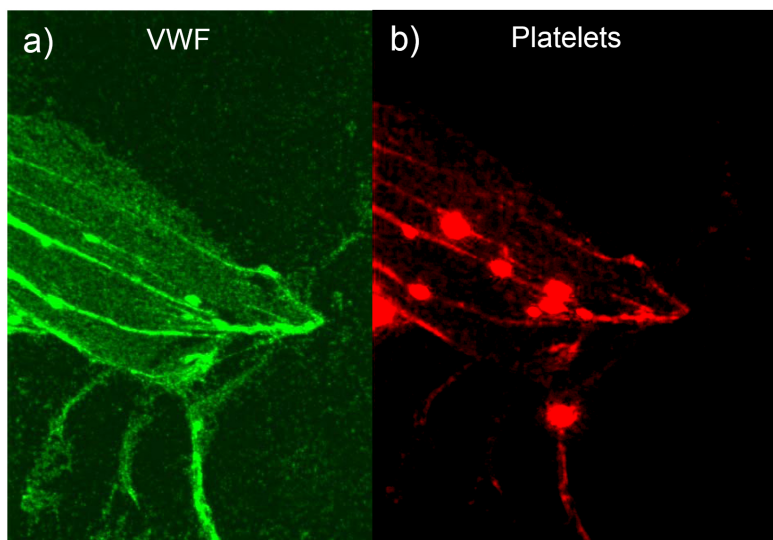


Figure 5.10: Shear rates above $1000s^{-1}$ cause extensive VWF networks at a $pH \approx 6.0$ (left). The tight adhesion of platelets (right) on VWF (left) demonstrates the haemostatic functionality (image size $\approx 140\mu m \times 100\mu m$). Both VWF and platelets were double-stained and were imaged by fluorescence microscopy.

the critical shear rate $\dot{\gamma}_{crit}(pH)$ necessary to trigger the globule-stretched transition as a function of pH in more detail reveals a clear maximum in both setups (figure 5.11). Using the more accurate cone and plate viscosimeter we find that this maximum occurs around $pH \approx 7.0$ when no calcium is present. Small deviations from this pH cause re-

solvable changes in $\dot{\gamma}_{crit}$. Therefore, VWF's potential to initiate blood clotting is clearly a function of both local shear stress as well as pH . At a first glance such a pronounced effect induced by a minute change in pH appears to be unfortunate for the protein's function. Natural fluctuations in pH would interfere with controlled activation at sides of elevated shear flow. However, the systemic pH of our circulatory system is precisely controlled and a departure from $pH \approx 7.4$ of ± 0.2 already represent pathophysiological conditions rather than natural pH -fluctuations.

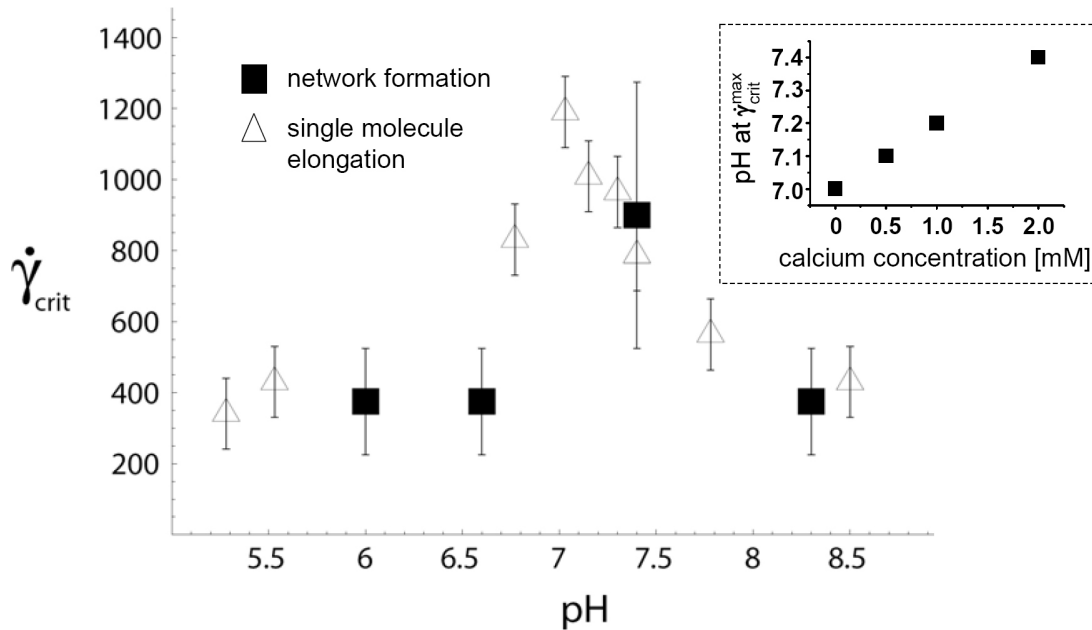


Figure 5.11: Single VWF molecules in PBS solution lacking divalent ions exhibit maximum stability against external shear stress at $pH \approx 7.0$. Inset: The pH at the maximum of the critical shear rate is strongly dependent of Ca^{2+} -concentration. An increase of the Ca^{2+} -concentration from 0 to a physiologic concentration of $c_{Ca^{2+}} \approx 2mM$ shifts VWF's maximum stability against hydrodynamic activation exactly to blood $pH \approx 7.4$.

However, these data were collected in a simple PBS buffer in the absence of divalent ions, which have a much higher binding constant to charged proteins than monovalent ions. To account for the effect of the most important divalent ions, the change in $\dot{\gamma}_{crit}^{max}$ at different Ca^{2+} concentrations was studied (figure 5.11 inset). A concentration of $1mM Ca^{2+}$ already shifts the maximum stability $\dot{\gamma}_{crit}^{max}$ from $pH \approx 7.0$ without Ca^{2+} to $pH \approx 7.2$. At $2mM Ca^{2+}$, the typical plasma level of divalent ions, $\dot{\gamma}_{crit}^{max}$ is found at physiological pH of 7.4. Therefore, divalent ions seem to be able to fine-tune the interaction potential ΔU between VWF monomers and to cause the maximum resistance against mechanical stretch-activation to take place at exactly physiological pH .

Discussion

What is the molecular origin of VWF's peculiar mechanical activation? The physical explanation for the conformational transition of the VWF multimers at the observed shear rates can be found in the sensitive scaling of $\dot{\gamma}_{crit}$ with the large subunit-size a (equation 3.6). A subunit of half the size would result in an increase in $\dot{\gamma}_{crit}$ to $\approx 30.000 - 50.000s^{-1}$ and would only in rare cases be of physiological relevance. However, keeping the size "genetically" fixed and varying the interaction potential ΔU between individual monomers assures the right order of magnitude for the stretching transition ($\approx 1000 - 10000s^{-1}$). This allows fine-tuning the critical shear rate $\dot{\gamma}_{crit}$ to the local physiological conditions. One way to manipulate the interaction potential ΔU between individual subunits is the protonation of the amino acid side group. The resulting net charge of the folded three dimensional polypeptide chain will affect its solubility in an aqueous environment. The relationship between solubility s and the molecules net-charge σ can be expressed as:

$$s \propto \sigma^2 \quad (5.2)$$

It can be related to the interaction potential ΔU between VWF monomers by assuming that the protein solubility decreases as the potential becomes more attractive:

$$s \propto \Delta U^{-1} = \frac{1}{\Delta U_0 - f^2 \cdot \frac{l_B}{a} \cdot e^{-\kappa \cdot a}} \quad (5.3)$$

Here, the first term in the denominator, ΔU_0 , represents the dispersion part (equation 3.6) and the second term the electrostatic contribution in the form of a Debye-Hückel equation for low potentials [36]. Further, l_B denotes the Bjerrum length, κ the Debye length, a the monomere size, and f the charge fraction per monomer. For small electrical contribution with respect to the dispersion part, equation 5.3 can be Taylor-expanded to arrive at

$$\Delta U^{-1} = \left(\frac{1}{\Delta U_0} \right)^2 \cdot \left(\Delta U_0 - f^2 \cdot \frac{l_B}{a} \cdot e^{-\kappa \cdot a} \right) \quad (5.4)$$

This expression is to leading order quadratic in the charge fraction f , implying $s \propto f^2$. Therefore, the monomer-monomer attraction is maximal while the solubility is minimal for zero net charge ($f \approx 0$). From a mechanical perspective, protein solubility is inversely related to its stability against side chain exposure, as it occurs during stretching. At its (effective) isoelectric point (pI_{eff}) the proteins net charge equals to zero demonstrating minimal solubility in the aqueous medium and a maximum in its stability against shear stress. It is important to note, that the effective isoelectric point must not be mistaken for the average over the individual pI s along the amino acid sequence. In contrast, it includes the complex cooperative effects of neighbouring residues forming a net potential along the protein-water interface. So far, no good theoretical models exist to predict effective isoelectric points pI_{eff} . Fulcher et al. determined the isoelectric point pI of urea treated (denatured) human VWF by isoelectric focussing and found it to be around

$pH \approx 5.7$ [97]. However, at this pH the protein is not in its native state, but resembles an unfolded coil of individual amino acids. On the other hand, the determination of the effective isoelectric point by simple pH titration experiments revealed clear indication for the existence of another pI_{eff} . This is shown in figure 5.12 where two plateaus, one at $pH > 8$ and another one around $pH \approx 6.5$ are present. The pH at half height between the onset of the two plateaus (8.1 and 6.7) corresponds to pI_{eff} and coincides with the physiological pH of 7.4. Further titration revealed a second drop at $pH \approx 5.5$ representing the isoelectric point of the unfolded state (data not shown). To confirm, the titration curve and to proof that VWF indeed exhibits charge neutrality around $pH \approx 7.4$ the effect of $NaCl$ on the globe-stretched transition was studied. While a charged protein should experience electrostatic screening of the charged side groups by monovalent ions, and thus would be less soluble in the presence of the salt, a protein at its pI_{eff} would be only weakly affected by monovalent ions. Varying the $NaCl$ concentration from $100mM$ to $1M$ without a detectable change in $\dot{\gamma}_{crit}$ gave strong evidence that the molecule is uncharged at $pH \approx 7.4$.

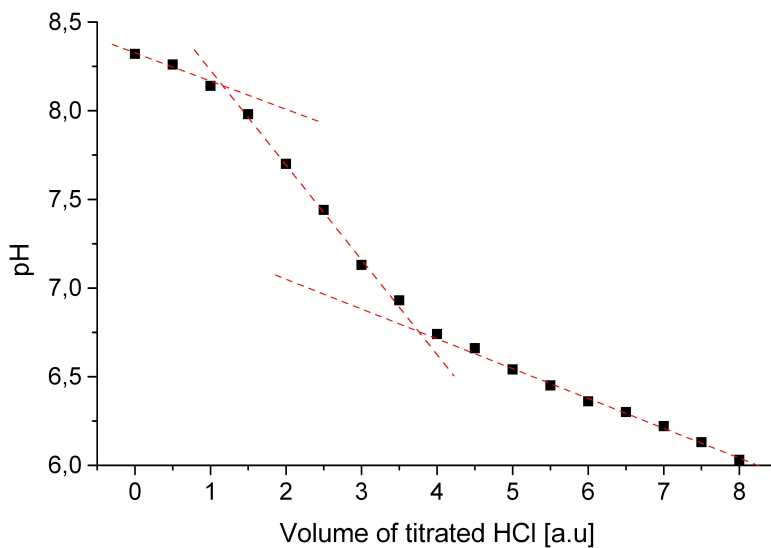


Figure 5.12: The pH titration curve of VWF in ion-free water features plateaus for pH values both > 8.1 and < 6.7 connected by a steep decline in between. The red lines are inserted for the evaluation of the effective isoelectric point pI_{eff} . pI_{eff} is derived as the mean value of the intersections of the red lines and happens to be exactly at $pH \approx 7.4$, typically for our blood.

In summary, the sequence of amino acids of the VWF molecule and its three dimensional arrangement seem to be optimally fitted to the physiological conditions of our blood. While geometrical factors like the length and monomer size had to be adopted to

match with typical mechanical stress conditions in our microvascular system [1, 2], side chains residues were arranged to result in an effective isoelectric point around $pH \approx 7.4$ providing maximum stability to VWF under physiological conditions. pH changes under pathophysiological conditions are therefore proposed to cause severe clotting issues. Local pH changes down to $pH \approx 6.0$ may occur in acidosis, ischaemia and under post-stenotic conditions. So far, medical data concerning the direct influence of pH on VWF activation and thrombus formation are missing. The impact of pH changes on blood clot formation was exclusively investigated with regard to platelet and endothelial cell activation in primary hemostasis [98, 99] and fibrin formation in secondary hemostasis [100]. pH changes below $pH \leq 7.0$ led to diminished platelet and endothelial cell activation and a reduction of the fibrin concentration. Therefore, the focus was set on the protection against excessive bleeding rather than thrombus formation. On the other hand, despite a pronounced decrease in platelet and endothelial cell activation accompanied with a diminished secretion of VWF from the Weibel-Palade-bodies, the clotting time (CT) remains constant. CT is defined as the time till blood clotting is initiated. Exactly this initiation process involves VWF activation and binding. Hence, although there is significantly reduced VWF release from platelets and endothelial cells, VWF binding (most probably directly from the blood stream) and its binding potential to platelets seems not to be impaired (see also figure 5.10). Therefore, it seems reasonable to propose an enhanced probability for the formation of VWF-platelet thrombi. Such thrombi would not, or to a minor extent, contain stabilising fibrin and develop their harmful nature only in small vessels. Of course, an increase in stretch-activation at lower pH is expected to induce an increase in ADAMTS-13 cleavage due to the altered substrate conformation. Using an static assay, ADAMTS-13 activity has recently been reported to strongly increase when the pH is below the physiological pH with an optimum around $pH \approx 5.5$ [28, 27]. These effects could at least partially compensate for the increased VWF activity and work against clotting. However, a complete picture of this fine yet robust equilibrium between clotting and cleaving requires to fully unravel the dynamics of all blood clotting processes, of which only the very first one is currently understood from a physical point of view.

In conclusion, these results provide an important insight for understanding VWF's response to mechanical stress and chemical stimuli. In fact, it is illustrated that charge can play a pivotal role in the activation of VWF and of biopolymers in general. This property can be tailored by using the right structure and sequence in a protein. In this sense, the presented results begin to bridge the gap between genetic mutations, physical properties and physiological implications for von Willebrand Factor related diseases.

5.1.5 Protein - Phase - Diagram

From the last chapters we know that the critical shear rate for unrolling the VWF molecule depends on the monomer-monomer interaction potential ΔU and can be fine-tuned by changing the solvent conditions of the protein in the medium. So far, quantifying the mechanical response of VWF fibres to external forces was limited to measurements with SAW driven microfluidics [1] or a custom designed shear cell using fluores-

cently labelled single proteins or analyzing the formation of complete networks. The resolution in either case is limited by the rapid movement of the free floating molecules while the fluorescence dye itself may slightly influence the protein dynamics. In the experiments presented in this section, an unlabelled VWF fibre was immobilised on an AFM tip and its extension on the application of a broad spectrum of hydrodynamic drag forces was monitored. The discussion of our results in combination with pH induced changes in the monomer-monomer interaction potential ΔU leads to a phase diagram displaying VWF's haemostatic activity as a function of external shear rate and pH .

Results

Similar to the bundle relaxation measurements, an AFM tip scans the surface for a preformed VWF conglomerate in our microfluidic AFM hybrid system (chapter 5.1.2). In this set of experiments, continuous flow was maintained while the tip penetrated a protein conglomerate and a VWF fibre was pulled out. The drag force of the fluid movement prevents complete relaxation of the VWF fibre to the cantilever tip where undefined and irreversible adhesion of the protein would occur. An extended and rigid VWF conglomerate, which was bound to the free end of the VWF molecule, mediated the pulling force on the fibre (figure 5.13). This approach is similar to the method of optical tweezers [101, 102], where a protein is pinned to a solid surface (the AFM tip in this case) and experiences forces mediated by a bead on the protein's second end. In the course of our experiment, an extremely thin VWF fibre (below the optical resolution of the microscope) was linked to the AFM tip and remained attached to a freely moving VWF-"bead". Continuous fluid streaming during the pulling sequence prevented total relaxation and irreversible adhesion to the AFM tip. When the power of the SAW is kept constant, the entire flow field becomes a function of the position inside the sample volume only [76]. Moving the immobilized VWF along the vertical axis of the flow field in small $50\mu m$ steps therefore allows probing the proteins response to hydrodynamic stresses as a function of the position inside the sample volume. Moving the immobilized VWF along the vertical axis of the flow field in small $50\mu m$ steps therefore allows probing the proteins response to hydrodynamic stress. With increasing relative cantilever height, the flow velocity and hence the acting force on the fibre steadily decreased, resulting in a slight reduction of the fibre length. Above a critical height, or in other words, falling below a critical force on the VWF-"bead", the protein fibre contracted in a non-monotonous fashion while the flow velocity still decreased continuously (figure 5.14).

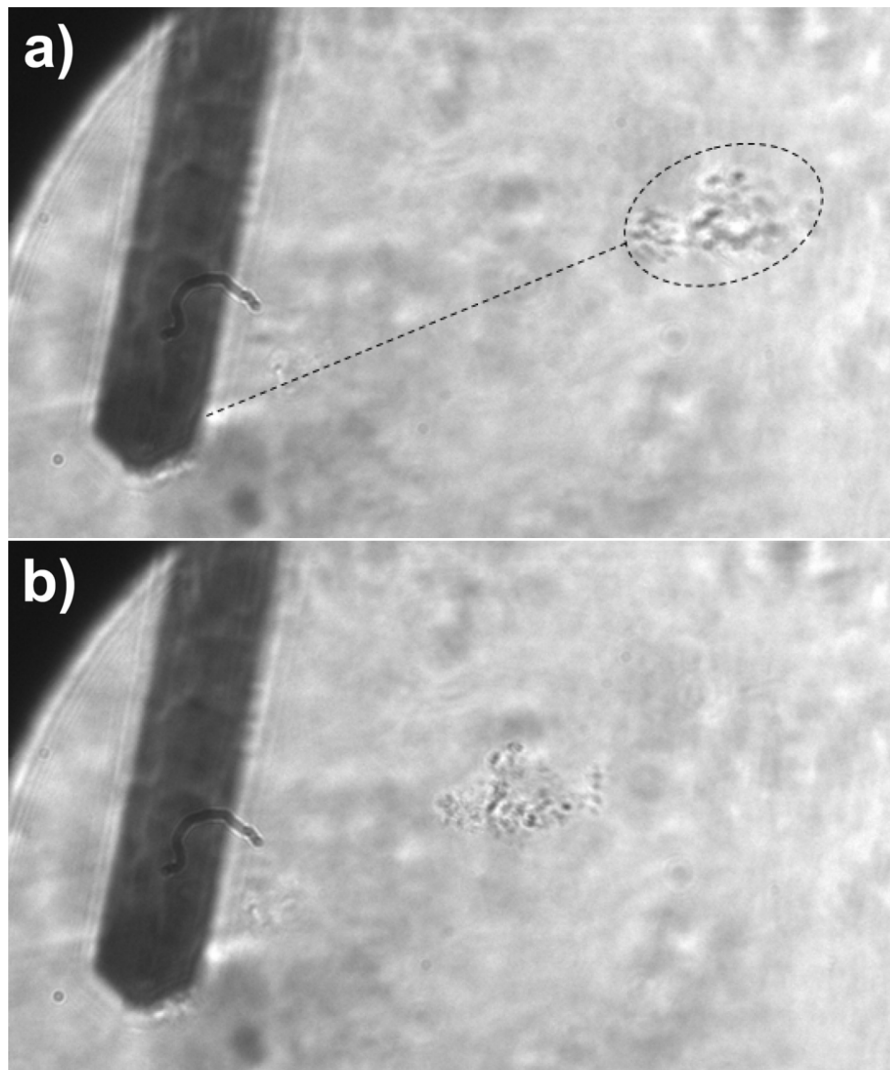


Figure 5.13: A thin VWF fibre, which can not be resolved optically, is stretched between an AFM tip and a VWF assembly (highlighted by the dashed circle). Hydrodynamic drag forces on the fibre mediated by a) high flow velocities lead to unrolling of the fibre whereas b) under low flow conditions the fibre contracts. In a first approximation, the VWF assembly can be described as a solid sphere and the drag forces can be calculated by Stokes friction (tip width $\approx 35\mu\text{m}$).

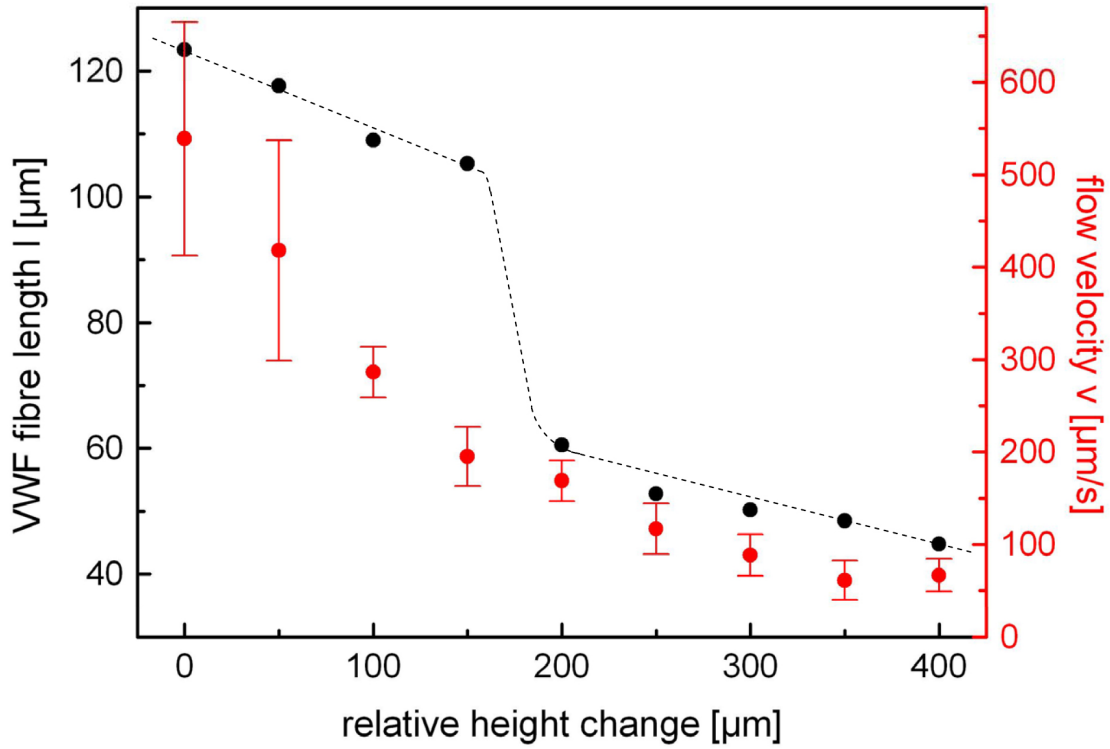


Figure 5.14: With increasing relative height the flow velocity decreases steadily (red). At the same time, there is a significant discontinuous reduction of the VWF fibre length at a relative height between 150 and 200 μm . Data were collected several hundreds of μm away from the surface, where wall effects can be neglected.

Discussion

The force on the tip bound VWF fibre is mediated by the friction forces of the rigid VWF conglomerate in the flowing buffer medium (velocity v , viscosity η). As a simple model, and for mathematical simplicity, the VWF assembly is modelled as a solid sphere with radius r . Doing so, the force f on the fibre can be easily calculated (Stoke's friction):

$$f = 6 \cdot \pi \cdot \eta \cdot R \cdot v \quad (5.5)$$

The analysis of the flow velocity v for every height step and the application of equation 5.5 yields the fibre length as a function of the effective drag force (figure 5.15 a). A clear transition from a collapsed to an unrolled regime is observed at a critical force of approximately $75 pN$. Different slopes before and after the transition indicate different elasticity of the fibre in its collapsed and elongated state. For large forces, the fibre length plateaus at the contour length of the polymer in agreement with the experiment. The small increase in the fibre length in the unrolled state upon application of additional force may have two reasons, acting at the same time. First, single elongated molecules

in a multi-molecule fibre may glide against each other (see also bundle relaxation in chapter 5.1.2). Second, there may be structural changes within the protein's secondary and tertiary structure due to destructive pulling forces [57].

The peculiar behaviour expressed in figure 5.15 a) comprises all features of a phase transition of first order. According to the Ehrenfest-classification, the order of the phase transition is characterized by the lowest discontinuous derivative of the free energy G at the transition point [103]. In our case, and compared to 3D, the volume V is replaced by the length l and the pressure p by the pulling force f . However, according to the well known proof of Landau, separated phases and therefore a phase transition between two states can not exist in one dimension. His hypothetical system is composed of a chain of interconnected units experiencing only next neighbour interactions. Each unit can exist in two distinct phases. Minimizing the free energy of this system leads to a complete mixing rather than phase separation, which includes the impossibility for a phase transition itself [104]. Similar to other reported obvious phase transitions in one dimension [105, 106], the VWF fibre under investigation does not perfectly fulfill the postulates of Landau's one dimensional system. The orientation of the chain of VWF monomers itself defines the phase state rather than the single monomer unit structure. Furthermore, distant monomers may interact with each other by hydrogen bonding, hydrophobic forces, hydrodynamic coupling, etc. From the experimentally observed force - strain relation the isothermal compressibility of the fibre can be calculated using the appropriate thermodynamic potential:

$$\kappa_T = \frac{1}{l} \cdot \frac{\partial l}{\partial f} = \frac{1}{l} \cdot \frac{\partial^2 G}{\partial f^2} \quad (5.6)$$

During the phase transition, the VWF molecule exhibits a pronounced discontinuity in its length change accompanied by a maximum in elasticity on the exposure of external forces. The isothermal compressibility κ_T is directly related to the length fluctuations $\langle l^2 \rangle$ of the polymer system [104]:

$$\kappa_T = - \frac{\langle l^2 \rangle}{k_T T \cdot l} \quad (5.7)$$

Hence, VWF molecules exhibit pronounced length fluctuations in the phase transition regime, where κ_T exhibits a maximum (figure 5.15). This is in perfect agreement with computer simulations including hydrodynamic interactions [1, 2, 78].

The absolute force values in figure 5.15 may contain a systematic error by simply assuming the VWF conglomerate as a solid sphere. Furthermore, the actual drag forces are calculated for the peculiar fibre of this very experiment. Moreover, it can not be distinguished if the fibre consists of a single molecule or a multitude of interconnected or crosslinked fibres. Nevertheless, the shape of the curves in figure 5.15 a) comprises a distinct length change at a critical force indicating that the observed fibre displays single molecule rather than bundle characteristics [75, 1, 2]. Hence, the related discussion should also be valid for single VWF molecules.

The phase transition of the VWF molecule from a collapsed to an unrolled conformation

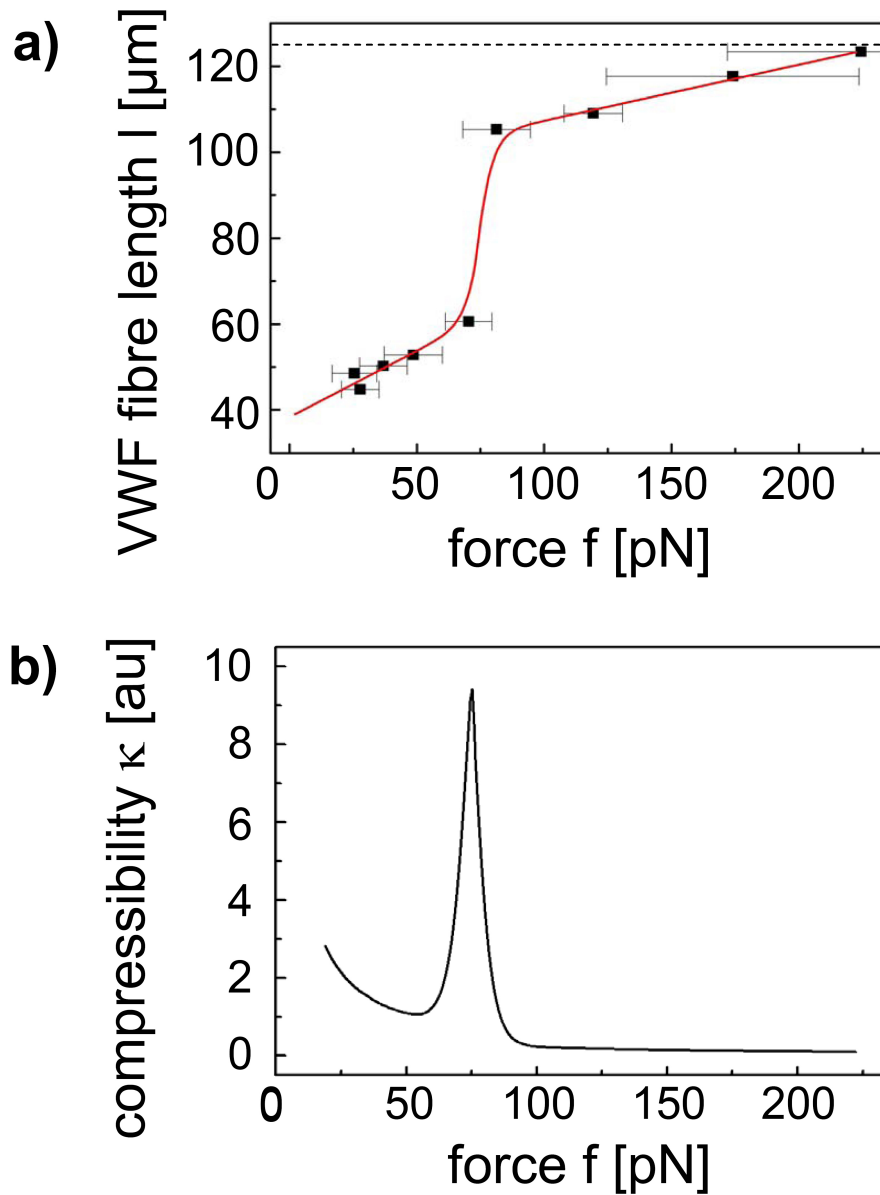


Figure 5.15: a) The length as a function of the applied pulling force (equation 5.5) exhibits a pronounced jump (at approximately 75pN) indicating a phase transition of first order. The red line is a fit to the data points. In the high force regime, the fibre length approaches the contour length of the protein (dashed line). The derivative of this fit with respect to the force f yields b) the one dimensional isothermal compressibility κ . κ is a measure for the fibre elasticity and shows a clear maximum at the phase transition.

is sensitively dependent on the pH of the surrounding medium. Combining the solubility results of the previous chapter with the concept of a VWF phase transition, it is possible to predict a phase diagram illustrating the activity of VWF as a function of both force, or shear stress respectively, and pH of the medium (figure 5.16). Although the axes of the phase diagram are given in arbitrary units due to the inclusion of results obtained with VWF fibres of different length and thickness, the presented conclusions are valid without loss of generality.

At $pH \approx 7.4$, an increase of the pulling force slightly deforms the VWF molecule until the polymer is fully elongated in an all-or-none fashion (induced by a critical shear stress for example). In its stretched conformation, the elasticity of the fibre is reduced compared to the collapsed state. The analysis of a stiff molecule, as VWF is assumed in a variety of simulations [1, 2, 78], would exhibit no length change in the elongated state at all. For pH values, which differ from blood pH , the critical shear rate and hence the critical force for the unrolling of VWF decreases as a result of a diminished monomer-monomer interaction potential ΔU . The blue area in the phase diagram illustrates the coexistence region where the molecules exhibit pronounced fluctuations of their size and both elongated and collapsed molecules coexist. A decrease in ΔU has drastic effects on the iso- pH curve as it not only shifts the critical force, but also changes the qualitative shape of the force-elongation profile. The packing density of the VWF molecule is reduced accompanied by a slight increase of the initial size of the molecule at zero force (transition from a collapsed to a coiled molecule (see chapter 3.1.4)). Furthermore, the slope within the phase transition regime increases with decreasing pH . This behaviour emphasizes a loss of cooperativity of the conformational change of the VWF molecule due to the reduction of the monomer-monomer interaction strength [1, 2]. Instead of a critical activation force or shear rate respectively, the phase transition is smeared over a certain force range. Fulcher et al denatured the VWF molecule by adding urea and found a global isoelectric point at $pH \approx 5.7$ [97]. In this conformation, all previously buried amino acid residues are now exposed to the external solution as a result of a vanishing interaction potential ΔU . For ΔU approaching zero, globular and stretched conformation of the VWF molecule become more and more indistinguishable and the phase transition itself disappears. Without an effective interaction potential, the "freely jointed chain" (FJC) polymer model [107] may be an appropriate approximation for the force-elongation behaviour of the VWF molecule [108]. Herein, a polymer is made up by a chain of N statistical orientated monomers while any interaction between its subunits is neglected. The restoring force upon pulling on the FJC polymer is a linear function of the elongation from its mean size (entropic spring). Another prerequisite for the construction of a phase diagram is that in the high force regime the fibre lengths of all iso- pH curves converge into one maximum length.

From a physical point of view, the phase transition of first order loses its cooperativity with decreasing pH and completely disappears at the critical point (or critical pH , respectively). An analogous behaviour can be found in the two dimensional compression of phospholipid membranes on a film balance at varying temperatures [109]. The discussion of a phase diagram for basic pH values follows the same lines.

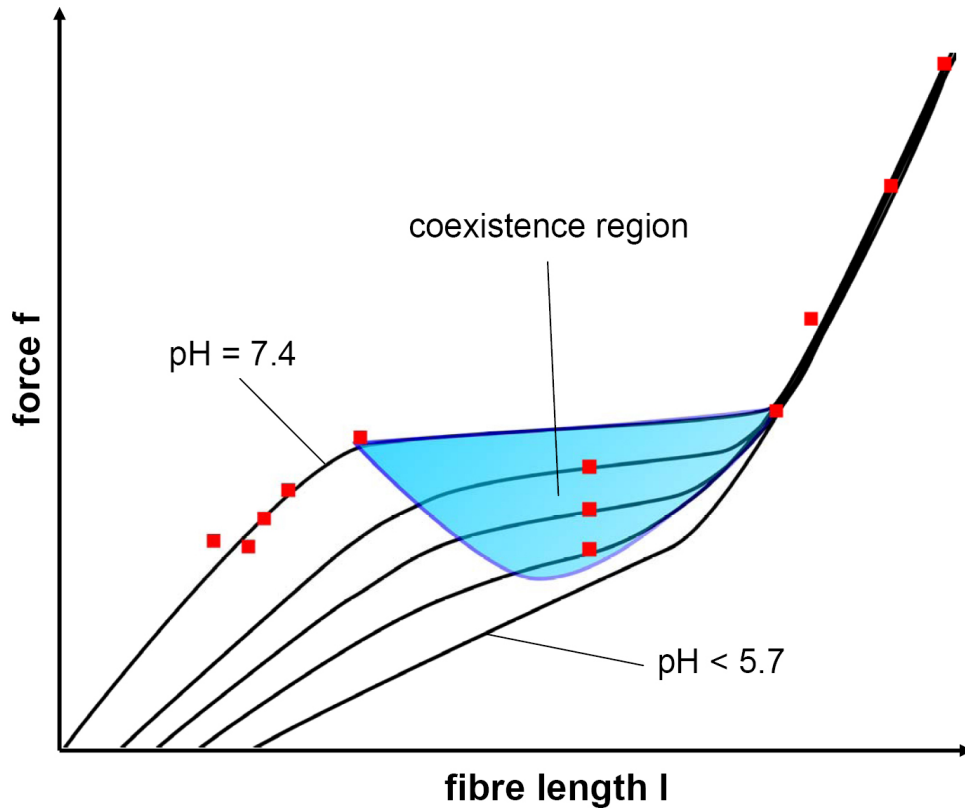


Figure 5.16: The schematic phase diagram illustrates the length change of VWF molecules upon the application of a stretching force f for various pH values of the surrounding medium (each line denotes a iso- pH force-elongation curve). At $pH \approx 7.4$, the force to unroll the VWF molecule is maximal and a sharp transition from a collapsed to an elongated state is found (the data points are taken from the results presented above). For decreasing pH , the transition curves change to smaller activation forces and lower cooperativity. At $pH < 5.7$, the interaction energy ΔU approaches zero. In this regime, no clear distinction can be made between a collapsed and elongated regime and hence no phase transition occurs. The blue area of the phase diagram denotes the coexistence region where the molecule exhibits strong fluctuation between the collapsed and the elongated conformation.

In order to obtain absolute values of length and force (or shear rate) for the phase diagram, optical tweezer experiments [110] with recombinant VWF molecules exhibiting a precise length distribution may be an improvement. Advanced protein engineering will allow the binding of beads to the second end of a VWF molecule immobilized on a surface. With the help of such a setup it will be possible to study complete force elongation curves with identical proteins at varying pH values. Nevertheless, the qualitative appearance of the VWF phase diagram won't change.

The implications of the VWF phase diagram can be directly adapted to our blood stream with significant meaning for biological, medical as well as clinical applications. A decrease in the vessel diameter accompanied by an increase of the shear rate under stenotic conditions will enhance the force on the VWF molecule and might lead to its activation. On the other hand, acidosis can locally change the pH value of the medium and directly affect the critical shear rate of the VWF molecule (see also discussion in section 5.1.4). The pathologically induced activation of VWF may have dramatic effects in the occlusion of blood vessels and possibly results in excessive clotting and thrombus formation. The phase diagram contains the entire information on VWF's haemostatic active state with respect to pH and shear and provides information about the interplay of both stenotic and acidic conditions. A precise determination of the pathological constraints inside a blood vessel in combination with the VWF activation phase diagram can lead to an improved medication and sloping of drugs and a more precise estimation of possible side effects for blood clotting.

5.2 VWF - Membrane - Interaction

The binding of VWF molecules to damaged endothelial cell walls has almost completely been neglected in the literature, so far. Conventional biological models focus on the lock-and-key interaction between specific protein ligands and membrane receptors. This is surprising because adhesion of VWF molecules to the complex cell surface accompanied by network formation requires at least an extended area of pure physical contact. Keeping in mind the observations of VWF activation, network formation and interacting forces between its monomeric subunits of chapter 5.1, the focus will now be set on the analysis of VWF interaction with phospholipid model systems mimicking the cell wall of endothelial cells and platelets. In particular, VWF conformation, phase state and electric charge of the membrane system will be under investigation regarding possible implications for blood clotting.

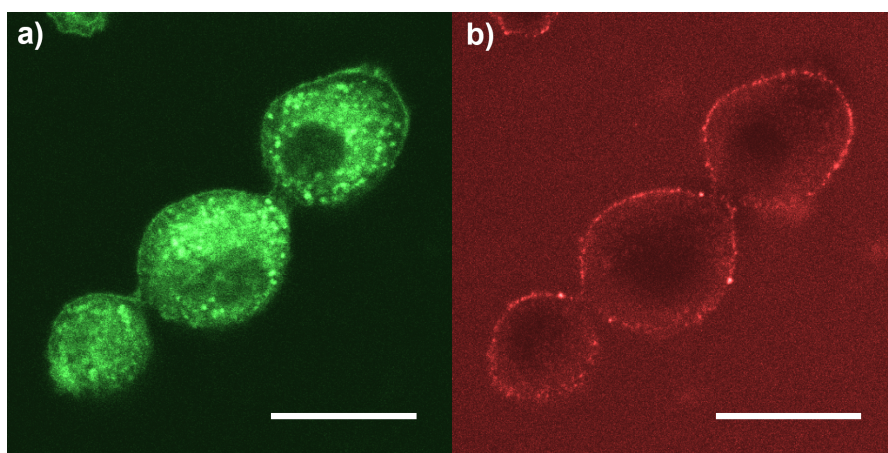


Figure 5.17: Endothelial cells were incubated in a VWF solution ($c = 10 \frac{\mu\text{g}}{\text{ml}}$) and double-stained with specific membrane and VWF fluorescence dyes. a) The fluorescence image of endothelial cells on a glass support with a membrane dye shows both plasma membrane and cell organelles. b) The protein seems to be solely distributed on the cell wall of the endothelial cells and does not enter the cytoplasm or organelles. (Scale bar $\approx 15 \mu\text{m}$)

5.2.1 Binding Model of Von Willebrand Factor to Cell Membranes

While specific binding sites within the VWF monomer for both compounds of the extracellular matrix and platelets has been identified [22], the binding behaviour of VWF to the pure cell membrane is still an open field. On the following pages, strong evidence will be presented for a tight bonding between model membranes and VWF molecules that is strong enough to form individual and haemostatically active VWF networks. Furthermore, the adhesion process is broken down to the basic building block of the protein by the analysis of the adhesion potential of recombinant VWF (rVWF) dimers

to phospholipid membranes.

Results

The extraordinary size of both the multimeric molecule and its single monomer unit has been identified as a key factor for VWF activation and its binding potential to sites of vascular damage upon arterial shear flow conditions. In this chapter, the generic interactions of both VWF multimers and dimers to endothelial cells (EC) were analysed by studying its binding behaviour to phospholipid membranes (see Appendix A for an introduction in phospholipid membranes). To account not only for static but also dynamic conditions, Differential Scanning Calorimetry (DSC), Fluorescence Microscopy and Circular Dichroism (CD) Spectroscopy were combined with Surface Acoustic Wave driven microfluidics.

Differential Scanning Calorimetry (DSC)

Microcalorimetry provides a powerful tool in measuring the phase transition of phospholipid membranes from the gel-like to the fluid state [111]. As the exact position of the phase transition exhibits subtle dependence on the actual phospholipid structure, any disturbance induced by solvents, pH or bound proteins will shift the phase transition [112, 113]. Furthermore, the use of free vesicles in calorimetry experiments excludes any disturbing side effects of a solid support. Hence, the measured influence can be directly attributed to an interaction of VWF with the membrane system.

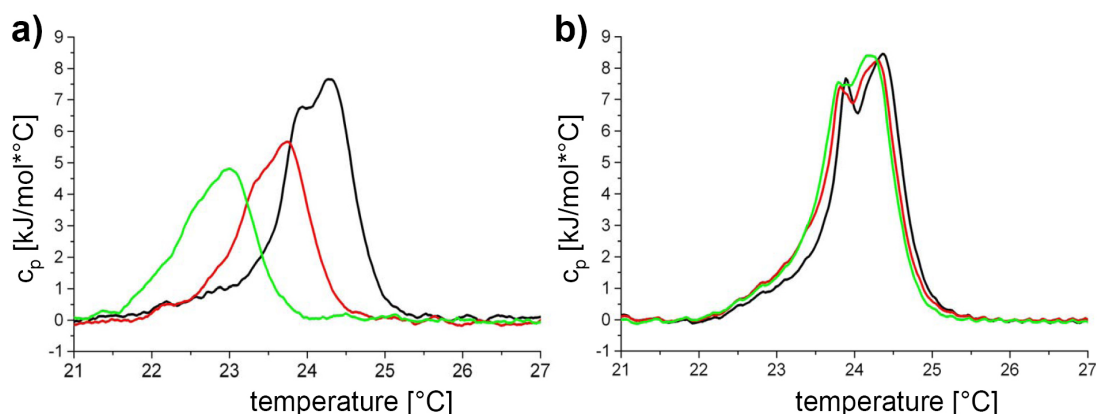


Figure 5.18: DSC measurements for both a) multimeric and b) dimeric VWF. Black curves denote the pure DMPC vesicles, red curves include the addition of VWF and DSC scans after the application of over-critical shear stress are coloured in green. Both the sole addition of protein and the subsequent application of shear resulted in a distinct shift of the phase transition temperature ΔT in the multimer in clear contrast to the dimeric system.

Differential heat capacity scans of the lipid dispersions of DMPC small unilamellar vesicles (SUVs) ($c \approx 0.3 \frac{mg}{ml}$) with and without VWF were performed with a Microcal VP-

DSC Micro Calorimeter (Microcal Inc., USA) at a heating rate of $5 \frac{^{\circ}C}{h}$ at high feedback mode. VWF was added to the previously investigated pure lipid sample to achieve a mass relation of approximately $\frac{m_{lipid}}{m_{VWF}} = \frac{50}{1}$ and scanned again. Before the last measurement, the VWF lipid dispersion was exposed to an over-critical shear flow in a surface acoustic wave (SAW) pumping cuvette for $5min$. Obtained data were analyzed using the routines of the Origin software (Microcal Inc., USA). For analysis, the phase transition temperature was defined as the mean temperature at half height of the DSC peak.

Incorporation of multimeric VWF into the membrane results in a distinct shift of the phase transition temperature ΔT compared to the pure DMPC membrane (figure 5.18 a). The application of over-critical shear stress to the vesicle-protein solution led to further decrease of the phase transition temperature. In reference measurements with protein free vesicle solutions, the phase transition temperature was not affected by shear stress. This provides strong evidence that the changes of the DSC signals after both the sole addition of VWF and its shear induced activation can be attributed to the interaction of the phospholipid membrane with the protein. The double peak found in our calorimetric measurements is a common feature for DMPC vesicles and was observed in a variety of studies [114].

The same set of experiments was performed with DMPC SUVs and dimeric VWF to test the interaction of the VWF subunits with phospholipid membranes. For optimal comparability, identical vesicle preparation and concentration was used. The experiments were performed with equivalent masses of phospholipids and proteins as described above. A shift in the phase transition temperature of only $\Delta T \approx 0.1^{\circ}C$ is observed with respect to the pure membrane upon the addition of VWF dimers (figure 5.18). The application of over-critical shear stress did not further decrease the phase transition temperature.

Fluorescence Microscopy

DSC data indicate a conformational dependent interaction of VWF multimers with phospholipid membranes. Fluorescence microscopy is able to provide optical evidence for the actual structure of VWF molecules on phospholipid membranes in both its coiled and unrolled conformation. Here, DMPC bilayers are prepared on a solid glass support and VWF molecules are added at a concentration of $c \approx 10 \frac{\mu g}{ml}$ (blood concentration). After giving the system several hours for equilibration, overcritical shear stress was applied to the membrane bound VWF molecules. Subsequently, the sample was excessively rinsed with buffer. VWF staining was performed without protein crosslinkers. Network formation with diameters in the range of $20\mu m$ and above took place on the supported membranes. Most VWF conglomerates exhibit two prominent structural features. Network-like regions were interconnected by string-like VWF bundles (figure 5.19). Manipulation of these structures with an AFM tip revealed that the network-like structures were tightly attached to the membrane while the string-like bundles seemed not to be bound to the surface. In clear contrast, network formation of VWF molecules was not observed without the application of shear flow. Randomly distributed spots with varying brightness were detected on the membrane, indicating the adhesion of single VWF multimers of different sizes.

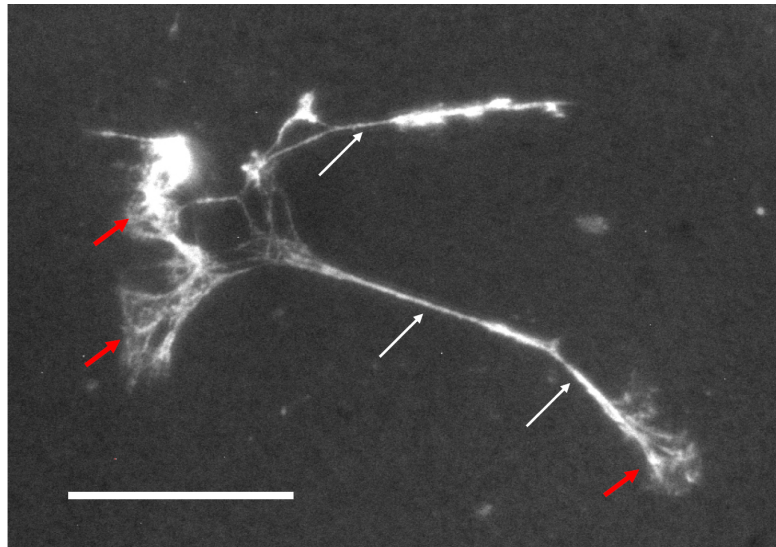


Figure 5.19: The image illustrates the two regimes of a fluorescently labelled individual VWF network on a supported bilayer. Red arrows indicate network-like regions, which are tightly connected to the membrane, whereas string-like VWF bundles (white arrows) do not comprise firm adhesion over their entire length. (Scale bar $\approx 20\mu m$)

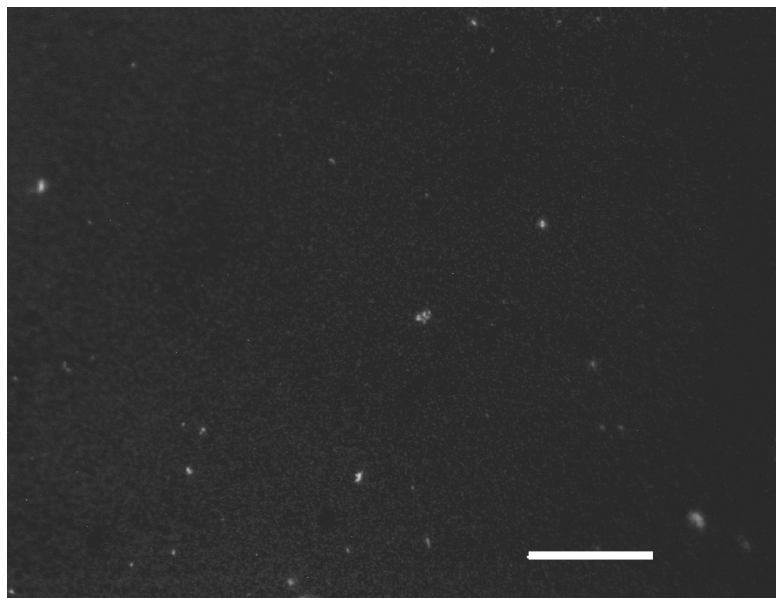


Figure 5.20: In contrast to multimeric VWF, no individual networks formed from dimeric VWF on the phospholipid bilayer. Few bright spots most probably indicate smaller conglomerates of self-assembled VWF dimers. The application of shear flow did not result in any detectable change of the dimeric distribution on the membrane. (Scale bar $\approx 20\mu m$)

The VWF dimer distribution on the phospholipid membrane (figure 5.20) resembled that of the unsheared VWF multimers. Differences in fluorescence intensity most probably originated from self-agglomeration of single dimeric units followed by the adhesion to the membrane. The application of shear stress with varying strength did not result in network formation.

Circular Dichroism (CD) Spectroscopy

Calorimetry and Fluorescence Imaging illustrated a significant conformational dependent interaction potential of multimeric VWF and DMPC membranes in clear contrast to its dimeric subunit. In order to achieve deeper insight into the molecular level of the interaction between VWF and phospholipid membranes CD spectroscopy experiments were performed. This technique allows for an estimate of the secondary structure of VWF as well as membrane and shear flow induced structural changes within the protein. Hence, CD data may connect molecular architecture of VWF molecules to its biological function. CD spectra were recorded for both multimeric and dimeric VWF (figure 5.21) before and after the application of shear stress. Furthermore, the influence of free DMPC SUVs on the VWF's secondary structure was investigated. Secondary structure was predicted by the CDSSTR algorithm (appendix).

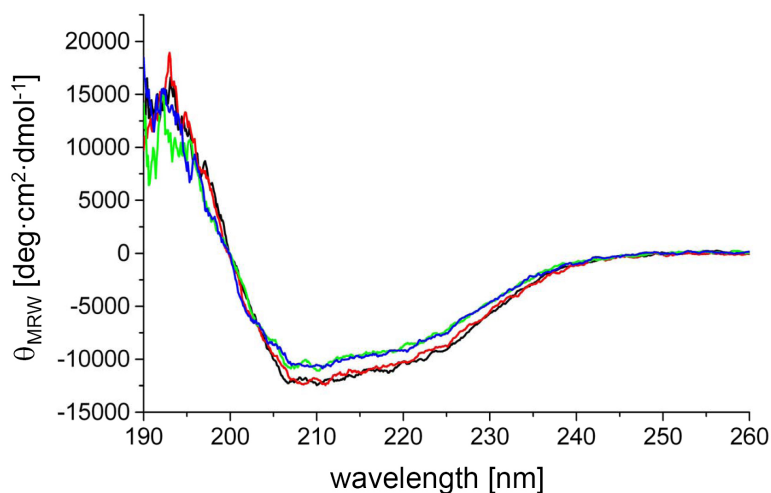


Figure 5.21: The CD Spectrum of pure dimeric VWF (black) is altered after the application of overcritical shear flow (green). The addition of DMPC SUVs to VWF dimers (red) with subsequent shearing (blue) resulted in a similar curve shift.

Table 5.2.1 summarizes the results for the analysis of the secondary structure for VWF multimers. The deconvolution software indicates only small conformational changes of pure multimeric VWF after the application of shear flow. While the amount of random coil remains constant, the fraction of α -helix is diminished on the expense of β -sheet. The addition of DMPC vesicles revealed an opposing effect. Due to the interaction

between protein and membrane new α -helices are formed whereas the amount of β -sheet and random coil slightly decreases. Subsequent application of shear stress to the protein-vesicle system affects the protein in a similar way as found for the pure protein solution. The actual increase in β -sheet and the decrease in α -helix are more pronounced in the membrane containing case.

multimeric VWF	pure VWF	after the application of shear stress	addition of vesicles	vesicles and shear stress
α -helix	31	29	35	28
β -sheet	21	23	20	24
random coil	48	48	45	48

Table 5.1: The fraction of α -helix, β -sheet and random coil was analysed in multimeric VWF. The percentage of pure VWF before and after the application of over-critical shear stress is displayed in the first two columns. Addition of DMPC vesicles to unsheared VWF already changes the secondary structure content. Further application of over-critical shear stress to this protein-membrane system resulted in an additional transformation of the protein's secondary structure.

The changes upon shear stress are more distinct in the dimeric form compared to the multimer both in the presence and absence of DMPC vesicles (Table 5.2.1). The structural changes within VWF dimers upon the addition of vesicles are comparable to the multimeric protein system. The stronger signal change in the case of dimeric VWF probably results from the higher amount of molecules exposed to vesicles compared to the same mass of multimeric VWF. In multimeric VWF, a certain proportion of subunits is buried within the polymer and inaccessible to both solvent and membrane. Consequently, less structural change is expected for multimers encountering vesicles.

dimeric VWF	pure VWF	after the application of shear stress	addition of vesicles	vesicles and shear stress
α -helix	31	23	34	19
β -sheet	21	27	18	30
random coil	48	49	48	49

Table 5.2: The secondary structure analysis of dimeric VWF followed that of multimeric VWF (see Table 5.2.1)

Discussion

The use of both free and supported membranes for the investigation of VWF interaction with phospholipid membranes may look like an over-simplification at first glance. Nevertheless, this combination may be an advantage in mimicking the properties of real cell membranes. Membranes in living organisms exhibit a lipid composition which allows

relatively free diffusion in two dimensions. Nevertheless, phospholipids are at least to some degree restricted in their movement due to the interaction with the cytoskeleton from the inside and the glycocalix from the outside. Exploiting the individual properties of free vesicles in DSC and CD Spectroscopy measurements and supported membranes for fluorescence microscopy can account for both properties of a cell membrane.

Calorimetry and fluorescence imaging revealed a conformational dependent interaction mechanism of VWF multimers with free phospholipid membranes. This finding by itself is remarkable as there are no specific binding sites within the phospholipid membrane which would account for an adhesion of neither the collapsed nor the unrolled polymer. Random binding of globular proteins resulted in a distinct shift of the membrane's phase transition temperature $\Delta T = T_M - T_{MP}$ ($T_{M/MP}$: phase transition temperature of the pure membrane system and the membrane protein system, respectively). ΔT can be directly related to the amount of protein segments incorporated into the bilayer x_P .

Assuming only protein incorporation into the fluid phase (see also results and discussions in chapter 5.2.2) the chemical potentials of the membrane $\mu(g)$ in the gel-like phase and $\mu(f)$ in the fluid phase are given by [115]

$$\mu(g) = \mu^0(g) \quad (5.8)$$

$$\mu(f) = \mu^0(f) + RT \cdot \ln(x_M) \quad (5.9)$$

The index 0 indicates the chemical potential of the pure membrane. The second term in equation 5.9 describes the change in the chemical potential of the pure membrane system upon integration of parts of the protein. Herein, x_M denotes the molar fraction of phospholipids in the protein-membrane system. It is related to the molar fraction of the incorporated protein segments into the membrane x_P by

$$x_M = 1 - x_P \quad (5.10)$$

The chemical potentials for the gel-like and fluid state equal each other during the phase transition.

$$\mu(g) = \mu(f) \quad (5.11)$$

$$\Leftrightarrow \Delta\mu = \mu^0(f) - \mu^0(g) = RT \cdot \ln(x_M) = RT \cdot \ln(1 - x_P) \quad (5.12)$$

Taylor-expansion of $\ln(1 - x_P)$ for small x_P leads to

$$\Delta\mu = RT \cdot x_M \quad (5.13)$$

Hence, the change in the chemical potential $\Delta\mu$ is directly related to the amount of incorporated protein x_M and can itself be assigned to the shift of the phase transition temperature ΔT by considering the Gibbs-Helmholtz equation [115]

$$\frac{\partial}{\partial T} \left(\frac{\Delta\mu}{T} \right)_p = -\frac{\Delta H}{T^2} \quad (5.14)$$

Integrating equation 5.14 from T_{MP} to T_M yields

$$\Delta\mu(T_M) - \Delta\mu(T_{MP}) = -\Delta H \cdot \ln\left(\frac{T_M}{T_{MP}}\right) = -\Delta H \cdot \ln\left(1 - \frac{\Delta T}{T_{MP}}\right) \quad (5.15)$$

While the change of the chemical potential $\Delta\mu(T)$ follows equation 5.13 at $T = T_{MP}$, it is zero at T_M . A Taylor-expansion of $\ln\left(1 - \frac{\Delta T}{T_{MP}}\right)$ for small $\frac{\Delta T}{T_{MP}}$ directly results in the proportionality of the change in the phase transition temperature ΔT and membrane incorporated protein segments x_P (melting point depression)

$$\Delta T = \frac{R \cdot T_M^2}{\Delta H} \cdot x_P \quad (5.16)$$

Strictly speaking, the proportionality $\Delta T \propto x_P$ is only valid for the integration of individual independent molecules into the membrane system without the formation of separate phases. In particular, the first argument is not true for the extended VWF molecule. Nevertheless, a first approximation of the degree of protein - membrane interaction can be achieved by examining the size of the temperature shift ΔT . ΔT seems to be sensitively dependent on VWF's conformation. Mechanical activation of the polymer into individual protein networks further decreased the phase transition temperature of the vesicles in relation to globular VWF. This behaviour clearly indicates an increased membrane - protein interaction in VWF's activated elongated state. On a molecular level, the shift of the phase transition temperature ΔT to lower values suggests a disturbing effect of the protein - membrane interaction on the lipid chain order. The phase transition peak originates from the "melting" of the hydrophobic phospholipid tails from an ordered, gel-like into a disordered conformation in the fluid phase. Any interaction contributing to an increased disorder of the side chains will therefore lower the phase transition temperature. Two binding mechanisms are possible. First, parts of the protein may penetrate the hydrophobic core of the membrane and directly induce fatty acid chain disorder. Second, the protein may adhere on the phospholipid headgroups. This can induce both ordering as well as distortion of the membrane structure. An enhanced phase transition temperature may be achieved by protein induced dehydration of the headgroups. The lack or reduction of solvent molecules increases the packing density and the order of the phospholipids. On the other hand, the protein may change the headgroup solubility with an inverse effect on the phase transition temperature. Considering the sheer size of the VWF protein, a molecular picture most probably involves both the penetration of the hydrophobic core and the adhesion to the hydrophilic headgroup region of the membrane.

On supported phospholipid membranes, VWF conglomerates and networks consisted of a multitude of unrolled and crosslinked single VWF multimers. Herein, regions of network-like structures were interconnected with stretched VWF bundles of varying thickness. These bundles were, at least in some parts, not tightly connected to the underlying surface. In order to keep the bundles elongated, the relaxation forces [75] have to be overcome by a tight binding to the membrane at regions which show a higher density of network-like structures. Therefore, the network formation process seems to

be accompanied by the development of anchoring points within the membrane which are able to span complete VWF networks in the range of dozens of μm . The limited diffusion ability of phospholipids in supported membranes [116] may be the reason for the formation of protein anchors capable of withstanding these relaxation forces.

In free DMPC SUV membranes the appearance of activated VWF networks may look slightly different. Networks are limited to the size of the vesicles (unless they do not connect several individual vesicles) and the unhindered diffusion does not prevent the relaxation of stretched bundles or fibres. Such protein structures may appear more like bulky conglomerates than two dimensional networks (figure 5.22).

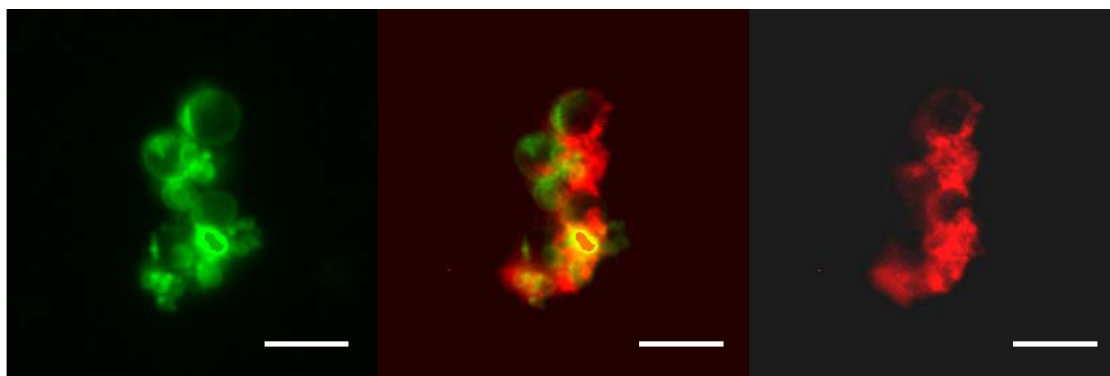


Figure 5.22: Double staining of free DMPC vesicles (left) and attached VWF (right) exhibits protein conglomerates rather than two dimensional networks. The overlay (middle) points out the spatial distribution of protein and membrane within this structure. (Scale bar $\approx 10\mu m$)

Nevertheless, networks similar to that in figure 5.19 may form on the cell membrane of endothelial cells due to restrictions of the glycocalix and the cytoskeleton and build the adhesive basis for platelets out of the blood stream. In addition, both DSC and CD spectroscopy revealed an enhanced interaction of VWF multimers after activation. The reason for this behaviour is most probably found in the exposure of a multitude of previously buried interaction sites in the elongated VWF molecule.

After giving strong evidence for a tight and conformational dependent adhesion mechanism of VWF to phospholipid membranes, the analysis was broken down to VWF's dimeric subunits. DSC data of DMPC vesicles incubated with dimeric VWF suggest only weak interaction between protein and membrane. Separated VWF dimers seem to interact with the membrane to a lower extent than the same mass of interconnected VWF dimers does. This finding is in contrast to CD data, which elucidated a pronounced interaction of both dimers and multimers with phospholipid membranes. So far, a comprehensive explanation for the differences obtained in DSC and CD measurements of dimeric VWF is missing and the molecular mechanism remains unclear. A qualitative defect or degeneration of the VWF molecules can be excluded. The identical distribution in secondary structure of both VWF dimers and multimers in CD analysis proofs the

quality of the recombinant protein and indicates that dimers are real building blocks of VWF multimers. CD data suggest that the impact of the membrane produces excess α -helical structure within the protein on the expense of random coil for the multimer and on the expense of β -sheet for the dimer. In a variety of trans-membrane proteins, α -helical structures are known to be incorporated into the hydrophobic core of the membrane bilayer [117]. The additional α -helical fraction of VWF possibly penetrates into the membrane structure and might build anchoring points for spanning individual VWF networks. A possible VWF binding model to cell membranes is illustrated in figure 5.23. The change in secondary structure upon the application of shear flow is similar with and without membrane. However, it is more pronounced when a membrane is present. The membrane may act as an additional surface mediating increased shear flow [78] and hence resulting in a more complete unrolling of the protein. Whereas in the pure VWF solution the protein may unroll only fragmentary (probably accompanied by the formation of smaller VWF aggregates), shear stress in close vicinity to a surface enhances the amount of unrolled VWF and therefore amplifies the change in secondary structure.

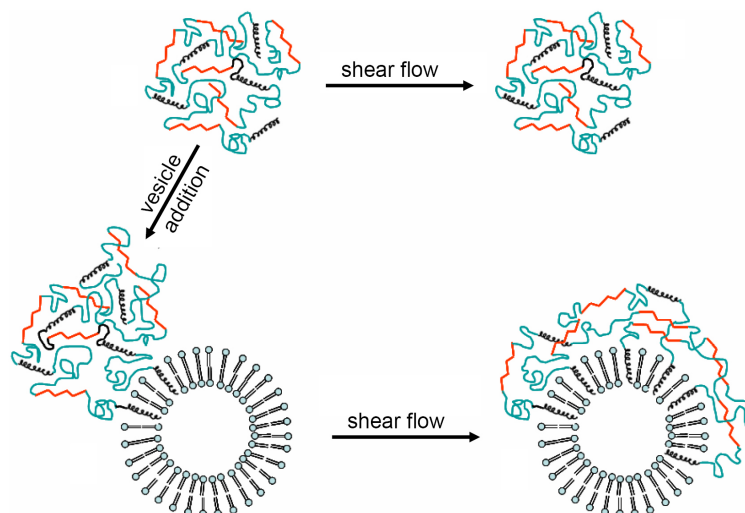


Figure 5.23: The addition of VWF to a phospholipid bilayer leads to adhesion of the protein by the formation of α -helical anchoring points. The application of shear stress leads to an unrolling of VWF on the vesicle surface which induces the formation of additional α -helical anchors while in the parts of the protein without direct contact to the membrane α -helix is transformed in the more stable β -sheets. Although the conformational change from the collapsed to the elongated state of free VWF molecules seems to be reversible, the change in secondary structure is not.

The susceptibility of multimers to conformational changes upon critical shear stress was observed in a variety of experimental studies as well as described theoretically. Most

of these papers treated the conformational change of VWF from its collapsed into the elongated state as reversible transition [1, 2, 78]. Indirect hints in literature for non-reversibility were not interpreted in a way that the reversibility of this process was doubted. Several studies, in which the proteolytic degradation of VWF after the application of shear stress was analysed, revealed an enhanced degradation compared to unsheared reference proteins [28]. This is only possible when there are irreversible structural alterations within the protein upon the application of shear stress. The CD data presented above give direct evidence for this irreversibility in secondary structure for the first time.

Furthermore, the molecular origin of VWF activation and its minute changes in secondary structure were traced back to their dimeric subunits. In this sense, an outstanding finding is that already VWF dimers are susceptible to shear stress. This gives direct proof that the treatment of VWF dimers as monomeric and rigid building blocks is a simplification. Such a treatment may be fruitful for theoretical considerations but cannot account for a clear molecular picture. Actually, these conformational changes within the dimer structure may be a prerequisite for the unrolling of the multimer as they directly affect the interaction with adjacent dimers within the globule. Shear flow induced changes in its secondary structure may contribute significantly to the observed all-or-none behaviour of VWF activation. In this sense, it seems likely that VWF activation from a collapsed into an unrolled conformation already originates from structural changes in its dimeric subunit.

In summary, the results presented in this section helped to clarify some existing and misleading concepts of VWF. Tight conformation dependent adhesion of VWF to phospholipid membranes, including network formation, was observed in the absence of any specific lock and key binding sites. Furthermore, the reversibility of the transition from the collapsed to the unrolled state could be disproved on a molecular level. This irreversibility was found to originate from structural changes within VWF's dimeric building blocks, which were treated as solid and unalterable bodies up to now.

5.2.2 Investigation of the Binding Forces of von Willebrand Factor (VWF) to Phospholipid Membranes by Atomic Force Microscopy

To date, blood clotting and wound healing was examined almost exclusively in the light of specific binding between blood clotting factors and the extracellular matrix. The endothelial cell wall itself and especially the lipid matrix of the membrane did not receive much attention in the course of wound healing. In the previous chapter, it was shown that VWF forms tight bonds and even large haemostatically active networks on pure phospholipid membranes without the presence of specific protein binding sites within the membrane. In this context it is worth mentioning that specificity does not necessarily imply molecular lock and key forces. If, e.g. VWF only binds tightly once a variety of independent variables (e.g. membrane and glyocalix composition, pH , shear flow, electrostatic interaction, protein hydration shell, etc.) exhibit a distinctive combination of values, the binding process becomes specific by the complex combination of generic interactions. Since VWF adheres only significantly above a certain hydrodynamic shear

[1], the binding to the endothelial cell wall could become quite specific once VWF reacts sensitive to the physical properties of the endothelial cell membrane (fluid, gel, charged, etc.). Of course, this does not exclude the importance of lock and key forces for the process in general, but allows extending the idea of specific binding, which might be crucial in order to understand binding under dynamic conditions where static binding models fail.

In this section, the concept of VWF-membrane interaction is extended and specific factors of the phospholipid membrane such as phase state, electrostatics or chain length are tested for their contribution to VWF binding. A special challenge for the AFM force spectroscopy experiments is the enormous weight and length of the VWF molecule. Two mature VWF monomers, which consist of 2050 amino acids with a weight of about $278kDa$, form a dimer. After multimerisation of up to 100 dimers, mature VWF multimers can gain diameters in the range of $1\mu m$ in the globular conformation. Such extremely large proteins have never been investigated with an Atomic Force Microscope before.

Results

Atomic Force Microscopy (AFM) techniques represent an effective method for investigating interactions between surfaces and adhering substances. Here, this method is exploited as an imaging tool for the determination of the precise arrangement of VWF on phospholipid membranes. In addition, minute interaction forces during protein-membrane binding are analysed. In order to elucidate potential binding preferences, AFM imaging and AFM Force Spectroscopy experiments were performed with VWF on supported membranes with varying phase state, electrical charge and phospholipid composition.

AFM Imaging

The phase state of a biological membrane is a crucial parameter for many essential tasks inside a living organism. These include, e.g. membrane fusion, budding, and nerve propagation to name only a few. Furthermore, it is also able to trigger the activity of membrane proteins [118]. Schmitz et al. and Loidl-Stahlhofen et al. described a method which they call "phase transition chromatography" (PTC) based on the phase dependent binding potential of proteins to phospholipid bilayers [119, 120]. To investigate the impact of the membrane phase, the binding behaviour of VWF molecules was analysed on supported fluid DOPC and gel-like DSPC membranes at room temperature. These phospholipids exhibit identical headgroups and chain length and differ only in an unsaturated bond within the hydrocarbon chain of DOPC. Although almost chemically identical the binding of VWF to these substrates shows significant differences (figure 5.24). Adhesion of single VWF molecules on the DOPC bilayer occurred in a random manner with varying heights and diameters according to a broad VWF size distribution. Upon the application of shear stress, extended individual networks consisting of unrolled and crosslinked VWF molecules were observed (see also chapter 5.2.1). The binding behaviour of VWF on the DSPC bilayer exhibits a different appearance. A network-like

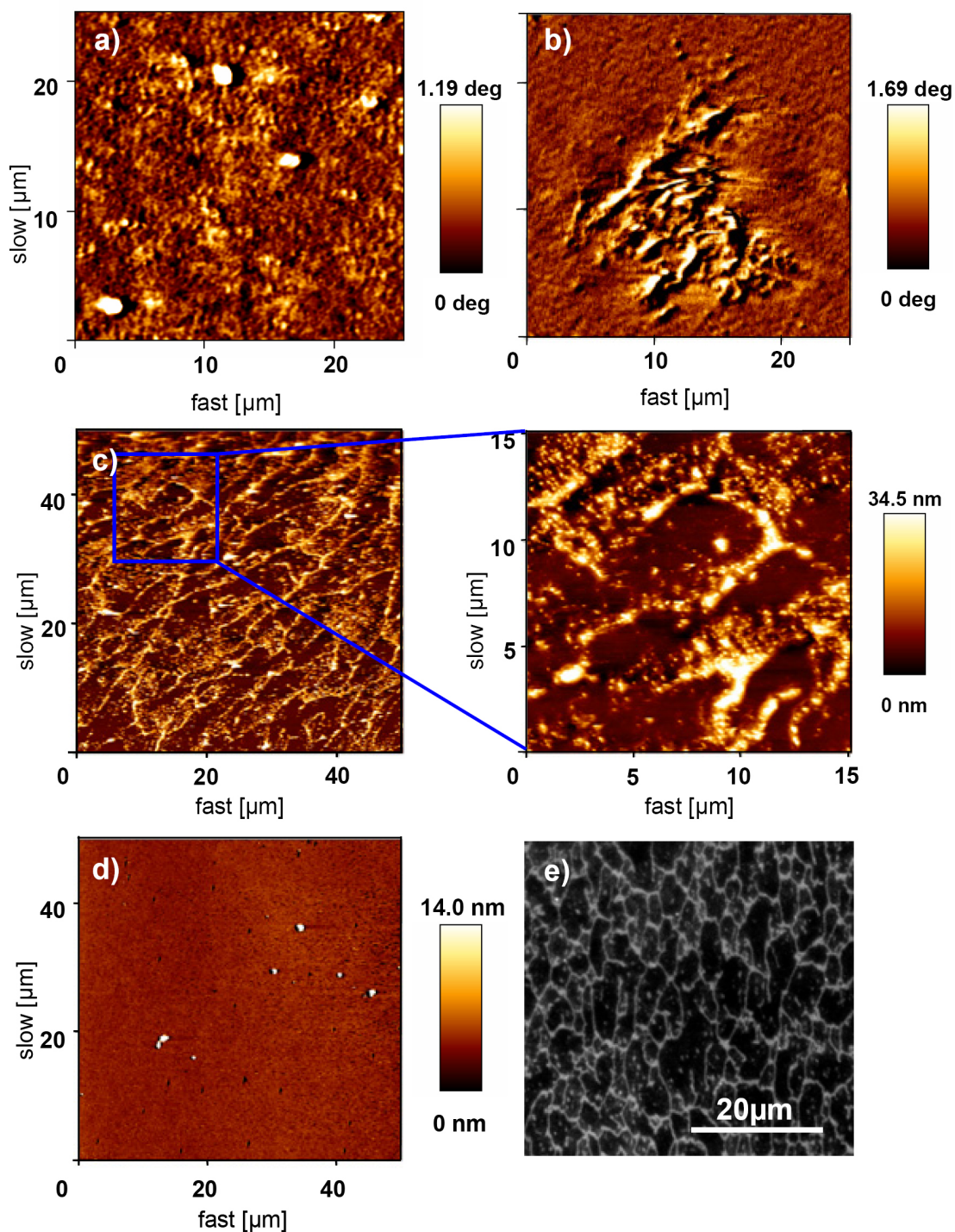


Figure 5.24: a) Single VWF molecules are randomly distributed on a fluid DOPC Bilayer with molecule heights ranging up to 30nm), whereas b) individual networks, which consisted of unrolled and crosslinked VWF molecules reached heights up to 180nm on DOPC bilayers after the application of shear stress. c) Network-like VWF structures consisting of single globular molecules (zoom) are observed on gel-like DSPC bilayers. d) The DSPC reference membrane without VWF molecules exhibited a molecular flat surface with few dirt particles, only. e) Fluorescence imaging of the DSPC reference membrane further revealed a two dimensional "grain boundary" structure within the flat membrane.

structure of VWF molecules formed on gel-phase DSPC bilayers. High resolution imaging of a smaller scan area revealed that these network-like structures are composed of single globular VWF molecules (Figure 5.24 c) rather than crosslinked fibres on DOPC membranes. Shear stress did not result in the formation of extended individual networks on DSPC. The reason for the network-like structuring is hidden in the membrane itself. Fluorescence imaging of membrane references without the protein gave evidence for a corresponding pattern inside the membrane, while AFM scans only exposed a molecular flat surface. This pattern inside the gel-like DSPC membrane may arise from the membrane transfer on the substrate and can be regarded as two dimensional "grain boundaries". So far, single VWF molecule adhesion is observed both on a fluid and a gel-like membrane but seems to have distinct differences in both cases.

In the next set of experiments, the membrane system was extended to binary phospholipid mixtures. These experiments aimed towards the investigation of the influence of the electrical charge of the membrane headgroups on the binding behaviour of VWF. Therefore, DSPC membranes with either 50% DOPC (neutral), DOTAP (positively charged) or DOPA (negatively charged) were prepared. Phase separation of gel-like DSPC and fluid DO-lipids led to the formation of electrically charged domains, which could be observed in both AFM imaging and fluorescence microscopy control experiments. On DSPC-DOPA bilayers random adhesion with no preference to a particular phase is monitored. Control bilayers exhibited a comparable domain structure within an intact membrane. Analysing both the DSPC-DOTAP and DSPC-DOPC mixtures an extensive defect pattern of membrane holes is observed. These holes are enriched in the DOTAP and DOPC rich domains, respectively. The defects itself comprised a heterogeneous appearance ranging from complete membrane loss down to the glass substrate to the loss of only one monolayer comprising a hydrophobic monolayer towards the buffer environment. Unlike the adhesion of VWF on the defect-free DSPC-DOPA membrane, binding of the protein to DSPC-DOTAP and DSPC-DOPC clearly followed the defect architecture of the membrane (figure 5.25).

Comparable AFM imaging experiments were performed on monolayers featuring the same lipid composition as described above. The DSPC and DOPC monolayers were stable in buffer environment for the time of the experiments. Although DSPC monolayers exhibit equivalent network-like membrane structuring as observed for the DSPC bilayer, no preference in VWF binding to either membrane could be found. VWF adhesion to both DSPC and DOPC monolayers resulted in a random distribution of single molecules on the membrane. Furthermore, extended individual networks formed without respect to the membrane phase state. VWF adhesion on mixed monolayers exhibited identical features. Extended individual networks formed and were accompanied by randomly distributed single VWF molecules. It has to be stated that the mixed monolayers were not as stable as the pure DSPC or DOPC monolayers and developed defects and holes during the experiment.

By applying a critical shear flow to the membrane bound single VWF molecules, it was possible to induce VWF unrolling and network formation on phospholipid membranes. Unlike the network-like VWF structures on DSPC bilayers, which were made up by the alignment of single collapsed molecules, individual networks consisted of unrolled and ag-

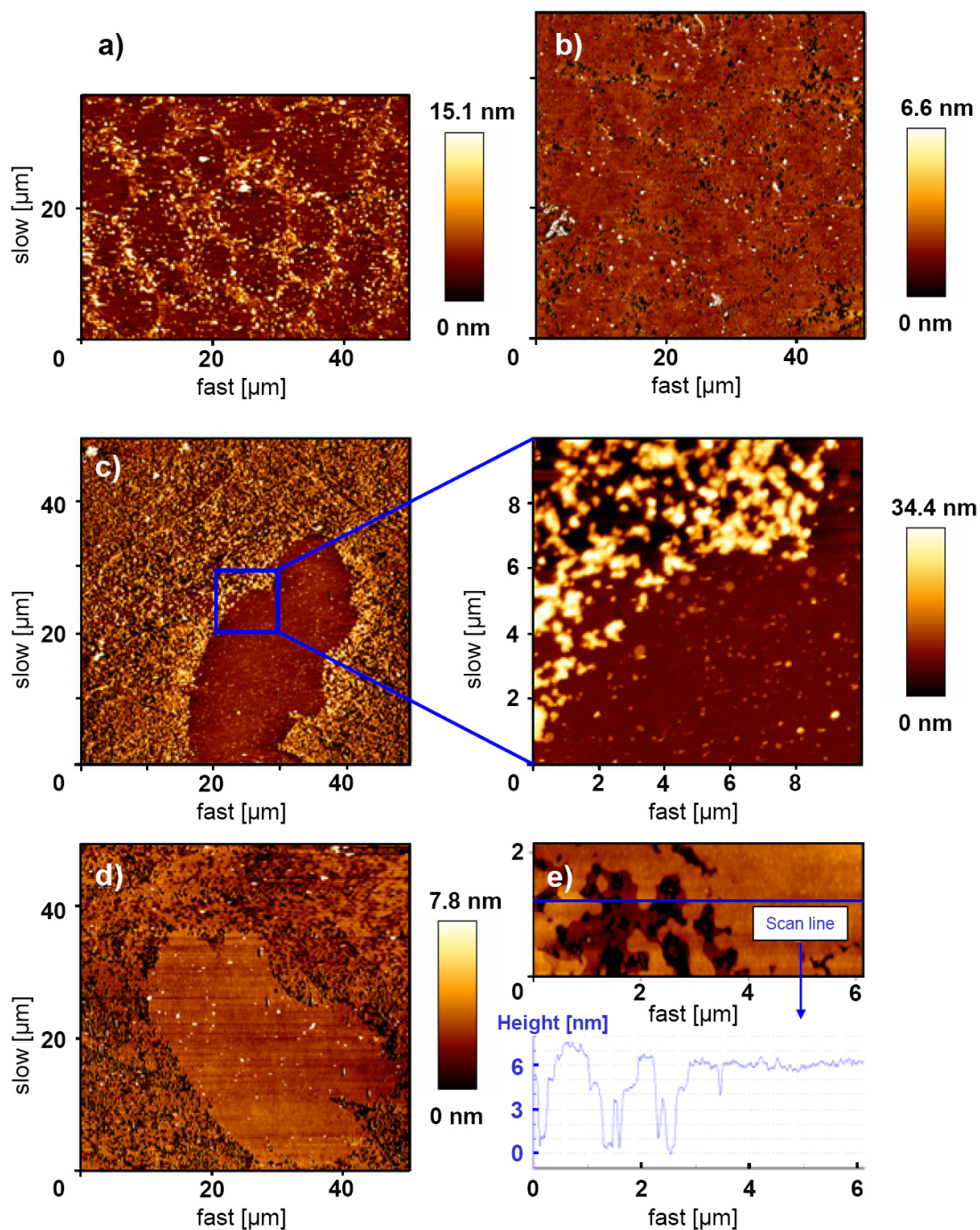


Figure 5.25: a) Single VWF molecules arrange in a certain pattern on a DOTAP-DSPC bilayer membrane. b) The pure reference membrane showed a similar behaviour comprising a system of holes within the membrane. c) VWF on DOPC-DSPC also showed a distinct adhesion pattern of VWF molecules and d) an analogous defect pattern on the pure membrane. e) The zoom into the bilayer membrane revealed that defects formed by the loss of either the complete bilayer down to the glass substrate or the loss of only one monolayer.

glomerated VWF molecules (figure 5.24). Individual networks only formed on pure fluid bilayers, lipid mixtures and on monolayers (see discussion below). AFM imaging of complete individual networks turned out to be difficult. Beside the shear size and stickiness of most of these networks, two regimes are frequently found. Imaging of firmly attached networks was performed easily without deformation or displacement of the protein from the surface. Stretched bundles between these structures could be easily detached from the membrane and bend by the AFM tip like elastic straps during scan cycles.

AFM Force Spectroscopy

In order to measure the actual interaction forces between VWF and phospholipid membranes AFM Force Spectroscopy measurements with tip bound VWF were performed. As discussed above, the focus was set on the dependence of VWF's binding potential on lipid phase state and electric charge. All membranes used for force spectroscopy measurements were stable during the course of the experiment and did not comprise detectable defects.

Force spectroscopy curves contain two kinds of information. The shape of the force distance cycle displays information about the nature and origin of the interaction (see also chapter 4.1.2) while the value of the adhesion force defines the strength of the tip-sample interaction. The appearance of the force distance cycles is heterogeneous for most membrane surfaces (figure 5.26). As a measure for the interaction strength, the rupture or unbinding forces of the protein from the surface were evaluated in at least 500 individual force distance cycles. This marks the importance of the force on the surface-bound VWF to unbind a part of the molecule from the surface or the complete protein, respectively. The approach and retraction speed was kept constant at $1.8 \frac{\mu\text{m}}{\text{s}}$. The extended delay, i.e. the time while the cantilever remains pressed on the surface after the maximum of the preset contact force is reached, was set to 10s. Lowering the extended delay to 1s or 0s resulted in a decrease in the unbinding forces in each case indicating a time dependent adhesion and relaxation process of the protein on or within the phospholipids membrane in the range of seconds to minutes (figure 5.27 a). Although comprising identical force constants, the actual values for rupture forces slightly depend on the cantilever used for the experiment. The reason for this behaviour is found in the broad size distribution of VWF molecules and the statistical binding of the protein to the tip during the cantilever preparation. The interaction forces of the cantilever tip with the surface will increase with increasing molecule size and the amount of VWF molecules bound tightly to the interacting part of the tip, respectively. Nevertheless most cantilevers featured an almost complete surface covering with VWF molecules and showed similar rupture force distributions with discrepancies smaller than 50pN . Reference measurements were performed with VWF free cantilevers. Only data with reproducible differences between reference and VWF sample were considered for analysis.

In a first set of force spectroscopy curves, the dependence of VWF adhesion on the lipid phase state was examined. The rupture forces are clearly enhanced for the fluid DMPC compared to the gel-like DSPC membrane (figure 5.27 b). Furthermore, the total amount of unbinding and therefore binding events in first place is distinct higher

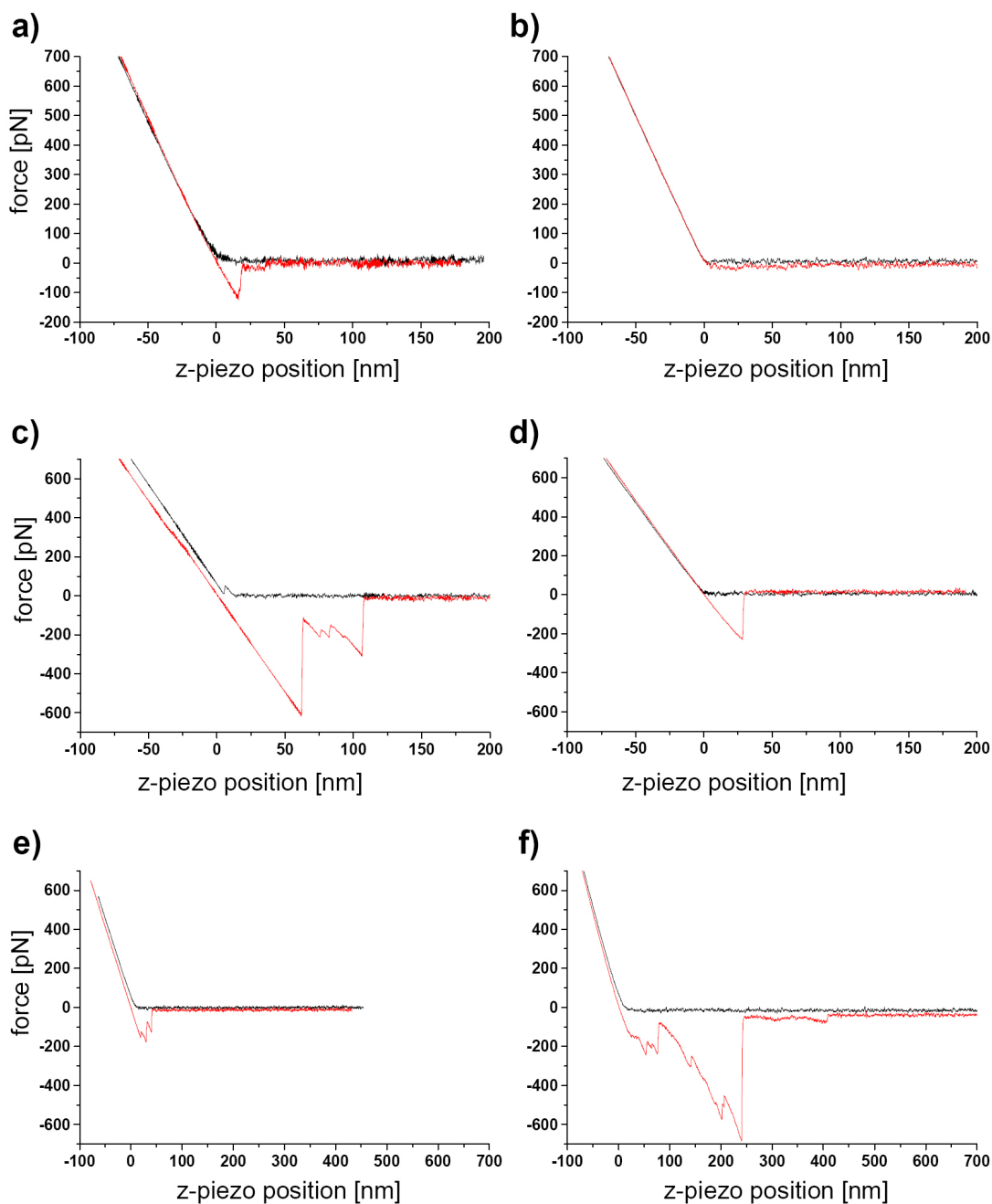


Figure 5.26: The force - distance cycles of VWF immobilised on an AFM tip display heterogeneous behaviour and no clear tendency can be determined. Nevertheless, most cycles feature simple adhesion characteristics (see also figure 4.2) with multiple unbinding events in some cases. In comparison to a) fluid DOPC bilayers, b) gel-like DSPC membranes show almost no protein adhesion at all. c) VWF binding to DOPC monolayers on the other hand frequently resulted in multiple unbinding events. d) Force curves of VWF on DOPC doped with 10mol% DOTAP (or DOPA - data not shown) resembled the characteristics of binding to pure DOPC, but occurred more frequently and at slightly higher force values. The evaluation of the dependence of the force - distance cycles on VWF conformation exhibits a pronounced increase of binding events from e) globular VWF f) to unrolled VWF on DMPC membranes. The extended delay was 10s for each measurement.

for the fluid membrane. In addition to the phase state, the influence of electrostatics on the protein-membrane-interaction was analyzed. Charged membranes were prepared by mixing neutral DOPC with either 10mol% of DOPA or DOTAP lipids, respectively. Unlike mixing with gel-like DSPC, lipid separation or domain formation did not occur. Both the negatively and positively charged membranes exhibit higher interaction forces with VWF compared to the pure DOPC reference bilayer (figure 5.27 d).

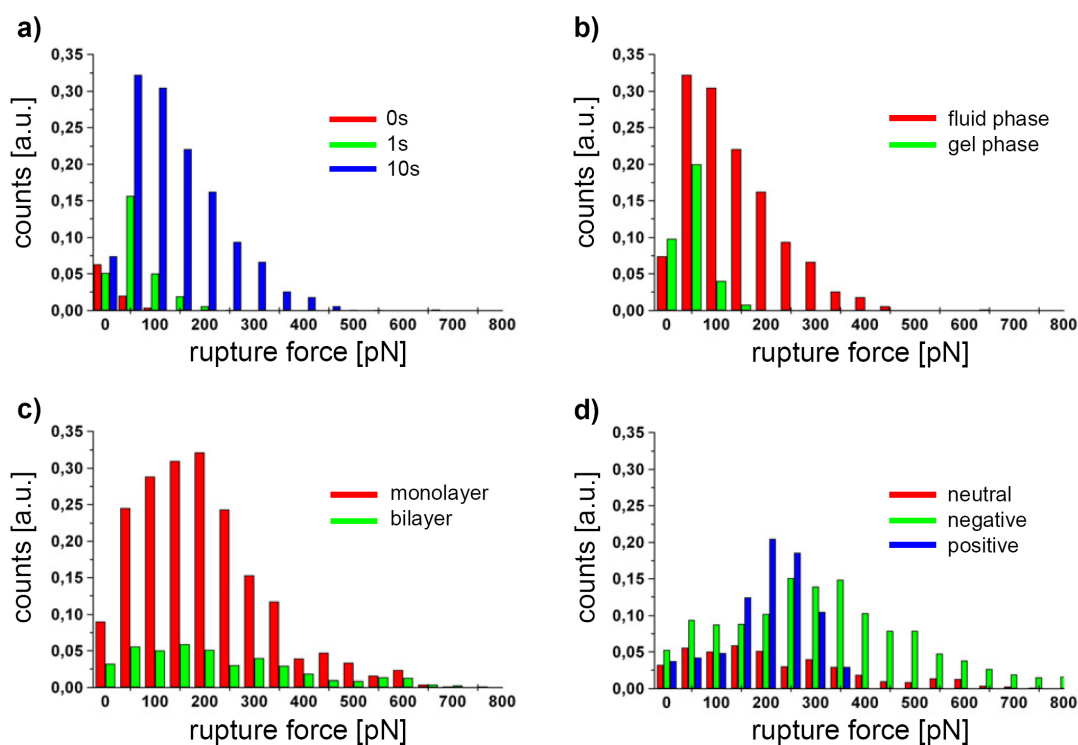


Figure 5.27: a) Variation of the extended delay from 0 to 10s increased the forces necessary to unbind VWF from a DMPC bilayer. b) Both the amount of unbinding events and the distribution of rupture forces is enhanced for a fluid DMPC compared to a gel-like DSPC membrane. c) The influence of the hydrophobic/hydrophilic properties on the adhesion of VWF was tested on both a DOPC monolayer and bilayer. Whereas the rupture force distribution does not change, the amount of binding events is dramatically increased. d) Both negatively (DOPC + 10mol% DOPA) and positively (DOPC + 10mol% DOTAP) charged membranes shift the maximum of the unbinding force distribution to higher values compared to a neutral DOPC membrane. The counts were normalized on the amount of force distance cycles.

This observation goes along with the imaging experiments of chapter 5.2.1, where no difference in the adhesion of VWF to oppositely charged membranes could be found besides the contribution of membrane defects. On the other hand, membrane defects comprised hydrophobic surfaces of the remaining monolayer. The monolayer does not significantly influence the values of the rupture forces compared to the bilayer system, but it results in a pronounced increase in the amount of unbinding events. So far, Force Spectroscopy measurements were performed with tip-bound VWF in the collapsed conformation. In order to analyse the dependence of the interaction forces on VWF conformation, tip-bound protein was mechanically activated at $pH \approx 6.5$, which led to the formation of networks on the AFM cantilevers (figure 5.28 a). The differences in the unbinding forces in PBS++ buffer between collapsed and unrolled VWF were of quantitative rather than qualitative nature (figure 5.28 b). Whereas the distributions resembled each other in the basic characteristics of the curve, a drastic increase in unbinding events could be observed in the activated conformation. The chain length itself did not show any influ-

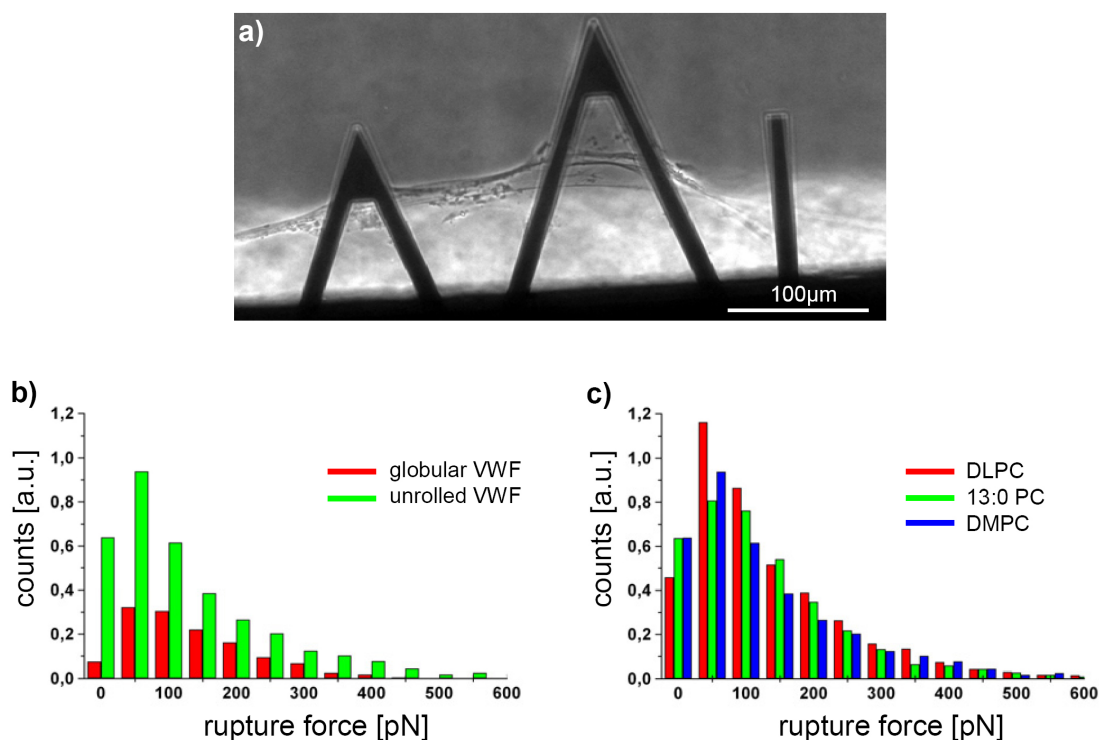


Figure 5.28: a) Mechanical activation of VWF on AFM cantilevers led to the formation of extended network. b) The analysis of globular and unrolled VWF on a DMPC membrane yields a pronounced increase in binding events, whereas the rupture force distributions remain similar. c) The influence of the chain length is negligible in bilayers of DPLC (12:0 PC), 13:0 PC and DMPC (14:0 PC).

ence on VWF-membrane interaction both in the collapsed and the unrolled conformation (figure 5.28 c). Force measurements on fluid 12:0 PC (DLPC), 13:0 PC and 14:0 PC (DMPC) showed almost identical distributions of rupture forces.

Discussion

AFM imaging and AFM Force Spectroscopy indicate a binding mechanism of VWF to phospholipid membranes which depends on the interplay between membrane phase state, membrane defects or domain boundaries and VWF conformation. Single VWF molecules exhibit a distinct preference to the network-like two dimensional "grain boundaries" within the perfectly flat gel-like DSPC bilayer (figure 5.24). Apart from these boundaries almost no adhesion was detected. On the other hand, random adhesion of single molecules occurred in fluid DOPC membranes. Although featuring identical headgroups, AFM Force Spectroscopy exhibited a considerable increase in the rupture forces in fluid compared to gel-like DSPC membranes. A further increase in rupture force is monitored by analysing mixed phospholipid membranes. A dominating electrostatic effect can be excluded by the fact that fluid membranes with both negatively and positively charged lipid doping shift the rupture forces to higher values. Hence, a charge independent binding mechanism governed by lipid phase state and domain boundaries or defects is proposed. Fluid membranes exhibit higher diffusion constants of their constituting phospholipids, higher elasticity and a lower density compared to gel-like membranes [116, 121]. All these properties positively affect the integration of parts of the VWF protein into the membrane. Within a perfectly flat surface of a one component membrane, VWF incorporation may be more difficult than it is in membranes comprising regions of subtle phospholipid mismatch. Such characteristics are found in domain boundaries as well as in mixtures of various different phospholipids (e.g. in real cell walls) [122, 123]. The concept of mismatch in lipid mixtures is able to accurately explain the increase of rupture forces observed for the DOPC-DOPA and DOPC-DOTAP bilayers in AFM Force Spectroscopy. DSPC bilayers also comprise some kind of minute mismatch. Although AFM imaging shows a flat membrane, an in plane displacement with imperfect lipid packing can be assumed by an accumulation of the fluorescence dye within some kind of two dimensional defects (figure 5.24 d, e). While the lipid chain length in pure phospholipid membranes does not seem to affect the binding of VWF, the particular type of membrane defect does. Interaction with hydrophobic DOPC monolayers increased the interaction strength compared to a DOPC bilayer (figure 5.27 c). The membrane defects in DSPC-DOPC or DSPC-DOTAP bilayers in imaging experiments also expose hydrophobic side chains, which enhanced the interaction forces to VWF. Besides the negligible influence of the electric charge located on the phospholipid headgroups, this gives further evidence that single VWF molecules dispose strong interaction with the hydrophobic core of a membrane.

The tight attachment of individual molecules to phospholipid membranes is a prerequisite for the formation of networks with several dozens of μm in size. This led to the concept of anchoring points within the hydrophobic part of the membrane (see chapter 5.2.1), a picture being strongly supported by an increase in rupture forces on hydrophobic mono-

layers. These protein anchors have to adhere tightly enough to the membrane in order to span extended networks and resist their relaxation forces. Mechanical unrolling of VWF increases the contact area of the protein and the membrane and therefore the total interaction force. Our Force Spectroscopy measurements revealed that both the distribution and absolute values of rupture forces in the range of few hundreds of pico-Newton strongly resemble each other in both conformations. Nevertheless, a striking difference is the significant increase of the amount of unbinding events in the activated state. With regard to the VWF multimer composition of up to 100 identical subunits with identical chemical and physical properties, the only possible explanation for this behaviour is a sequential detachment of identical binding sites. This multiple linkage of unrolled and crosslinked VWF molecules most probably enables the formation of anchor points to span macroscopic individual networks. The appearance of the force - distance cycles does not provide additional information on the peculiar type of interaction. Although differences in the amount of binding events can be discriminated, the general shape of the force-curves is similar in each case. It does not display pronounced attractive or repulsive features upon cantilever approach (see also figure 4.3). A common feature is the presence of multiple unbinding events during a single force cycle. Theoretically, only the last rupture event can be clearly assigned to the detachment of the protein from the membrane. The exclusive analysis of the last unbinding yields comparable rupture force distributions as for taking all rupture events into account. Hence, most unbinding events can be assigned to protein detachment from the membrane surface. A "force quantum", i.e. a minimum repetitive rupture force, was not found. The interaction between multiple amino acids and the membrane may be too complex, too numerous or just below force resolution for demonstrating its existence. A deformation of tip bound VWF is not expected since the slope before most rupture events equalled that of the contact line.

The results presented above give strong evidence for a dominating influence of the hydrophobic core of phospholipid membranes on the interaction with VWF. Nevertheless, a bilayer exhibits a chemically complex surface and offers numerous possibilities for non-covalent interactions. These may be dependent on charge, hydrophobicity, polarity and *H*-bonding potential [117] of the membrane and the protein side chains. The side chains of amino acids display preferences for either the hydrophobic part of the membrane, the headgroup region, the headgroup-water interface or just a hydrophilic environment. Furthermore, proteins can find a new thermodynamic energy minimum inside a membrane by changes in their secondary structure. The high energy cost of dehydrating peptides during the transfer into a non-polar phase is reduced by the formation of *H*-bonds in structured elements like α -helices and β -barrels (see also CD data in table 5.2.1 and 5.2.1) [124]. On the other hand, the membrane itself will rearrange in order to minimize the energy of the system [125, 126].

Whatever the actual molecular binding mechanism may look like, VWF may be able to shape fluid membranes more easily than gel-like membranes in a way that optimal protein embedding can be achieved. Grain boundaries in DSPC bilayers provide binding sites for small parts of the VWF molecule, while the intact homogeneous gel-like membrane is too rigid to be manipulated in a way that binding on an extended area is achieved and individual networks can be formed. The fluidity of a membrane in the liquid

phase seems to be the key in this process. Lipid mixtures in biological cell membranes will enhance this effect by providing additional anchor points as a result of phospholipid mismatch within both the hydrophobic chains and headgroup of phospholipids.

6 Summary and Outlook

In recent years, VWF research attracted more and more attention. A possible reason might be the improved knowledge of the correlations between VWF's structure, its mechanical properties [1] and function in wound healing. In this highly interdisciplinary research environment, physicians, chemists, biologists and physicists contribute their part to a better understanding of both functional and pathological forms of VWF. Within this thesis, VWF's potency to unroll and form extended haemostatically active networks as well as its membrane binding potential was approached from a physical perspective. The results presented above will contribute a significant part to the development of specific clinical applications to understand and cure VWF related diseases and stimulate discussions concerning the coupling of mechanic properties and function of polymers in general.

From a medical point of view, the most outstanding finding of the present work may be the elucidation of the strong pH dependence of the critical shear rate for VWF activation. Blood pH is precisely controlled to $pH \approx 7.4$ and any local deviation in the range of ± 0.2 represents pathological conditions. Such a pH drop at a site of vascular injury, under poststenotic conditions, ischaemia or acidosis is a vital parameter to stimulate enhanced and misguided thrombus formation. In physical terms, our unique VWF activity phase diagram summarises the protein's potency to bind platelets as a function of shear stress and local pH . Applying this diagram for medical diagnostics, a physician may be able to estimate the risk of thrombus formation at occluded or pathological altered blood vessels by simple pH and vessel size analysis. The origin of VWF's pH dependent behaviour was found in the three dimensional structure of its amino acids sequence, as it evolved during evolution. The VWF multimer is made up in a way that it exhibits an effective isoelectric point of its native structure exactly at blood pH . Using solubility arguments, it was shown that increasing electrical charging of the protein by any pH change from its effective isoelectric point leads to an enhanced solubility in the medium. This solubility enhancement is accompanied by a decrease of the critical shear rate of the protein. The measurement of the VWF activation as a function of temperature would be an additional benefit for both medicine and physics. While pH is very sensitively controlled in our vascular system, body temperature slightly decreases from the inside to the extremities and, hence, influences VWF activation. The knowledge of the precise temperature and pH dependence of VWF's critical shear rate will enable to calculate the latent heat and heat capacity of VWF's first order phase transition. This will help to specify the interaction potential ΔU , which represents a powerful but heuristic and temperature independent unit so far.

The critical shear rate for VWF activation is diminished in close vicinity to a surface. Hence, instead of uncontrolled thrombus formation in the vessel interior, VWF unrolling

as well as platelets binding occurs preferentially directly at sites of injury at the vessel wall. Furthermore, geometrical constrictions or protruding parts of damaged tissue into the blood stream are able to manipulate the stream lines in a way that particles, e.g. cells or proteins, are locally enriched. In the course of wound healing, such enrichment in combination with a decreased critical shear rate near a surface is a tremendous step towards fast and efficient network formation and wound healing. The analysis of the relaxation behaviour of stretched VWF bundles highlighted the presence of memory effects and a strong internal coupling between single protein fibres inside the networks. Here, a molecule or the peculiar arrangement of molecules within the network, respectively, is significantly influenced by its arrangement at previous times. This strong coupling in both single VWF molecules and networks is mediated by hydrophobic forces. The stability of the VWF molecule against hydrodynamic activation could be tuned by manipulating the polarity of the solvent. This behaviour can be directly related to a change in the effective interaction potential ΔU between the dimeric subunits of the polymer, which retains the molecule in its collapsed conformation. The dimer itself displayed strong susceptibility to hydrodynamic shear forces which led to irreversible changes in the protein's secondary structure. These experiments gave strong evidence that both the treatment of the VWF building blocks as solid bodies and the view of VWF unrolling as being totally reversible is an over-simplification. The role of the dimer in VWF activation as well as in self association is still to be elucidated. The results of this thesis will build the basis for a detailed investigation of structural rearrangements within the dimer and its impact on the interaction potential ΔU and multimer activation upon shear flow. Furthermore, AFM Force Spectroscopy with tip bound dimers will expose interaction forces between collagens, membranes or other dimers immobilized on a surface.

The results of VWF's activation and network formation potential were further applied to the protein's binding potency to platelet and endothelial cells. Using phospholipid model membranes without specific lock and key binding sites, the interaction was reduced to the pure physical contact between membrane and protein. The fluidity of a membrane, minute phospholipid mismatch of phase boundaries and membrane defects were identified as the dominating factors in membrane binding. The membrane environment and especially its hydrophobic core are able to shape VWF structure and exhibit strong adhesive potential. The molecular binding mechanism seems to be independent of the conformation of VWF. AFM Force Spectroscopy measurement proved that the binding forces for globular and elongated VWF fibres comprise identical values. The only and most striking factor is the pronounced enhancement of binding events in the activated protein state which is the requirement for tight adhesion of the protein on the membrane. Although binding to endothelial cells may involve lock and key binding to certain receptor proteins within the cell membrane, they are not essential for network formation on cell surfaces. Nevertheless, a pronounced specificity of VWF - membrane interaction arises from the interplay of various factors. Membrane binding of the VWF protein at a vessel lesion is supported by the influence of a solid wall, which reduces the critical shear rate, possible accumulation effects as a result of stream line modifications, membrane phase state and lipid composition as well as VWF conformation.

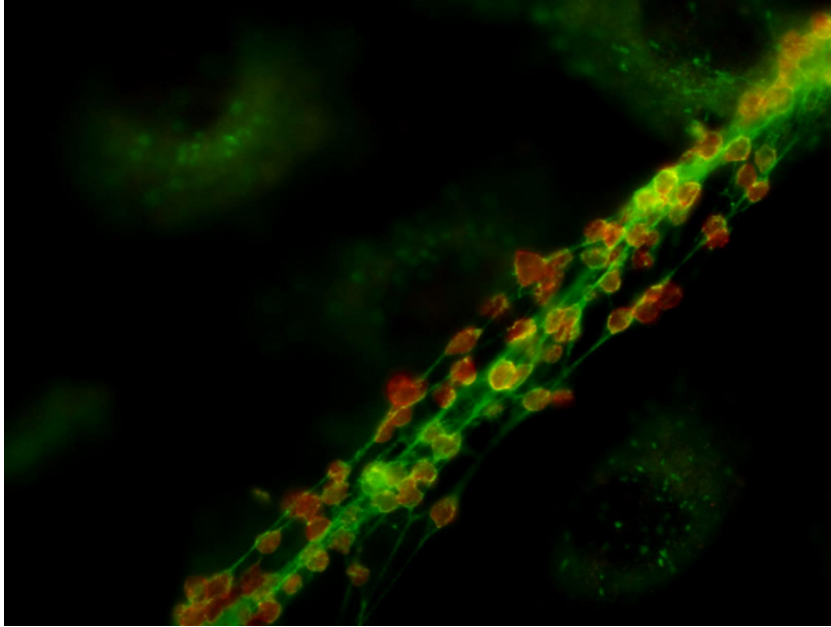


Figure 6.1: The fluorescence image points out the functional activity of stretched VWF (green) in platelet (red) binding. Platelets exhibit sizes in the order of $10\mu m$, which also highlights the enormous size of the VWF network.

From a technological point of view, our newly developed AFM-SAW-hybrid setup combines the benefits of high resolution imaging or the accuracy of AFM force measurements, fluid mechanics and optical accessibility. Apart from mixing and driving the system into equilibrium, an analysis of the effect of shear stress on single cells, platelets or proteins, mimicking blood flow conditions or just adding mechanical forces on the sample is impossible in a common AFM-setup and can be accomplished by this hybrid system.

This thesis provides a first comprehensive physical study of VWF activation, self association and network formation, its dynamics response to mechanical deformations and its solubility dependence. It started to bridge the gap between physics and medicine by emphasising the role of fluid dynamics, macroscopic force fields, interfaces and protein mechanics in blood clotting. The exposure of the connections between molecular origin of VWF activation and its dynamic response to hydrodynamic forces forms a powerful tool for medicine to estimate VWF's binding potency under normal and pathologic blood conditions.

7 Danksagung

Diese Arbeit war in den letzten Jahren nicht nur ein Job für mich, sondern vielmehr eine persönliche Motivation und Aufgabe! Nichtsdestotrotz wäre Vieles ohne die tatkräftige Unterstützung im fachlichen, privaten, freundschaftlichen und familiärem Bereich in diesem Umfang nicht möglich gewesen. An dieser Stelle möchte ich nochmals den Menschen danken, die in irgendeiner Form an der Durchführung und am Abschluss dieser Dissertation beteiligt waren.

Prof. Dr. Achim Wixforth

für die gewährten Freiräume während meiner Arbeit, die stets offene Türe, den enormen Sachverstand, seine Menschenkenntnis und das beispielhafte Führen der Menschen am Lehrstuhl.

Dr. Matthias Schneider

für deine intensive Betreuung in vielerlei Hinsicht zurück bis zur Diplomarbeit, deine mitreißende Begeisterung für biophysikalische Fragestellungen, für die freundschaftliche Atmosphäre bei der Arbeit, im Büro und an so manchen abendlichen Veranstaltungen.

Sidonie Lieber

in deiner Rolle als gute Fee im Labor und bei Fragen zu Chemikalien jeglicher Art, deiner sofortigen Unterstützung bei jedem Problem und noch so kleinem oder großem Problemchen im "forschungsunterstützenden Bereich" [127].

Alexander Hupfer

für deine Dienste am Rechner, die Unterstützung im Labor und außer Haus!

Jennifer Angerer

für deine ansteckend gute Laune, deinen unermüthlichen Eifer, deine Hilfsbereitschaft und deine Freundschaft.

Stefan Bössinger

für deinen Einsatz und deine Motivation während deiner Diplomarbeit und darüber hinaus, deine offene Art, für unsere fachlichen Gespräche in angenehmer Atmosphäre und unsere privaten Gespräche auf persönlicher Ebene, die eigentlich immer auf irgendeine Weise fruchtbar waren und nicht zuletzt auch für deine Freundschaft.

Alfred Grießer

für deine erfrischend trockene Einstellung zu manchen Dingen und deinen Einsatz auch außerhalb der Geschäftszeiten.

Stefan Nuschele

für die Vererbung des Themas und die Beratung und Hilfe bei allen Fragen.

Susanne Braunnüller, Georg Osenstätter, Thomas Franke

Susanne für die Beantwortung aller Fragen mit chemischen Hintergrund; Georg für seine Messungen an der Scherzelle; Thomas für Tipps zu Mikropipetten und Scherzelle.

Jan Opfer, Christian Leirer, Josef Griesbauer, Jürgen Neumann, Babak, Alexander Wolf

für viele Kleinigkeiten, die euch in der Summe doch viel Zeit und Arbeit gekostet haben.

Dr. Stefan Thalhammer (Helmholtz Zentrum München)

für deine nicht selbstverständliche Hilfsbereitschaft auch in schwierigen Zeiten, Ideen und Anregungen für mögliche Messungen und die Korrektur eines Teils dieser Arbeit.

Teresa Neumaier (Helmholtz Zentrum München)

für die Hilfe bei den Messungen mit Mikropipetten und dem Konfokalem Mikroskop und deine einnehmend positive Art.

Prof. Dr. Stefan Schneider (Universität Münster)

und deiner Gruppe für die tatkräftige Unterstützung, sowie die Betrachtung der VWF- Thematik aus medizinischer Sicht. Meine Arbeit wurde durch viele Diskussionen, unterschiedliche und doch sinnverwandte Denkansätze bereichert und gewann darüber hinaus ein "greifbares" Ziel.

Prof. Dr. Peter Hinterdorfer und Dr. Andreas Ebner (Universität Linz)

für die Einführung in die Welt der "Molekül-Zupfer", die andauernde Kooperation und die noch laufenden Messungen.

Andreas Schmid (TU München)

für die Möglichkeit immer wieder am CD Spektrometer zu messen und deine Unterstützung sowohl bei Durchführung der Experimente als auch der Interpretation der Daten.

Vincent Pieribone (Yale University)

für deine tolle Gastfreundschaft während meiner Zeit in den USA und den Einblick in ein "richtiges" Biolabor.

Marie, Kenneth und Vanessa Myles

für die Aufnahme in die Familie während meines Aufenthalts in New Haven inklusive Thanksgiving-Truthahn, Weihnachtsschinken, Pumpkin-Pie und nicht zu vergessen: Pumpkin-Ball!

meinen Eltern Karola und Raimund

für die bedingungslose Unterstützung in jeglicher Hinsicht, den gewährten Freiraum und das Vertrauen in mein Handeln.

Die Liste der Personen und die an sie gerichteten Dankesworte sind bei weitem nicht vollständig. Die freundschaftliche Atmosphäre am Lehrstuhl hat wohl viel dazu beigetragen, dass der Raum 335 regelmäßig nicht nur von 9-17 Uhr belegt war. Ich möchte mich hiermit noch einmal bei allen Mitarbeitern, speziell in der Biophysik, und dem gesamten Team von EP I für die Zusammenarbeit und manche gewachsene Freundschaft bedanken!

A Chemicals, Materials and Procedures

VWF and Buffer

As long as not stated otherwise, all experiments were performed at room temperature in PBS++ buffer containing 140mM NaCl, 10mM KCl, 6,4mM Na₂HPO₄, 2mM KH₂PO₄, 0,1mM CaCl₂ and 1mM MgCl₂. VWF was purchased from Merck Bioscience GmbH (Schwalbach) diluted with double distilled water and stored at -18°C before use. Recombinant VWF was fabricated and kindly provided by the group of Prof. Dr. Schneppenheim (Universitätsklinikum Hamburg) and further purified by Andreas Schmid (TU München).

Phospholipids and Membrane Preparation

To study protein interaction with artificial membranes, the phospholipids DLPC (1,2-Dilauroyl-sn-Glycero-3-Phosphocholine), 13:0 PC (1,2-Ditridecanoyl-sn-Glycero-3-Phosphocholine), DMPC (1,2-Dimyristoyl-sn-Glycero-3-Phosphocholine), 15:0 PC (1,2-Dipentadecanoyl-sn-Glycero-3-Phosphocholine), DSPC (1,2-Distearoyl-sn-Glycero-3-Phosphocholine), DOPC (1,2-Dioleoyl-sn-Glycero-3-Phosphocholine), DOPA (1,2-Dioleoyl-sn-Glycero-3-Phosphate) and DOTAP (1,2-Dioleoyl-3-Trimethylammonium-Propane) were purchased from Avanti Polar Lipids (Al, USA). Lipids were dissolved in pure chloroform and used without further purification. For fluorescence imaging the fluorescence dye Texas-Red coupled to DHPE (1,2-Dihexanoyl-sn-Glycero-3-Phosphoethanolamine) (Invitrogen, Karlsruhe) was incorporated into membrane lipids in dilution (2:1000). Phospholipid membranes were prepared either by spreading vesicles [128] or film balance deposition on a glass support [129]. For AFM experiments glass slides were plasma treated in order to get a molecular clean surface while rinsing with ethanol and water proofed to be sufficient for adhesion experiments.

Immunostaining

For imaging experiments VWF molecules dissolved in PBS++ buffer was added to a reaction chamber including membrane, collagen or bare glass surfaces and kept over night at room temperature. Fluorescence staining of the protein was performed in a two step mechanism including specific antibodies. A primary antibody ($c \approx 3.1 \frac{g}{l}$) was diluted 1:100 in PBS++ buffer and incubated for one hour at room temperature (RT). The secondary antibody ($c \approx 0.81 \frac{g}{l}$) carrying a FITC fluorescence dye was also diluted 1:100 in PBS++ buffer and added to the sample for one hour at RT. Between each step the sample was extensively rinsed with PBS++ buffer. No additional fixative was used. After the staining procedure VWF was analysed using a Zeiss Axiovert 200M fluorescence microscope.

Amino Acids

The 20 proteinogenic amino acids are the building blocks of every protein. The individual sequence and its three dimensional arrangement define the protein's mechanical and chemical properties. Featuring identical backbones, amino acids are discriminated by their side chains R. The following table summarises selected properties of the amino acid's residues [130].

amino acid	residue	polarity	hydrophobicity	acidity/basicity	pK_S
Alanine	$-CH_3$	apolar	1.8	neutral	-
Arginine	$-(CH_2)_3 NH-C(NH)NH_2$	polar	-4.5	basic	12.48
Asparagine	$-CH_2CONH_2$	polar	-3.5	neutral	-
Aspartic acid	$-CH_2COOH$	polar	-3.5	acidic	3.90
Cysteine	$-CH_2SH$	polar	2.5	neutral	8.18
Glutamine	$-(CH_2)_2 CONH_2$	polar	-3.5	neutral	-
Glutamic acid	$-(CH_2)_2 COOH$	polar	-3.5	acidic	4.07
Glycine	$-H$	apolar	-0.4	neutral	-
Histidine	$-CH_2 (C_3H_3N_2)$	polar	-3.2	basic	6.04
Isoleucine	$-CH (CH_3) - CH_2CH_3$	apolar	4.5	neutral	-
Leucine	$-CH_2CH (CH_3)_2$	apolar	3.8	neutral	-
Lysine	$-(CH_2)_4 NH_2$	polar	-3.9	basic	10.54
Methionine	$-(CH_2)_2 SCH_3$	apolar	1.9	neutral	-
Phenylalanine	$-CH_2 (C_6H_5)$	apolar	2.8	neutral	-
Proline	$-(CH_2)_3 -$	apolar	-1.6	neutral	-
Serine	$-CH_2OH$	polar	-0.8	neutral	-
Threonine	$-CH (OH) CH_3$	polar	-0.7	neutral	-
Tryptophan	$-CH_2 (C_8H_6N)$	polar	-0.9	neutral	-
Tyrosine	$-CH_2 (C_6H_4) OH$	polar	-1.3	neutral	10.46
Valine	$-CH (CH_3)_2$	apolar	4.2	neutral	-

Table A.1: The hydrophobicity values are taken from [131].

Amino Acid Sequence of VWF's mature Monomer

SLSCRPPMVKLVCPADNLRAEGLECAKTCQNYDLECMMSGCVSGCLCPPG
MVRHENRCVALERCPCFHQGKEYAPGETVKIGCNTCVCRDRKWNCTDHVC
DATCSTIGMAHYLTFDGLKYLPPGECQYVLVQDYCGSNPGTFRILVGNKG
CSPHSVKCKKRVTILVEGGEIELFDGEVNVKRPMKDETHFEVVESGRYII
LLGKALSVVWDRHLSISVVLKQTYQEKVCGLCGNFDGIQNNDLTSSNLQ
VEEDPVDFGNSWKVSSQCADTRKVPLDSSPATCHNNIMKQTMVDSSCRIL

TSDVFQDCNKLVDPPEPYLDVCIYDTCSCESIGDCACFCDTIAAYAHVCAQ
HGKVVWRTATLCPQSCEERNLRENGYECEWRYNSCAPACQVTCQHPEPL
ACPVQCVEGCHAHCPPGKILDELLQTCVDPEDCPVCEVAGRRFASGKKVT
LNPSDPEHCQICHCDVNNLTCEACQEPGGLVVPPTDAPVSPTTLYVEDIS
EPPLHDFYCSRLDLVFLLDGSSRLSEAEFEVLKAFVVDMMERLRISQKW
VRVAVVEYHDGSHAYIGLKDRKRPSSELRRIASQVKYAGSQVASTSEVLKY
TLFQIFSKIDRPEASRIALLMASQEPQRMSRNFVRYVQGLKKKKVIVIP
VGIGPHANLKQIRLIEKQAPENKAFVLSSVDELEQQRDEIVSYLCDLAPE
APPTLPPDMAQVTVGPGLLGVSTLGPKRNSMVLDAFVLEGSDDKIGEAD
FNRSKEFMEEVIQRMDVGQDSIHVTVLQYSYMTVEYPFSEAQSKGDILQ
RVREIRYQGGNRTNTGLALRYLSDHSFLVSQGDREQAPNLVYMVTGNPAS
DEIKRLPGDIQVVPVIGVGNANVQELERIGWPNAPILIQDFETLPREAPD
LVLQRCCSGEGLQIPTLSPAPDCSQPLDVILLDDGSSSFASYFDEMKSF
AKAFISKANIGPRLTQVSVLQYGSITTIDVPWNVVPPEKAHLLSLVDVMQR
EGGPSQIGDALGFAVRYLTSEMHGARPGASKAVVILVTDVSVDSVDAAD
AARSNRVTVFPIGIGDRYDAAQLRILAGPAGDSNVVVKLQRIEDLPTMVTL
GNSFLHKLCSGFVRCMDEDGNEKRPGDVWTLQDQCHTVTCQPDGQTLK
SHRVNCDRGLRPSCPNSQSPVKVEETCGCRWTCPCVCTGSSTRHIVTFDG
QNFKLTGSCSYVLFQNKEDLEVLHNGACSPGARQGCMSIEVKHSALS
VELHSDMEVTVNGRLVSVPYVGGNMEVNVYGAIMHEVRFNHLGHIFTFTP
QNEFQLQLSPKTFASKTYGLCGICDENANDFMLRDGTVTTDWKTIVQE
WTVQRPGQTCQPILEEQCLVPDSSHCQVLLLPLFAECHKVLAPATFYAIC
QQDSCHQEQVCEVIASIAHLCRTNGVCVDWRTPDFCAMSCPPSLVYNHCE
HGCPRHCDGNVSSCGDHPSEGCFPPDKVMLEGSCVPEEACTQCIGEDGV
QHGFLEAWVPDHQPCQICTCLSGRKNCTTQPCPTAKAPTCLCEVARLR
QNADQCCPEYECVCDPVSCDLPPVPHCERGLQPTLTNPGECPNFTCACR
KEECKRVSPSPCPHRLPTLRKTQCCDEYECACNCVNSTVSCPLGYLAST
ATNDCGCTTTTCLPPDKVCVHRSTIYPVGQFWEEGCDVCTCTDEDAMGL
RVAQCSQKPCEDSCRSGFTYVLHEGECCGRCLPSACEVVTGSPRGDSQSS
WKSQVGSQWASPENPCLINECVRVKKEEVFIQQRNVSCPLEVPPVCPSPGFQL
SCKTSACCPSRCRERMEACMLNGTVIGPGKTMIDVCTTCRCMVQVGVIS
GFKLECRKTTNCPCPLGYKEENNTGECCGRCLPTACTIQLRGGQIMTLKR
DETLQDGDTHFCKVNERGEYFWEKRVTCPPFDEHKCLAEGGKIMKIPG
TCCDTCEEPECNDITARLQYVKVGSCKSEVEVDIHYCQGKASKAMYSID
INDVQDQCSCCSPTRTEPMQVALHCTNGSVVYHEVLNAMECKCSPRKCSK

These 2050 amino acids add up to 105 Alanine (A), 101 Arginine (R), 74 Asparagine (N), 13 Aspartic acid (D), 169 Cysteine (C), 99 Glutamine (Q), 137 Glutamic acid (E), 137 Glycine (G), 52 Histidine (H), 78 Isoleucine (I), 156 Leucine (L), 88 Lysine (K), 40 Methionine (M), 55 Phenylalanine (F), 139 Proline (P), 141 Serine (S), 115 Threonine (T), 18 Tryptophan (W), 49 Tyrosine (Y) and 184 Valine (V) [14].

AFM Imaging and Force Spectroscopy

AFM imaging experiments in fluids were performed in intermittent contact mode with CSC37/noAl cantilever chips from Mikromash (Tallinn, Estonia). Cantilever arms A and C with resonance frequencies of 41 and 28kHz and force constants 0.65 and 0.35 $\frac{N}{m}$ according to manufacturer information were commonly used. The resonance peak must be well shaped and high enough above background noise. Possible reasons for badly shaped resonance curves is adsorbed dirt on the cantilever, physical damage, improper fixation of the cantilever chip or contact of the cantilever to the sample surface. Cantilevers with a bad resonance curve have to be replaced. Typical oscillation amplitudes are in the order of 100 to 200nm. The parameters for imaging have to be set individually according to sample height, sample elasticity and scan area.

For improved force resolution in AFM Force Spectroscopy measurements, soft MSCT-AUNM cantilever chips were purchased from Veeco (Dourdan, France). Cantilever C with a force constant of 0.01 $\frac{N}{m}$ were used exclusively. The following protocol was applied for coating cantilevers with VWF molecules:

1. 3.3mg ethanolamine powder is dissolved in 6ml DMSO at 60°C and given into a beaker with mol-sieve (pores $\approx 0.4nm$).
2. The ethanolamin solution is given into an exiccator for several minutes to reduce the gas concentration in the fluid.
3. Chloroform cleaned cantilever chips are given on a glas slide into the solution and incubate over night.
4. Cantilever chips are extensively washed with DMSO and ethanol and dried under a gentle nitrogen flow.
5. Cantilever chips are incubated for two hours in a solution containing 25mg EGS, 25ml Chloroform and 125 μ l Triethylamine.
6. Cantilever chips are extensively washed with cloroform and dried under a gentle nitrogen flow.
7. Cantilever chips are incubated for two hours in a VWF solution ($c \approx 0.25 \frac{mg}{ml}$).
8. Cantilever chips are extensively washed with PBS++.
9. Cantilever chips are incubated for one hour in hydroxylamine solution in PBS++ ($c \approx 16mM$).
10. Cantilever chips are extensively washed with PBS++ and stored in PBS++ up to several hour before use.

B Phospholipid Membranes

Phospholipids are the main constituents of biological membranes. They comprise an amphiphilic structure of two hydrophobic fatty acid chains and a hydrophilic head group. Different phospholipids may vary in both the length of their fatty acid chains, the amount of double bonds within these chains and their headgroup composition. The amphiphilic design significantly influences its behaviour in a water environment. Hereby, the interaction energy and solubility of phospholipids is primarily determined by the length of its hydrophobic tails, which induce water ordering accompanied with an entropy reduction. In order to minimize the total energy of the system, phospholipids tend to form micells or bilayer membranes where the contact of water molecules and fatty acid chains is reduced to almost zero and the hydrophilic headgroups tend towards the water (figure B.1) [132].

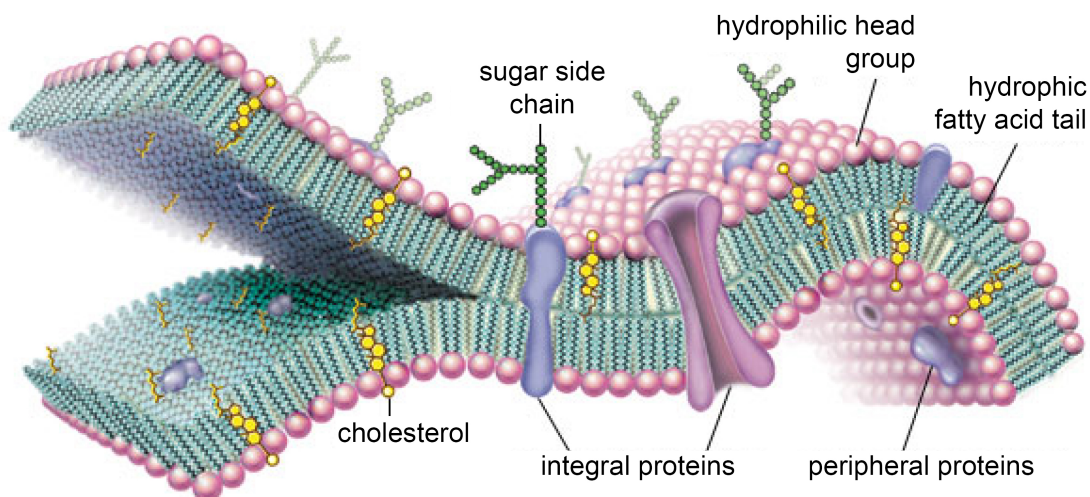


Figure B.1: Real cell membranes consist of a variety of proteins, sugars, etc. which are embedded in a matrix of phospholipids. Phospholipids form bilayer structures in a water environment with their hydrophilic headgroups at the interface between the water and the hydrophobic membrane core.

Phospholipid membranes comprise different phases with different physical properties dependent on external parameters like temperature, pressure or pH . Biological relevant are the fluid and gel-like phase as well as the phase transition between these phases. Whereas fluid membranes exhibit a unordered conformation, high lateral diffusion constants and

elasticity, gel-like membranes are more densely packed, feature lower compressibility and an ordered structure. During the phase transition of first order from the gel-like to the fluid phase (main transition), membrane parameters like isothermal compressibility, isobaric heat capacity or area expansion coefficient display pronounced maxima [109].

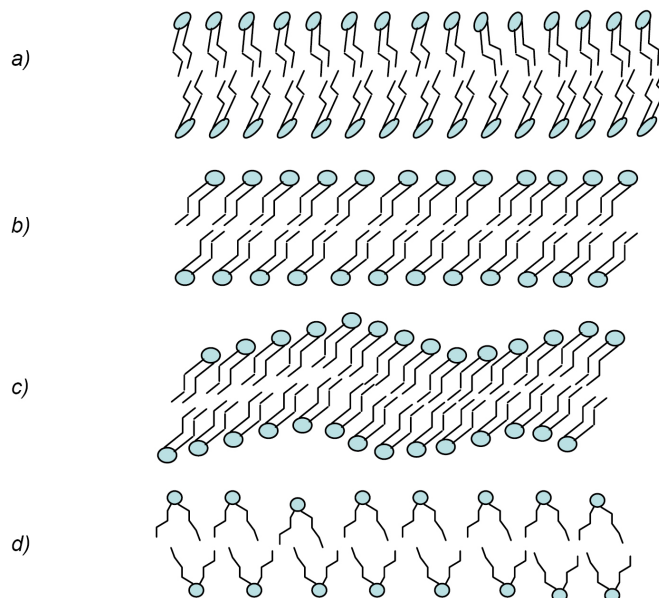


Figure B.2: a) In a high pressure or low temperature regime, the phospholipids inside a bilayer are ordered perpendicular to the membrane plane in the so called solid phase. b) With increasing temperature, the phospholipids start to tilt into the gel-like state until an angle of approximately 30° is reached. c) In between the gel-like and the d) fluid phase, a so called ripple phase may exist [133]. Whereas the transition from the solid into the gel-like phase can be described by a phase transition of second order, the transformation from gel-like to fluid phase is of first order.

C Interaction Forces

Electrostatic Interaction Forces

The selection of interaction forces in the theory part of this thesis is limited to van der Waals dipole - dipole interactions. In table C some more interaction potentials with electrostatic origin are illustrated. In this regard, an interesting aspect is the different scaling of several interactions with the distance r when Brownian motion is considered. A demonstrative example for this behaviour is given by the interaction of an ion with a dipole. The energy W of a permanent dipole $\vec{\mu}$ in an electric field E is given by

$$W = -\mu \cdot E \cdot \cos\Theta \quad (\text{C.1})$$

Θ is the angle between the connecting line of the dipole and the centre of the electric charge and the direction of the dipole moment. Inserting the electric field of a single point charge q yields an $W \propto \frac{1}{r^2}$ decay

$$W = -\frac{\mu \cdot q \cdot \cos\Theta}{4\pi \cdot \epsilon_0 \cdot r^2} \quad (\text{C.2})$$

When Brownian motion is also taken into account, the dipole is permanently pushed out of its equilibrium state and all orientations Θ are possible. The statistical weight of each orientation is given by a Boltzmann distribution:

$$\exp\left(-\frac{W}{k_B T}\right) = \exp\left(-\frac{\mu \cdot E \cdot \cos\Theta}{k_B T}\right) \quad (\text{C.3})$$

For $\mu \cdot E \cdot \cos\Theta \ll k_B T$, the mean value of $\vec{\mu}$ can be derived according to

$$\langle \vec{\mu} \rangle = \frac{p^2 \cdot E}{3 \cdot k_B T} \quad (\text{C.4})$$

Hence, the mean energy of a dipole in an electric field of a point charge becomes

$$W = -\langle \vec{\mu} \cdot \vec{E} \rangle = -\frac{p^2 \cdot E^2}{3 \cdot k_B T \cdot r^4} \quad (\text{C.5})$$

with an $W \propto \frac{1}{r^4}$ decay.

Van der Waals Interaction of Macroscopic Bodies

So far, the treatment of the van der Waals potential was limited to the interaction between two atoms or molecules. In order to generalize these considerations from a two particle problem to complex macroscopic systems, the sum over all atoms or molecules

Kind of Interaction	Potential without Brownian Motion	Potential with Brownian Motion
Ion - Ion	$C \cdot \frac{q_1 \cdot q_2}{r}$	$C \cdot \frac{q_1 \cdot q_2}{r}$
Ion - Permanent Dipole	$C \cdot \frac{\mu \cdot q \cdot \cos\Theta}{r^2}$	$C \cdot \frac{\mu^2 \cdot q^2}{4 \cdot k_B T \cdot r^4}$
Permanent Dipole - Permanent Dipole	$C \cdot \frac{\mu_1 \cdot \mu_2 \cdot K}{r^3}$	$C^2 \cdot \frac{2 \cdot \mu_1^2 \cdot \mu_2^2}{3 \cdot k_B T \cdot r^6}$
Ion - Molecule	$-C^2 \cdot \epsilon_0 \cdot \frac{\alpha \cdot q^2}{2 \cdot r^4}$	$-C^2 \cdot \epsilon_0 \cdot \frac{\alpha \cdot q^2}{2 \cdot r^4}$
Permanent Dipole - Molecule	$-C^2 \cdot \epsilon_0 \cdot \frac{\alpha \cdot (3 \cdot \cos\Theta + 1) \cdot \mu_0^2}{2 \cdot r^6}$	$-C^2 \cdot \epsilon_0 \cdot \frac{\alpha \cdot \mu_0^2}{r^6}$
Induced Dipole - Induced Dipole	$-C^2 \cdot \frac{3 \cdot I_1 \cdot I_2 \cdot \alpha_1 \cdot \alpha_2}{2 \cdot (I_1 + I_2) r^6}$	$-C^2 \cdot \frac{3 \cdot I_1 \cdot I_2 \cdot \alpha_1 \cdot \alpha_2}{2 \cdot (I_1 + I_2) r^6}$

Table C.1: Various interaction of electrostatic origin are summarized as a function of their separation r . Herein, the constant C is given by $C = \frac{1}{4\pi \cdot \epsilon_0}$, q is the electric charge, μ the dipole moment, k_B the Boltzmann constant, T the absolute temperature, α the polarizability, I the ionisation energy and K a constant which depends on the mutual orientation of the interacting dipoles. Taking Brownian motion into account, the distance relations change as depicted above.

of both bodies interacting with each other has to be estimated. Although the origin of the interaction between macroscopic structures is still dipoles, the resulting energies and forces depend strongly on the geometry of the bodies. In particular, the characteristic $V \propto -\frac{1}{r^6}$ behaviour of the vdW potential between two bodies can be lost. Figure C.1 exemplifies the vdW interaction potentials of several macroscopic bodies as a function of their separation distance [36].

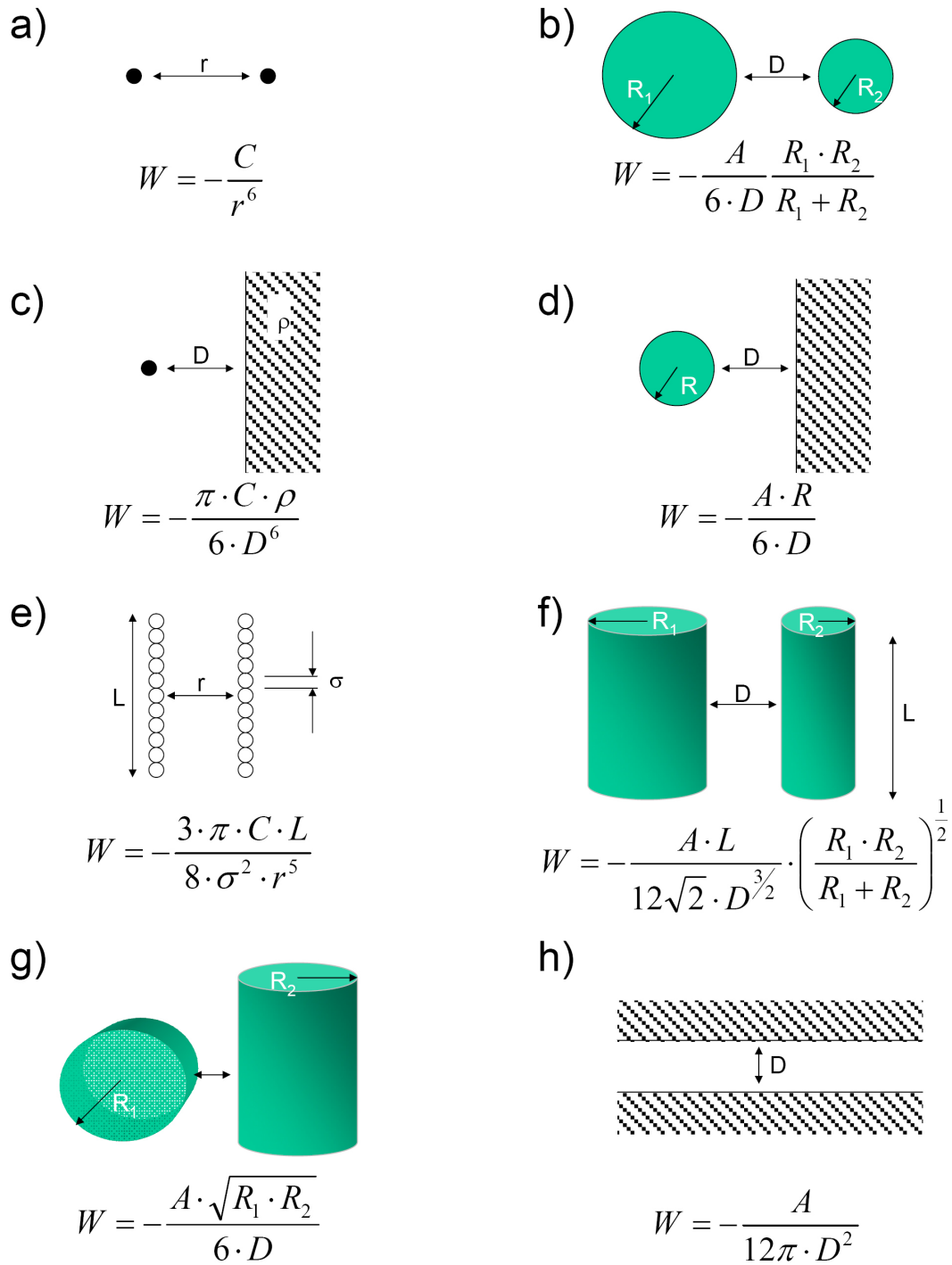


Figure C.1: a) The vdW potential W between two atoms comprises the well known $V \propto -\frac{1}{r^6}$ decay (C is the constant derived from Keesom, Debye and London-dispersion contributions) with distance r and changes into b) an $V \propto -\frac{1}{D}$ behaviour when considering two macroscopic spheres. The density ρ of the spheres is included in the Hamaker constant A . The following vdW potentials display the interaction energies between c) atom - surface, d) sphere - surface, e) two parallel chain molecules, f) two cylinders, g) two crossed cylinders and h) two extended surfaces (potential per unit area).

References

- [1] S. W. Schneider, S. Nuschele, A. Wixforth, C. Gorzelanny, A. Alexander-Katz, R. R. Netz, and M. F. Schneider. Shear-induced unfolding triggers adhesion of von Willebrand factor fibers. *Proc. Nat. Acad. Sci.*, 104:7899–7903, 2007.
- [2] A. Alexander-Katz, M. F. Schneider, S. W. Schneider, A. Wixforth, and R. R. Netz. Shear-flow-induced unfolding of polymeric globules. *Phys. Rev. Lett.*, 97(13):138101, 2006.
- [3] C. E. Mortimer. *Chemie*. Georg Thieme Verlag, 1996, ISBN-3-13-484306-4.
- [4] D. J. Voet, J. G. Voet, C. W. Pratt, and U. Hahn. *Lehrbuch der Biochemie*. Wiley-VCH, 2002, ISBN-3-527-30519-x.
- [5] H. R. Christen and G. Meyer. *Grundlagen der organischen Chemie*. Salle Verlag, 1996, ISBN-978-3793554936.
- [6] W. G. J. Hol, P. T. van Duijnen, and H. J. C. Berendsen. The α -helix dipole and the properties of proteins. *Nature*, 273:443–446, 1978.
- [7] B. Odaert, F. Jean, C. Boutillon, E. Buisine, O. Melnyk, A. Tartar, and G. Lippens. Synthesis, folding, and structure of the [bgr]-turn mimic modified b1 domain of streptococcal protein g. *Protein Sci.*, 8:2773–2783, 1999.
- [8] G. D. Rose, L. M. Gierasch, and J. A. Smith. Turns in peptides and proteins. *Adv. Protein Chem.*, 37:1–109, 1985.
- [9] P. E. Wright and H. J. Dyson. Intrinsically unstructured proteins: re-assessing the protein structure-function paradigm. *J. Mol. Biol.*, 22:321–31, 1999.
- [10] O. Yifrach and A. Horovitz. Coupling between protein folding and allostery in the GroE chaperonin system. *Proc. Nat. Acad. Sci.*, 97(4):1521–1524, 2000.
- [11] V. V. Mozhaev, K. Heremans, J. Frank, P. Masson, and C. Balny. High pressure effects on protein structure and function. *Protein Sci.*, 24(1):81–91, 1996.
- [12] C. J. Tsai, S. L. Lin, H. J. Wolfson, and R. Nussinov. Studies of protein-protein interfaces: A statistical analysis of the hydrophobic effect. *Protein Sci.*, 6(1):53–64, 1997.

- [13] A. Onufriev, D. A. Case, and G. M. Ullmann. A novel view of pH titration in biomolecules. *Biochemistry*, 40(12):3413–3419, 2001.
- [14] D. J. Mancuso, E.A. Tuley, L. A. Westfield, N. K. Worrall, B. B. Shelton-Inloes, J. M. Sorace, Y. G. Alevy, and J. E. Sadler. Structure of the gene for human von Willebrand factor. *J. Biol. Chem.*, 264(33):19514–19527, 1989.
- [15] J. E. Sadler. Biochemistry and genetics of von willebrand factor. *Annu. Rev. Biochem.*, 67(1):395–424, 1998.
- [16] D. D. Wagner, T. Mayadas, and V. J. Marder. Initial glycosylation and acidic pH in the Golgi apparatus are required for multimerization of von Willebrand factor. *J. Cell Biol.*, 102(4):1320–1324, 1986.
- [17] T. N. Mayadas and D. D. Wagner. In vitro multimerization of von Willebrand factor is triggered by low pH. Importance of the propolypeptide and free sulfhydryls. *J. Biol. Chem.*, 264(23):13497–13503, 1989.
- [18] C. L. Verweij, M. Hart, and H. Pannekoek. Expression of variant von willebrand factor (vwf) cDNA in heterologous cells: requirement of the pro-polypeptide in vwf multimer formation. *EMBO J.*, 6(10):2885–2890, 1987.
- [19] D. D. Wagner, J. B. Olmsted, and V. J. Marder. Immunolocalization of von Willebrand protein in Weibel-Palade bodies of human endothelial cells. *J. Cell Biol.*, 95(1):355–360, 1982.
- [20] L. A. Sporn, V. J. Marder, and D. D. Wagner. Inducible secretion of large, biologically potent von willebrand factor multimers. *Cell*, 46(2):185–90, 1986.
- [21] J. Perkkioe, L. J. Wurzinger, and H. Schmid-Schönbein. Plasma and platelet skimming at t-junctions. *Thromb. Res.*, 45(5):517–526, 1987.
- [22] Z. M. Ruggeri. von willebrand factor. *J. Clin. Invest.*, 99(4):559–564, 1997.
- [23] A. J. Reininger, H. F. G. Heijnen, H. Schumann, Ha. M. Specht, W. Schramm, and Z. M. Ruggeri. Mechanism of platelet adhesion to von Willebrand factor and microparticle formation under high shear stress. *Blood*, 107(9):3537–3545, 2006.
- [24] S.M. Dopheide, M. J. Maxwell, and S. P. Jackson. Shear-dependent tether formation during platelet translocation on von Willebrand factor. *Blood*, 99(1):159–167, 2002.
- [25] A. C. Guyton and J. E. Hall. *Textbook of medical physiology*. W.B.Saunders, 2000, ISBN-978-0721602400.
- [26] J. Dong, J. L. Moake, L. Nolasco, A. Bernardo, W. Arceneaux, C. N. Shrimpton, A. J. Schade, L. V. McIntire, K. Fujikawa, and J. A. Lopez. ADAMTS-13 rapidly cleaves newly secreted ultralarge von Willebrand factor multimers on the endothelial surface under flowing conditions. *Blood*, 100(12):4033–4039, 2002.

- [27] H. M. Tsai. Physiologic cleavage of von Willebrand factor by a plasma protease is dependent on its conformation and requires calcium ion. *Blood*, 87(10):4235–4244, 1996.
- [28] H. M. Tsai, I. I. Sussman, and R. L. Nagel. Shear stress enhances the proteolysis of von Willebrand factor in normal plasma. *Blood*, 83(8):2171–2179, 1994.
- [29] L. Holmberg and I. M. Nilsson. Von Willebrand disease. *Clin. Haematol.*, 14(2):461–88, 1985.
- [30] F. Rodeghiero, G. Castaman, and E. Dini. Epidemiological investigation of the prevalence of von Willebrand’s disease. *Blood*, 69(2):454–459, 1987.
- [31] R. Schneppenheim and U. Budde. *Das von Willebrand-Syndrom und von Willebrand-Faktor: Aktuelle Aspekte der Diagnostik und Therapie*. Uni-Med Verlag, 2006, ISBN-389599989X.
- [32] G. J. Tangelder, D. W. Slaaf, T. Arts, and R. S. Reneman. Wall shear rate in arterioles in vivo: least estimates from platelet velocity profiles. *Am. J. Physiol. Heart Circ. Physiol.*, 254(6):H1059–1064, 1988.
- [33] M. F., Z. Guttenberg, S. W. Schneider, K. Sritharan, V. M. Myles, U. Pamukci, and A. Wixforth. An Acoustically Driven Microliter Flow Chamber on a Chip (muFCC) for Cell-Cell and Cell-Surface Interaction Studies. *ChemPhysChem*, 9(4):641–645, 2008.
- [34] I. Singh, H. Shankaran, M. E. Beauharnois, Z. Xiao, P. Alexandridis, and S. Neelamegham. Solution Structure of Human von Willebrand Factor Studied Using Small Angle Neutron Scattering. *J. Biol. Chem.*, 281(50):38266–38275, 2006.
- [35] P. Atkins and R. Friedman. *Molecular Quantum Mechanics*. Oxford University Press, 2005, ISBN-0199274983.
- [36] J. N. Israelachvili. *Intermolecular and Surface Forces*. Academic Press, 1985, ISBN-0-12-375181-0.
- [37] D. Sarid. *Scanning Force Microscopy: With Applications to Electric, Magnetic, and Atomic Forces: With Applications to Electric, Magnetic and Atomic Forces*. Oxford University Press, 1994, ISBN-019509204X.
- [38] M. D. Joeston and L. Schaad. *Hydrogen Bonding*. Marcel Dekker Ltd, 1974, ISBN-0824762118.
- [39] H. S. Frank and W. Y. Wen. Ion-Solvent Interaction III. Structural Aspects of Ion-Solvent Interaction in aqueous Solutions: A suggested Picture of Water Structure. *Discussions Faraday Soc.*, 24:133–140, 1957.

- [40] Ge. Némethy and H. A. Scheraga. Structure of water and hydrophobic bonding in proteins. i. a model for the thermodynamic properties of liquid water. *J. Chem. Phys.*, 36(12):3382–3400, 1962.
- [41] B. Hribar, N. T. Southall, V. Vlachy, and K. A. Dill. How ions affect the structure of water. *J. Am. Chem. Soc.*, 124(41):12302–12311, 2002.
- [42] K. A. Dill, T. M. Truskett, V. Vlachy, and B. Hribar-Lee. Modelling water, the hydrophobic effect, and ion solvation. *Annu. Rev. Biophys. Biomol. Struct.*, 34(1):173–199, 2005.
- [43] A. Ben-Naim. Statistical mechanics of “waterlike” particles in two dimensions. i. physical model and application of the percus–yevick equation. *J. Chem. Phys.*, 54(9):3682–3695, 1971.
- [44] D. Chandler. Interfaces and the driving force of hydrophobic assembly. *Nature*, 437:640–647, 2005.
- [45] J. A. Schellman. Temperature, stability, and the hydrophobic interaction. *Biophys. J.*, 73(6):2960–2964, 1997.
- [46] K. Shinoda. ”iceberg” formation and solubility. *J. Phys. Chem.*, 81(13):1300–1302, 1977.
- [47] A. L. Weisenhorn, P. Maivald, H. J. Butt, and P. K. Hansma. Measuring adhesion, attraction, and repulsion between surfaces in liquids with an atomic-force microscope. *Phys. Rev. B*, 45(19):11226–11232, 1992.
- [48] R. C. Barrett and C. F. Quate. Charge storage in a nitride-oxide-silicon medium by scanning capacitance microscopy. *J. Appl. Phys.*, 70(5):2725–2733, 1991.
- [49] H. J. Butt. Measuring electrostatic, van der Waals, and hydration forces in electrolyte solutions with an atomic force microscope. *Biophys. J.*, 60(6):1438–1444, 1991.
- [50] S. N. Maganov and M. H. Whangbo. *Surface analysis with STM and AFM*. Wiley-VCH, 1996, ISBN-3527293132.
- [51] Y. Rabinovich. Interaction of hydrophobized filaments in aqueous electrolyte solutions. *Prog. Surf. Sci.*, 40:434–442, 1992.
- [52] G. Binnig, C. F. Quate, and C. Gerber. Atomic force microscope. *Phys. Rev. Lett.*, 56:930–933, 1986.
- [53] C. Thelander and L. Samuelson. AFM manipulation of carbon nanotubes: realization of ultra-fine nanoelectrodes. *Nanotechnology*, 13:108–113, 2002.
- [54] D. Fotiadis, S. Scheuring, S. A. Muller, A. Engel, and D. J. Muller. Imaging and manipulation of biological structures with the afm. *Micron*, 33, 2002.

- [55] G. L. Hornyak, J. Dutta, and H. F. Tibbals. *Introduction to Nanoscience*. Crc Pr Inc, 2008, ISBN-1420048058.
- [56] J. Opfer. *Diplomarbeit: Untersuchung kraftinduzierter Veränderungen des von-Willebrand-Factors*. Universität Augsburg, 2007.
- [57] M. Carrion-Vazquez, A. F. Oberhauser, T. E. Fisher, P. E. Marszalek, and H. Li and J. M. Fernandez. Mechanical design of proteins studied by single-molecule force spectroscopy and protein engineering. *Prog. Biophys. Mol. Biol.*, 74:63–91(29), 2000.
- [58] B. Cappella and G. Dietler. Force-distance curves by atomic force microscopy. *Surf. Sci. Rep.*, 34:5–104(100), 1999.
- [59] A. M. Freitas and M. M. Sharma. Detachment of particles from surfaces: An afm study. *J. Colloid Interface Sci.*, 233, 2001.
- [60] H. Li, A. F. Oberhauser, S. B. Fowler, J. Clarke, and J. M. Fernandez. Atomic force microscopy reveals the mechanical design of a modular protein. *Proc. Nat. Acad. Sci.*, 97:6527–6531, 2000.
- [61] T. Strunz, K. Oroszlan, R. Schafer, and H. J. Guntherodt. Dynamic Force Spectroscopy of Single DNA Molecules. *Proc. Nat. Acad. Sci.*, 96:11277–11282, 1999.
- [62] J. Zlatanova, S. M. Lindsay, and S. H. Leuba. Single molecule force spectroscopy in biology using the atomic force microscope. *Prog. Biophys. Mol. Biol.*, 74:37–61, 2000.
- [63] K. Feldman, T. Tervoort, P. Smith, and N. D. Spencer. Toward a force spectroscopy of polymer surfaces. *Langmuir*, 14(2):372–378, 1998.
- [64] M. Gad, A. Itoh, and A. Ikai. Mapping cell wall polysaccharides of living microbial cells using atomic force microscopy. *Cell Biol. Int.*, 21, 1997.
- [65] A. Raab, W. Han, D. Badt, S. J. Smith-Gill, S. M. Lindsay, H. Schindler, and P. Hinterdorfer. Antibody recognition imaging by force microscopy. *Nat. Biotechnol.*, 17:901–905, 1999.
- [66] JPK. *The Nanowizard AFM Handbook, Version 1.3*. 2005.
- [67] N. Lion, T. C. Rohner, L. Dayon, I. L. Arnaud, E. Damoc, N. Youhnovski, Z. Y. Wu, C. Roussel, J. Jossierand, H. Jensen, J. S. Rossier, M. Przybylski, and H. H. Girault. Microfluidic systems in proteomics. *Electrophoresis*, 24(21):3533–3562, 2003.
- [68] A. Heydorn, B. K. Ersbøll, M. Hentzer, M. R. Parsek, M. Givskov, and S. Molin. Experimental reproducibility in flow-chamber biofilms. *Microbiology*, 146(10):2409–2415, 2000.

- [69] J. A. Frangos, S. G. Eskin, L. V. McIntire, and C. L. Ives. Flow Effects on Prostacyclin Production by Cultured Human Endothelial Cells. *Science*, 227:1477–1479, 1985.
- [70] C. J. Strobl. *Dissertation: Mikro- und Nanofluidik auf piezoelektrischen Substraten*. LMU München, 2005.
- [71] M. F. Schneider, Z. Guttenberg, S. W. Schneider, K. Sritharan, V. M. Myles, U. Pamukci, and A. Wixforth. An acoustically driven microliter flow chamber on a chip (mufcc) for cell-cell and cell-surface interaction studies. *ChemPhysChem*, 9(4):641–645, 2008.
- [72] T. Uchida, T. Suzuki, and S. Shiokawa. Investigation of acoustic streaming excited by surface acoustic waves. *IEEE*, 2:1081–1084, 1995.
- [73] A. Wixforth, C. J. Strobl, C. Gauer, A. Toegl, J. Scriba, and Z. Guttenberg. Acoustic manipulation of small droplets. *Anal. Bioanal. Chem.*, 379:982–991, 2004.
- [74] A. Wixforth. Acoustically driven programmable microfluidics for biological and chemical applications. *JALA*, 11(6):399–405, 2006.
- [75] D. M. Steppich, J. I. Angerer, K. Sritharan, S. W. Schneider, S. Thalhammer, A. Wixforth, A. Alexander-Katz, and M. F. Schneider. Relaxation of ultralarge VWF bundles in a microfluidic-AFM hybrid reactor. *Biochem. Biophys. Res. Commun.*, 369(2):507–12, 2008.
- [76] T. Frommelt. *Dissertation: Mischen und Sortieren mit SAW-Fluidik in Simulation und Experiment*. Universität Augsburg, 2008.
- [77] T. Frommelt, M. Kostur, M. Wenzel-Schäfer, P. Talkner, P. Hänggi, and A. Wixforth. Microfluidic Mixing via Acoustically Driven Chaotic Advection. *Physical Review Letters*, 100(3):034502–+, 2008.
- [78] A. Alexander-Katz and R. R. Netz. Surface-enhanced unfolding of collapsed polymers in shear flow. *Europhys. Lett.*, 80(1):18001 (6pp), 2007.
- [79] W. Demtröder. *Experimentalphysik 1. Mechanik und Wärme*. Springer-Verlag GmbH, 2005, ISBN-354026034X.
- [80] M. Felten, W. Staroske, M. S. Jaeger, P. Schwille, and C. Duschl. Accumulation and filtering of nanoparticles in microchannels using electrohydrodynamically induced vortical flows. *Electrophoresis*, 29(14):2987–2996, 2008.
- [81] T. T. Perkins, D. E. Smith, and S. Chu. Single Polymer Dynamics in an Elongational Flow. *Science*, 276(5321):2016–2021, 1997.
- [82] J. C. Phillips. Stretched exponential relaxation in molecular and electronic glasses. *Rep. Prog. Phys.*, 59(9):1133–1207, 1996.

- [83] M. K. Hong, O. Narayan, R. E. Goldstein, E. Shyamsunder, R. H. Austin, D. S. Fisher, and M. Hogan. Internal dynamics of dna probed by transient electric birefringence. *Phys. Rev. Lett.*, 68(9):1430–1433, 1992.
- [84] S. J. and W. A. Eaton. Nonexponential structural relaxations in proteins. *J. Chem. Phys.*, 104(9):3395, 1996.
- [85] B. J. Cherayil. Stretched exponential relaxation in polymer dynamics. *J. Chem. Phys.*, 97(3):2090–2094, 1992.
- [86] T. Frisch and A. Verga. Unwinding globules under tension and polymer collapse. *Phys. Rev. E*, 65(4), 1992.
- [87] C. N. Pace. Contribution of the hydrophobic effect to globular protein stability. *J. Mol. Biol.*, 226:29–35, 1992.
- [88] R. S. Spolar, J. H. Ha, and M. T. Record. Hydrophobic effect in protein folding and other noncovalent processes involving proteins. *Proc. Nat. Acad. Sci.*, 86(21):8382–8385, 1989.
- [89] R. Breslow. Hydrophobic Effects on simple Organic Reactions in Water. *Acc. Chem. Res.*, 24(6):159–164, 1991.
- [90] Y. Nozaki and C. Tanford. The Solubility of Amino Acids and Two Glycine Peptides in Aqueous Ethanol and Dioxane Solutions. Establishment of a Hydrophobicity Scale. *J. Biol. Chem.*, 246(7):2211–2217, 1971.
- [91] F. Hofmeister. Von der Lehre der Wirkung der Salze . *Arch. Exp. Pathol. Pharmacol.*, 24:247–260, 1888.
- [92] A. A. Green. Studies in the Physical Chemistry of the Proteins. VIII. The Solubility of Hemoglobin in concentrated Salt Solutions. A Study of The Salting Out of Proteins. *J. Biol. Chem.*, 93(2):495–516, 1931.
- [93] P. L. Whitney and C. Tanford. Solubility of Amino Acids in Aqueous Urea Solutions and Its Implications for the Denaturation of Proteins by Urea. *J. Biol. Chem.*, 237(5):PC1735–1737, 1962.
- [94] J. Huddleston, J. C. Abelaira, W. Rayduen, and A. Lyddiatt. Protein partition between the different phases comprising poly(ethylene glycol)-salt aqueous two-phase systems, hydrophobic interaction chromatography and precipitation: a generic description in terms of salting-out effects. *J. Chromatogr. B*, 680:31–41(11), 1996.
- [95] Y. Zhang and P. S. Cremer. Interactions between macromolecules and ions: The Hofmeister series. *Curr. Opin. Chem. Biol.*, 10(6):658–663, 2006.
- [96] K. Sritharan, C. J. Strobl, M. F. Schneider, A. Wixforth, and Z. Guttenberg. Acoustic mixing at low Reynold’s numbers. *Appl. Phys. Lett.*, 88(5):054102, 2006.

- [97] C. A. Fulcher, Z.M. Ruggeri, and T. S. Zimmerman. Isoelectric focusing of human von Willebrand factor in urea-agarose gels. *Blood*, 61(2):304–310, 1983.
- [98] M. Marumo, A. Suehiro, E. Kakishita, K. Groschner, and I. Wakabayashi. Extracellular pH affects platelet aggregation associated with modulation of store-operated Ca^{2+} entry. *Thromb. Res.*, 104(5):353–360, 2001.
- [99] V. Huck, A. Niemeyer, T. Goerge, E. M. Schnaeker, R. Ossig, P. Rogge, M. F. Schneider, H. Oberleithner, and S. W. Schneider. Delay of acute intracellular pH recovery after acidosis decreases endothelial cell activation. *J. Cell. Physiol.*, 211(2):399–409, 2007.
- [100] W. Z. Martini, M. A. Dubick, C. E. Wade, and J. B. Holcomb. Evaluation of tris-hydroxymethylaminomethane on reversing coagulation abnormalities caused by acidosis in pigs. *Critical care medicine*, 35(6):1568–1574, 2007.
- [101] M. D. Wang, H. Yin, R. Landick, J. Gelles, and S. M. Block. Stretching DNA with optical tweezers. *Biophys. J.*, 72(3):1335–1346, 1997.
- [102] M. Arya, B. Anvari, G. M. Romo, M. A. Cruz, J. F. Dong, L. V. McIntire, J. L. Moake, and J. A. Lopez. Ultralarge multimers of von Willebrand factor form spontaneous high-strength bonds with the platelet glycoprotein Ib-IX complex: studies using optical tweezers. *Blood*, 99(11):3971–3977, 2002.
- [103] W. Nolting. *Grundkurs Theoretische Physik: 4 Spezielle Relativitätstheorie, Thermodynamik*. Vieweg, 1999, ISBN-3-528-26934-0.
- [104] L. D. Landau and E. M. Lifschitz. *Lehrbuch der theoretischen Physik: V Statistische Physik Teil 1*. Akademie Verlag, 1987, ISBN-3-05-500063-3.
- [105] B. H. Zimm and J. K. Bragg. Theory of the One-Dimensional Phase Transition in Polypeptide Chains. *J. Chem. Phys.*, 28:1246–1247, 1958.
- [106] D. Poland and H. A. Scheraga. Phase Transitions in One Dimension and the Helix-Coil Transition in Polyamino Acids. *J. Chem. Phys.*, 45:1456–1463, 1966.
- [107] A. Jenkins. *Compendium of Macromolecular Nomenclature: The Purple Book (IUPAC)*. Blackwell Sci., 1990, ISBN-0632028467.
- [108] W. A. Linke, M. Kulke, H. Li, S. Fujita-Becker, C. Neagoe, D. J. Manstein, M. Gautel, and J. M. Fernandez. Pevk domain of titin: An entropic spring with actin-binding properties. *J. Struct. Biol.*, 137(1-2):7194 – 205, 2002.
- [109] D. M. Steppich, J. Griesbauer, T. Frommelt, A. Wixforth, and M. F. Schneider. The Heat Capacity of Phospholipid Monolayers in the Vicinity of a Critical Point. *in preparation*.

- [110] L. Tskhovrebova, J. Trinick, J. A. Sleep, and R. M. Simmons. Elasticity and unfolding of single molecules of the giant muscle protein titin. *Nature*, 387:308–312, 1997.
- [111] K. Jacobson and D. Papahadjopoulos. Phase transitions and phase separations in phospholipid membranes induced by changes in temperature, pH, and concentration of bivalent cations. *Biochemistry*, 14(1):152–61, 1975.
- [112] B. Griepernau, S. Leis, M. F. Schneider, M. Sikor, D. M. Steppich, and R. A. Böckmann. 1-Alkanols and membranes: A story of attraction. *Biochim. Biophys. Acta*, 1768(11):2899–913, 2007.
- [113] D. Papahadjopoulos, M. Moscarello, E. H. Eylar, and T. Isac. Effects of proteins on thermotropic phase transitions of phospholipid membranes. *Biochim. Biophys. Acta*, 401(3):317–35, 1975.
- [114] T. Heimburg. *Thermal Biophysics of Membranes*. Wiley-VCH, 2007, ISBN-3527404716.
- [115] B. Linder. *Thermodynamics and Introductory Statistical Mechanics*. Wiley and Sons, 2004, ISBN-0471474592.
- [116] L. K. Tamm and H. M. McConnell. Supported phospholipid bilayers. *Biophys. J.*, 47(1):105–113, 1985.
- [117] J. A. Killian and G. von Heijne. How proteins adapt to a membrane-water interface. *Trends Biochem. Sci.*, 25(6):429–434, 2000.
- [118] H. Sandermann. Regulation of membrane enzymes by lipids. *Biochim. Biophys. Acta*, 515(3):209–237, 1978.
- [119] A. A. P. Schmitz, E. Schleiff, C. Röhring, A. Loidl-Stahlhofen, and G. Vergères. Interactions of myristoylated alanine-rich c kinase substrate (marcks)-related protein with a novel solid-supported lipid membrane system (transil). *Anal. Biochem.*, 268(2):343–353, 1999.
- [120] A. Loidl-Stahlhofen, A. S. Ulrich, S. Kaufmann, and T. M. Bayerl. Protein binding to supported lecithin bilayers controlled by the lipid phase state: a new concept for highly selective protein purification. *Eur. Biophys. J.*, 25(2):151–153, 1996.
- [121] T. Heimburg. Mechanical aspects of membrane thermodynamics. estimation of the mechanical properties of lipid membranes close to the chain melting transition from calorimetry. *Biochim. Biophys. Acta*, 1415, 1998.
- [122] M. Uragami, T. Dewa, M. Inagaki, R. A. Hendel, and S. L. Regen. Influence of head group mismatch on the miscibility of phospholipids in the physiologically-relevant fluid-phase - a nearest-neighbor recognition analysis. *J. Am. Chem. Soc.*, 119(16), 1997.

-
- [123] L. A. Bagatolli and E. Gratton. A Correlation between Lipid Domain Shape and Binary Phospholipid Mixture Composition in Free Standing Bilayers: A Two-Photon Fluorescence Microscopy Study. *Biophys. J.*, 79(1):434–447, 2000.
- [124] S. White. How Membranes Shape Protein Structure. *APS Meeting Abstracts*, pages L8001+, March 2004.
- [125] J. A. Killian. Hydrophobic mismatch between proteins and lipids in membranes. *Biochim. Biophys. Acta*, 1376, 1998.
- [126] M. M. Sperotto and O. G. Mouritsen. Dependence of lipid membrane phase transition temperature on the mismatch of protein and lipid hydrophobic thickness. *Eur. Biophys. J.*, 16(1):1–10, 1988.
- [127] A. Wixforth. *personal communication*.
- [128] D. M. Steppich. *Diplomarbeit: Kopplung von mechanischen und thermodynamischen Eigenschaften von Phospholipidmembranen in der Nähe von Phasenumwandlungen - Bedeutung für Anwendungen und Biologie*. Universität Augsburg, 2005.
- [129] P. Martin and Szablewski. *Langmuir-Blodgett Troughs - Operating Manual*. NIMA, 2002.
- [130] W. R. Taylor. The classification of amino acid conservation. *J. Theor. Biol.*, 119:205–218, 1986.
- [131] J. Kyte and R. F. Doolittle. A simple method for displaying the hydrophatic character of a protein. *J. Mol. Biol.*, 157:105–132, 1982.
- [132] G. Adam, P. Läger, and G. Stark. *Physikalische Chemie und Biophysik*. Springer, 2003, ISBN-3-540-00066-6.
- [133] T. Heimburg. A Model for the Lipid Pretransition: Coupling of Ripple Formation with the Chain-Melting Transition. *Biophys. J.*, 78(3):1154–1165, 2000.

Curriculum Vitae

PERSÖNLICHE INFORMATIONEN

Name Daniel Michael Steppich
Geburtsdatum 22.03.1979
Geburtsort Augsburg

SCHULAUSBILDUNG

1999 Abitur am Ringeisen-Gymnasium Ursberg (Abschlussnote: 1.4)

GRUNDWEHRDIENST

1999 - 2000 Luipold-Kaserne Dillingen, Deutschland

HOCHSCHULAUSBILDUNG AN DER UNIVERSITÄT AUGSBURG

2001 - 2005 Diplom in Experimentalphysik (Abschlussnote: 1.5), Diplomarbeitsthema:
Mechanische und thermodynamische Kopplung in künstlichen Zellmembranen
2005 - Doktorarbeit: The Physics of Von Willebrand Factor (VWF)
2005 - Förderung durch das "Elitenetzwerks Bayern" (ENB) im Rahmen des
internationalen Doktorandenkollegs "Material Science of Complex Interfaces"
(CompInt)

FORSCHUNGSaufenthalte

2006 Universität Linz, Österreich (2 Monate)
2007 Yale University, New Haven, USA (3 Monate)

ZUSÄTZLICHE QUALIFIKATIONEN

2004 - Mitglied der "Deutschen Biophysikalischen Gesellschaft"
2007 Soft-Skills Workshop "Rhetorik und Präsentation"
2008 Soft-Skills Workshop "Führungskompetenzen"

Fließend Englisch in Schrift und Wort
Studium der Betriebswirtschaftslehre als Nebenfach
Sehr gute Kenntnisse in Microsoft Office

HOBBYS

Fußball, Ski fahren, Kino